Quantum Phases for rotating bosons

ACADEMISCH PROEFSCHRIFT

ter verkrijging van de graad van doctor
aan de Universiteit van Amsterdam
op gezag van de Rector Magnificus
prof. mr. P.F. van der Heijden
ten overstaan van een door het college voor promoties ingestelde
commissie, in het openbaar te verdedigen in de Aula der Universiteit
op dinsdag 24 mei 2005, te 14.00 uur.

door

Jasper Willem Reijnders

geboren te Zaandam

PROMOTIECOMMISSIE:

PROMOTOR:

Prof. dr. C. J. M. Schoutens

OVERIGE LEDEN:

Prof. dr. ir. H. T. C. Stoof
Prof. dr. E. J. Mueller
dr. J. S. Caux
Prof. dr. B. Nienhuis
Prof. dr. J. Walraven
Prof. dr. A. M. M. Pruisken

FACULTEIT DER NATUURWETENSCHAPPEN, WISKUNDE EN INFORMATICA

THIS THESIS IS BASED ON THE FOLLOWING PAPERS:

- J. W. Reijnders and R. A. Duine,
  Pinning and collective modes of a vortex lattice in a Bose-Einstein condensate,
  `cond-mat/04011307`, (Accepted in Phys. Rev. A).
- N. R. Cooper, F.J.M. van Lankvelt, J.W. Reijnders and K. Schoutens,
  Density profiles for atomic quantum Hall states,
  `cond-mat/0409146`, (Submitted to Phys. Rev. A).
- J. W. Reijnders and R. A. Duine,
  Pinning of vortices in a Bose-Einstein condensate by an optical lattice,
  Phys. Rev. Lett. **93**, 060401 (2004) [`cond-mat/0401583`].
- J. W. Reijnders, F. J. M. van Lankvelt, K. Schoutens and N. Read,
  Rotating spin-1 bosons in the lowest Landau level,
  Phys. Rev. A **69**, 023612 (2004), [`cond-mat/0306402`].
- J. W. Reijnders, F. J. M. van Lankvelt, K. Schoutens and N. Read,
  Quantum Hall states and boson triplet condensate for rotating spin-1 bosons,
  Phys. Rev. Lett. **89**, 120401 (2002), [`cond-mat/0203263`].

PARANIMFEN: *Joris Reijnders*
Anne Koopmanschap

COVER: *Joachim Baan*

Nederlandse Organisatie voor Wetenschappelijk Onderzoek

This work is is financially supported by the "Nederlandse Organisatie voor Wetenschappelijk Onderzoek (NWO)".

Contents

Chapter 1

Introduction

The theoretical concept of Bose-Einstein condensation originated from Einstein in 1924 [1], following the work of the Indian physicist Bose [2]. However, the phase transition associated with the condensation of particles in a single quantum state had already been observed years before, when Kamerlingh-Onnes discovered superconductivity in 1911 [3]. The peculiar statistical properties of particles with integer spin, or bosons, leading to a macroscopic occupation of a single quantum state, play a crucial role in explaining remarkable physics in a wide range of systems. Prominent examples are superfluidity in liquid ^{4}He, where a small but significant fraction of the bosonic helium-4 atoms occupy the ground state, and superconductivity in metals through the condensation of Cooper pairs. A relatively new, but very important class of systems exhibiting Bose-Einstein condensation is that of ultra cold dilute gases. Other examples are superfluidity in ^{3}He where the bosons are formed by pairs of fermionic atoms, and condensation of nucleon pairs in nuclear matter.

The foundation of superconductivity dates back to the beginning of the twentieth century before even the theoretical concept of Bose-Einstein condensation was invented. However, it took till 1995 before researchers managed to realize Bose-Einstein condensation in ultra cold dilute alkali gases. The first experimental efforts to create an atomic condensate date back to the 1970s and were focused on spin-polarized hydrogen. Decades of development in trapping and cooling techniques eventually led to the creation of a Bose-Einstein condensate in rubidium [4], sodium [5] and lithium [6]. Later, condensates were created in other atomic species, including spin-polarized hydrogen, helium and potassium.

Reaching the low temperatures required for condensation in alkali vapors and trapping the atomic clouds had long been a great challenge, but nowadays the experimental realization of Bose-Einstein condensation in such systems is well established. It has opened up the possibility to study quantum physics on a macroscopic scale in very clean systems. Many phenomena exhibited by these quantum gases have been studied extensively and are understood quite well. These include the emergence of quantized vortices, collective excitations, and the dynamics of the condensate. In

particular, many of the predictions of a mean field description of the condensate have been observed. However, a lot of questions remain. For instance, regimes beyond mean field theory characterized by important quantum correlations receive much interest. Important examples are strong correlations induced by a so-called Feshbach resonance leading to the possibility of tuning the strength of interactions, and the (possible) emergence of atomic quantum Hall states at ultra fast rotation. Another major direction of research is focused on the physics of Bose gases in sophisticated confining geometries, such as periodic optical lattices. Apart from the exhaustive interest in the physics of cold Bose gases, the progress in experimental techniques has also led to the study of ultra cold fermionic gases. Today, this has become a field of its own.

Storing angular momentum in a Bose-Einstein condensate by applying a rotational force leads to a whole range of remarkable physical effects. All of these are very special in the sense that they underline the quantum mechanical nature of the ultra cold atomic systems. A fascinating feature of rotating Bose-Einstein condensates is the emergence of quantized vortices in order to accommodate the angular momentum. At the present day, the behavior of (lattices of) these vortices is very well understood, on a experimental and theoretical level. Although vortex lattices alone are interesting enough, yet another realm of spectacular physics opens up by adding 'extras'[1] to the system. This thesis deals with rotating condensates enriched by these additional ingredients. The subject we study can be divided in three separate parts. However, each part is connected to the others by placing it in the context outlined above, see figure 1.1.

First, in chapter 3, we study the influence of a co-rotating periodic potential (one- or two dimensional optical lattice) on the structure of a vortex lattice in a Bose-Einstein condensate. In the phase diagram we find structural transitions as function of the lattice strength and the vortex density. A calculation of the dispersion of the collective modes of the vortex lattice reveals that they acquire a gap in the presence of the periodic potential.

Secondly, in chapter 4 and 5 we consider a rotating condensate in which three spin components (spin-1) are included. 'Spin' has a great impact on the way the system reacts to the rotation. An enormous enhancement of the number of configurations (compared to singly quantized vortices) that can accommodate the angular momentum is one of the consequences. We map out the phase diagram of a rotating spin-1 condensate by identifying the structure of the spin-textures as a function of the interaction strengths and angular momentum.

Third, in chapter 6, we focus on the implications of ultra fast rotation in a (single component) condensate. On theoretical grounds, it is expected that forcing very large amounts of angular momentum in the system will drive the vortex lattice through a quantum melting transition. Beyond this transition the ground state is described very well by strongly correlated quantum Hall vortex liquids. The properties of these liquids are very remarkable, for instance, the behavior of (some of) the excitations is

[1] such as periodic potentials, very large amounts of angular momentum or a spin degree of freedom

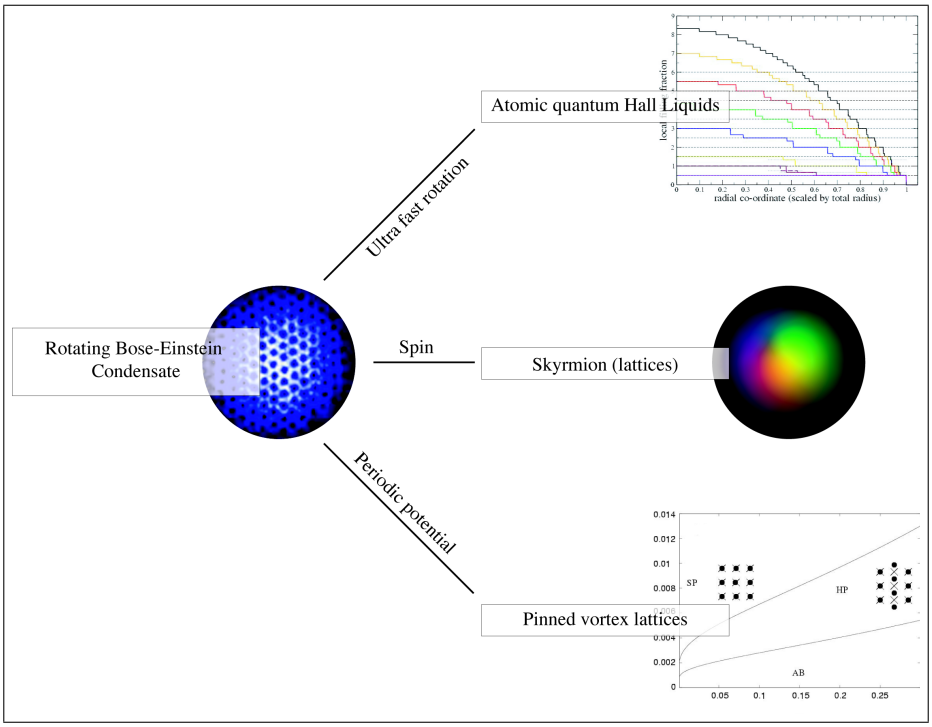

Figure 1.1: Fascinating physics emerges when rotating Bose-Einstein condensates are provided with additional “ingredients”.

described by fractional (non-Abelian) statistics. Experimentally it is very challenging to create such ultra fast rotating systems. We discuss density features of atomic quantum Hall states in a multi-layer geometry, which are relevant for a specific experimental set-up.

A fourth subject, which we also studied, is the characterization of the quantum liquids for rotating spin-1 condensates. However, this study is not included in this thesis. Interested readers should consult [7, 8] or [9].

Before we start with the main part of this thesis we introduce in chapter 2 some of the physics needed to proceed. We discuss various properties of atomic condensates and their response to rotation. Furthermore the concept of atomic quantum Hall states is introduced and the difference between spin-less and spin-full Bose-Einstein condensates is highlighted. Chapter 2 therefore serves as a general introduction to this thesis.

Chapter 2

Bose-Einstein condensation, rotation and spin

2.1 Bose-Einstein condensation in atomic gases

Among all quantum condensates, the atomic vapors are very special candidates to investigate quantum phenomena on a macroscopic scale. The advantages of using ultra cold gases are numerous. We mention the major ones. First of all, the fraction of atoms that occupy the lowest energy quantum state (the so-called condensate fraction) is very large below the critical temperature T_c, compared to, for instance, superfluid liquid helium. Therefore the condensate may be described by mean field theory accurately. Secondly, the low densities in dilute gaseous Bose-Einstein condensates lead to large coherence (healing) lengths. Gradients in the condensate wave function thus occur on a relatively large scale which can be as large as the system size. Therefore it is relatively easy to study density features by the use of optical methods after expansion of the cloud. Third, the low [1] temperatures in a alkali vapor enable the observation of a variety of collective phenomena, without being obscured by thermal fluctuations. These phenomena range from various types of surface waves to soliton solutions of the equations of motion [10].

Atomic interactions strongly influence the properties of the Bose-Einstein condensate. At low temperatures, these properties can be calculated reliably by only taking into account the two-body interactions which are characterized by the s-wave scattering length a_s. This is a direct consequence of the fact that ultra cold alkali vapors are dilute ($na_s^3 << 1$) in the sense that the mean particle separation $n^{-1/3}$ is large compared to the scattering length a. Therefore, the interactions are dominated by two-body processes. The effective inter-atomic short range interactions can

[1] Since the density in the cloud is very small, typically of the order $10^{13} - 10^{15}$ cm^{-3}, the temperatures below which quantum phenomena become important are incredibly low, $T_c \sim 10^{-5}$ K. By contrast, temperatures required for liquid ^{4}He are $T_c \sim 1$ K.

be attractive or repulsive, corresponding to a negative or positive scattering length, respectively. This leads to completely different physics in both cases. For instance, a gas with attractive interactions remains a compact droplet when it is subject to a rotational force, whereas quantized vortices will develop in the repulsive case.

The physics of a condensed atomic vapor is strongly dependent on the nature of the trap. In generic experiments one uses a *magnetic trap* to spatially confine the gas. The working principle of this type of trap is that the energy of an atomic state with certain hyperfine level m_F depends on external magnetic fields (the Zeeman effect). A magnetic field engineered such that it creates a spatial minimum in this energy will trap (slow moving) atoms with hyperfine label m_F. Another class of traps which is often used is based on the dipole force which the atoms experience in an off-resonant light field. A trap of this type is known as an *optical trap*. The energy shift of an atomic state confined by an optical trap depends very weakly on the internal hyperfine level m_F of the atoms. As a consequence, atoms in optical traps are characterized by the spin degree of freedom of the lowest energy hyperfine multiplet F of their electronic ground state. In turn, the overall hyperfine spin of a condensed atomic vapor with $F > 0$ confined in an optical trap becomes a free parameter. A Bose-gas with 'liberated' hyperfine spin is often referred to as a *multi-component condensate*.

An interesting development in the field of atomic gases is the possibility to trap atoms in a periodic potential using a so-called *optical lattice*. These confining geometries are created by using standing light fields in one-, two- or three directions. A condensate which is loaded in such a trap is divided into an array of condensates containing just a small number of atoms per system. Besides being an important tool to create a large number of small atomic systems, an optical lattice provides a easy way to mimic solid-state physics. For instance, by using an three-dimensional optical lattice Greiner *et al.* [11] were able to experimentally observe the transition from a superfluid, where the atoms are delocalized across the lattice, to a Mott-insulating state where the atoms are localized onsite [12, 13].

2.1.1 Some technical details

In the fully condensed state the single particle wave function $\Psi(\mathbf{r})$ corresponding to the lowest energy is macroscopically occupied. Using effective two-body interactions and neglecting correlations produced by interactions at length scales less then $n^{-1/3}$, the mean field energy of a cloud of condensed atoms held at chemical potential μ is

$$E[\Psi, \Psi^*] = \int \mathrm{d}\mathbf{r}\Psi^*(\mathbf{r}) \left[-\frac{\hbar^2\nabla^2}{2m_b} + \frac{g}{2}|\Psi(\mathbf{r})|^2 + V(\mathbf{r}) - \mu \right] \Psi(\mathbf{r}). \tag{2.1}$$

The mass of the atoms is given by m_b, the effective two-body interaction strength $g = 4\pi\hbar^2 a_s/m_b$ and $V(\mathbf{r})$ is an external (confining) potential. Variation of this energy with respect to $\Psi^*(\mathbf{r})$ leads to the equation of motion for $\Psi(\mathbf{r})$ which is known as the *Gross-Pitaevskii equation* [14, 15]. The solution to the Gross-Pitaevskii equation describes the ground state wave function of the condensate. In general this can be

found directly by numerical integration. However, if the kinetic energy is negligible with respect to the potential and interaction energy scales, and the interaction is repulsive $g > 0$, the density profile of the condensate may be obtained analytically, $|\Psi(\mathbf{r})|^2 = g^{-1}[\mu - V(\mathbf{r})]$. This is referred to as the *Thomas-Fermi approximation*. Quantitatively, this approximation is valid when $Na_s/d_{tr} >> 1$, with d_{tr} the typical length scale associated with the trap.

In a harmonic trap, the Thomas-Fermi density profile takes the form of an inverted parabola. However, near the edge of the atomic cloud, the Thomas-Fermi approximation fails. This is because the length scale over which the wave function rises from zero (at the edge) to its bulk value is fixed by the balance of the kinetic energy and the interaction energy. This length scale is known as the *healing length* $\xi = (8\pi n a_s)^{-1/2}$ and is relevant for superfluidity effects. For instance, it sets the typical size of the core of a quantized vortex. In experimental systems of condensed dilute gases, the healing length is larger then the mean atomic separation.

2.1.2 Multi-component condensates

Optical traps liberate the (hyperfine) spin degree of freedom of spin-full atoms, as there is no polarizing magnetic field. Ultra cold, optically trapped dilute vapors of atoms with a low lying spin-**F** multiplet can be understood as mixtures of $2F + 1$ equivalent, interacting Bose-Einstein condensates. The particle number in each of those condensates is not conserved, since scattering between an initial and final atomic state with a different hyperfine level does not lead to condensed atom loss from the trap. Experimentally, the first multi-component condensates were created in ^{87}Rb [16, 17] and ^{23}Na [18, 19, 20].

The realization of multi component condensates has opened up the possibility to study the combined effect of spin correlations and coherence phenomena. A wide range of quantum phenomena, not present in magnetically trapped (scalar) condensates has attracted a lot of experimental and theoretical interest. These phenomena include changes in the ground state structure with the spin-dependent interaction parameters, spin dynamics [21, 22] and topological defects such as *skyrmions* [23], *monopoles* [24] and π*-disclinations* [25].

Most studies are concerned with spin-1 condensates, as it is the simplest example of a multi-component condensate. The strength of the effective two-body interaction in vapors of condensed spin-1 atoms, is described by two[2] coupling parameters, c_0 and c_2. The first represents the interaction strength in the spin-0 channel, the second one describes the strength in the spin-2 channel.

The nature of the spin correlations divides the phase diagram in two distinct regimes [23], depending on the sign of the spin-dependent interaction c_2. In the *ferromagnetic regime* ($c_2 < 0$), the ground state has maximum possible spin, $F = N$. Such a spin state can be constructed by condensing all the bosons into a single-particle state with $F_z = +1$, or as a spin-rotation of this. In the opposite *anti-ferromagnetic regime*

[2]The spin-1 channel is ruled out since that would require an anti-symmetric two-atom wave function.

($c_2 > 0$), the ground state has minimal spin. Such a spin state can be constructed by condensing all the bosons in the same $F_z = 0$ single-particle spin state, or by taking a spin-rotation of this. Examples of such systems can be realized by optically trapping atoms such as ^{87}Rb ($c_2 < 0$) and ^{23}Na ($c_2 > 0$). In both cases, the ratio $\gamma = c_2/c_0$ of the spin-dependent and the spin-independent parts of the (contact) interaction is small, typically a few percent, $|\gamma| \approx 0.01 - 0.05$.

2.2 Response of a condensate to rotation

The quantum mechanical nature of a Bose-Einstein condensate becomes even more pronounced when an external torque is applied. Storing angular momentum in a condensate leads to very interesting states formed by quantized vortices. The topology of these vortices is dependent on the details of the interactions and the number of components in the condensate. Rotation of a Bose-Einstein condensate enables the study of various types of vortices, which forms a whole research area on its own. Besides this, storing angular momentum in these systems opens the route to the formation of atomic quantum Hall states at ultra high rotation.

At the present day, the physics of vortices in atomic Bose-Einstein condensates and arrays thereof is understood very well, both theoretically and experimentally. The generic behavior as a function of the angular velocity is such that at certain critical rotation frequency ω_c a single vortex line first appears, followed by additional vortices at still higher rotation. The vortices arrange themselves on a hexagonal lattice, in order to minimize their total energy. This vortex lattice supports elliptically polarized phonon excitations, the so-called *Tkachenko modes* [26, 27].

The appearance of quantized vortices in rotating ultra cold dilute gases has first been observed by Matthews *et al.* [28]. Although there has been some experimental interest in the equilibrium and non-equilibrium behavior of a single vortex line [29, 30], since the observation of multiple vortices [31], however, most of the experimental studies are focused on vortex lattices [32, 33, 34, 35]. Usually, vortices in a Bose-Einstein condensate are created by applying a laser beam with a fixed direction, and a center which is rotating in space. This "stirring" rotation field interacts with the atoms and induces a torque on the trapped cloud. The size of the vortex core is set by the healing length ξ over which the condensate density heals back from zero (at the center of the vortex) to the bulk value of the condensate. In atomic condensates, this spatial scale is too small to directly resolve it optically. In an experimental system, to perform a measurement on a vortex state, one first turns off the trap such that the cloud undergoes ballistic expansion before the spatial scale of the vortices can be studied by optical means, see figure 2.1.

The stabilization of (a lattice of) singly quantized vortices in a rotating harmonically trapped ultra cold gas with repulsive atom-atom interactions over the uniform irrotational ground state can best be understood by comparing the energy of a single vortex state E_{vortex} with that of the uniform condensate $E_{uniform}$ in the rotating frame where $E' = E - \mathbf{L} \cdot \omega$. The energy E is given by equation (2.1) and ω is the

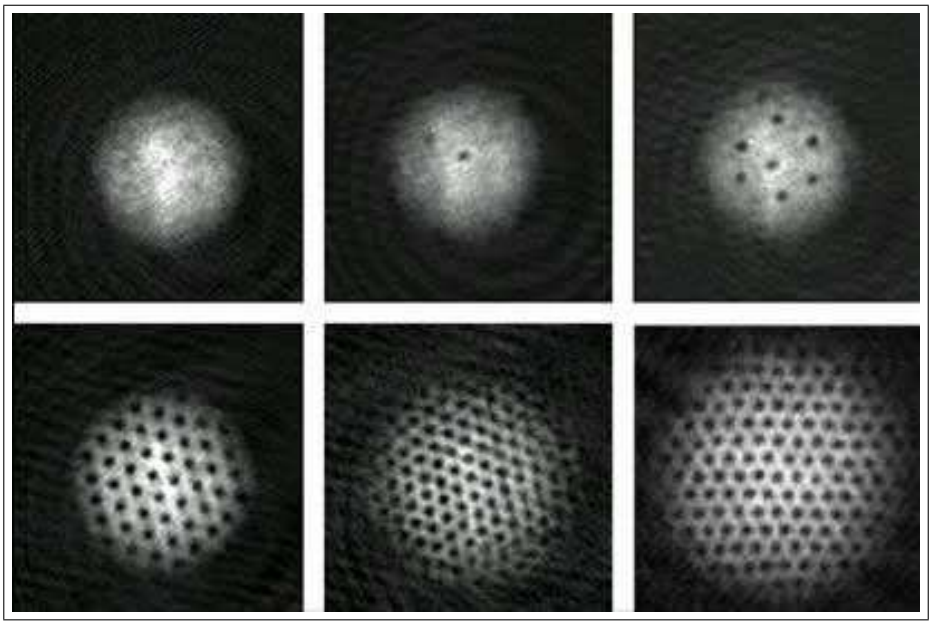

Figure 2.1: Expansion images of a rotating Bose-Einstein condensate of ^{87}Rb atoms containing vortices at different angular velocities. Picture taken from [36].

external rotation frequency or angular velocity. In the rotating frame, E'_{vortex} can be smaller than $E'_{uniform}$ for a rotation exceeding ω_c. This is in marked contrast with vapors of atoms with attractive interactions, where the angular momentum is carried by center-of-mass motion of the cloud, and the system remains a compact blob, without any vortices, all the way up to the maximum rotation frequency (the eigen frequency of the trap ω_0).

A system containing many vortex lines rotates uniformly with average angular velocity ω which is related to the two-dimensional vortex density by $n_v = m_b\omega/(\pi\hbar)$ [37]. From this relation it can be seen that as the system rotates more rapidly, the vortex density increases *i.e.* the vortices come closer to each other. At the same time, as the healing length becomes comparable with the mean distance between the vortices, the vortex cores start to shrink with increasing ω [38, 39]. This is a direct consequence of the fact that the vortices repel each other and do not want to overlap (at least in the mean field regime). Eventually, the radius of the vortex core scales with the inter-vortex separation and in the limit where ω approaches the eigen frequency ω_0 of the trap, the ratio of the area per vortex and the core area becomes a constant [38, 39, 40, 35]. At this point, the rotating atomic cloud enters the so-called *mean field quantum Hall limit*. In this limit, the transverse trapping potential $V(\mathbf{r}) = \frac{1}{2}m_b\omega_0^2 r_\perp^2$ is canceled by the centrifugal potential, and the condensate expands dramatically in the plane perpendicular to the axis of rotation, effectively

becoming a two-dimensional system. Subsequently the density drops and the energy scale of the interaction becomes small compared to the energy scale associated with the angular velocity, $gn << \hbar\omega$. The dominant energy of the cloud in the rotating frame then becomes equivalent to the energy of an electron in a effective magnetic field $\mathbf{B} = -2m_b\omega/|e|$ in the symmetric gauge. The spectrum of the latter is organized in terms of degenerate harmonic oscillator states or Landau levels. Ho [41] predicted that atoms in a rapidly rotating Bose gas should condense in the *lowest Landau level* (LLL). Experimentally, the mean field quantum Hall limit has been reached convincingly [40]. Rotation rates of $.99\ \omega_0$ and filling fractions (ratio of the particle number N to the number of vortices N_v) of $\nu \sim 500$ have been reached.

The approximate many-body ground state solution of the Gross-Pitaevskii equation in the LLL regime describing a vortex lattice, is a coherent (superfluid) state given by

$$\Psi(z_1, ..., z_N) \propto \prod_{i=1}^{N} \prod_{j} (z_i - \zeta_j) e^{-\frac{|z_i|^2}{2d_\perp^2}}. \tag{2.2}$$

In this wave function, $z = x + iy$, $d_\perp = \sqrt{\hbar/m_b\omega_0}$ is the characteristic length of the trap and $\{\zeta_j\}$ are the positions of the vortices. The state in equation (2.2) may still be interpreted as a Bose-Einstein condensate, since each term in the product (labeled by i) describes a single vortex state which is macroscopically occupied.

2.2.1 Atomic quantum Hall states

Looking at figure 2.1, it is natural to ask what the next picture would look like if one would be able to speed up the angular velocity close to the trap frequency. In this regime of ultra fast rotation, quantum fluctuations of the vortex coordinates become important and mean field theory breaks down. On theoretical grounds the question regarding the nature of the ground state at ultra fast rotation is therefore justified. A number of theoretical studies have been carried out in order to address this question. Throughout the years a scenario has been established in which the quantum fluctuations of the individual vortex cores are expected to cause a *quantum melting* transition [42] of the vortex lattice after which the angular momentum is carried uniformly by a *vortex liquid*. Beyond this transition, the condensate is destroyed and the resulting state of matter is disordered, with a large amount of vorticity stored in it.

In the regime of ultra fast rotation, a number of quantum liquid states have been proposed [43, 44, 45, 46, 47, 48, 49, 50, 7, 8]. Based on the analogy with the physics of electrons in a strong perpendicular magnetic field in two dimensions, the boson quantum liquid states can be characterized as *fractional quantum Hall liquids*, see figure 2.3 for an overview. The critical filling fraction at which the melting transition should occur, was estimated to be $\nu_c \approx 10$ by the Lindemann criterion [46] (that is, the average fluctuation in the position of the vortices equals the separation between them). An exact diagonalization study using periodic boundary conditions found that the vortex lattice of equation (2.2) melts at a critical $\nu = \nu_c \approx 6 - 10$, and that incompressible fluid states occur at $\nu = \frac{k}{2} < \nu_c$, with $k = 1, 2, 3, ..$, see figure 2.2. The

corresponding ground state wavefunctions have large overlaps with the Read-Rezayi series [46, 51] of fractional quantum Hall states.

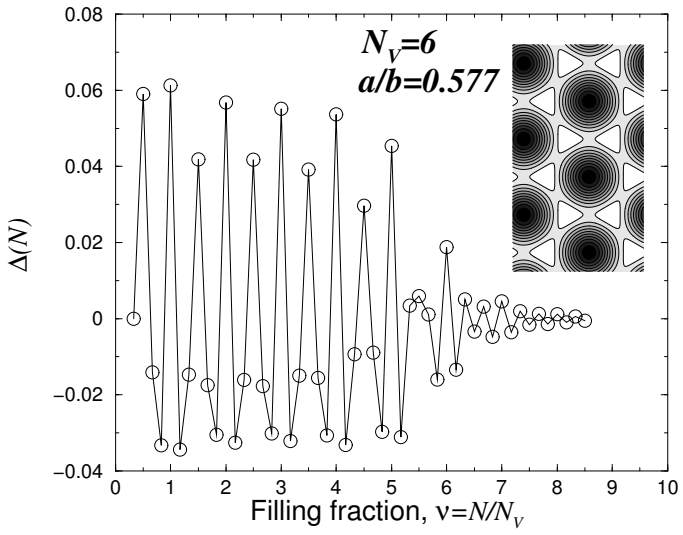

Figure 2.2: The energy gap as function of the filling fraction over the ground state of a bosonic system subject to large amounts of vorticity. Upward spikes signal values of ν for which the ground state is incompressible. The collapse of the gaps at $\nu \sim 6$ indicates the transition to the vortex lattice phase. Inset shows the density of the mean field ground state. This results from exact diagonalization studies in an toroidal geometry with aspect ratio $a/b = 1/\sqrt{3}$. Figure taken from [46].

The Read-Rezayi quantum Hall states possess a specific "order-k" clustering property: whenever $k+1$ bosons are brought together on the same position, the wave function vanishes. This implies that the Read-Rezayi states are zero energy ground states of a $k+1$ body contact interaction. Another special feature of the Read-Rezayi states (with $k > 1$) is that the properties of their quasi-particle excitations are described by non-Abelian statistics. This means that adiabatic transport of quasi-particles leads to a matrix operation on the space of degenerate quasi-particle states. This latter exotic property makes the study of rapidly rotating ultra cold Bose gases even more interesting and is a major justification of experimental efforts to create systems with small filling factors.

A special member of the Read-Rezayi series is the bosonic *Laughlin liquid* at $k = 1$ and $\nu = \frac{1}{2}$

$$\Psi(z_1, ..., z_N) \propto \prod_{i<j}^{N} (z_i - z_j)^M e^{-\sum_j^N \frac{|z_i|^2}{2d_\perp^2}}, \qquad \text{with } M = 2. \tag{2.3}$$

This state, with $M = 3$, was first proposed by Laughlin in 1983 in the context of electronic systems that exhibit the $\nu = \frac{1}{3}$ fractional quantum Hall effect [52]. The strongly correlated nature of the Laughlin liquid reflects itself in the fact that whenever two particles approach each other, the wavefunction vanishes. Furthermore it is an exact, zero energy eigenstate of the two-body contact interaction. The Laughlin wavefunction of equation (2.3) describes the many-body ground state of a system of harmonically trapped, neutral bosons at and slightly below $\omega = \omega_0$. Unfortunately, this is right at the point at which the system becomes unstable.

A second special member of the Read-Rezayi series is the bosonic *Moore-Read state* [53] at $k = 2$. It is the simplest quantum Hall state with the above mentioned clustering property and may be represented as the symmetrized product of two Laughlin liquids. Suppressing the exponential factor it reads

$$\Psi(z_1, ..., z_N) \propto \mathcal{S} \prod_{i<j\in A}^{N/2} (z_i - z_j)^2 \prod_{k<l\in B}^{N/2} (z_k - z_l)^2, \tag{2.4}$$

where $\mathcal{S}$ means total symmetrization with respect to the coordinates $\{z_j\}$. A and B label groups that each contain $\frac{N}{2}$ particles. This wave function has a paired structure in the sense that it vanishes whenever 3 bosons (or more) come together on the same position. It has a large overlap with the exact ground state of a harmonically trapped system of rotating bosons at $\nu = 1$ [46, 47, 48, 49].

Yet another type of fractional quantum Hall state important for the description of rapidly rotating bosons are the *composite fermion* states [44]. These fit in a hierarchy scheme, analogous to the Jain principal sequence for [54] fermions. Composite fermion states can be 'understood' as follows. In the original system, each boson binds to a vortex which carries a unit of statistical flux. The composite entities obey fermionic statistics and feel a reduced vorticity field as compared to the original system. When the composite fermions occupy exactly an integer number p of Landau levels, the resulting state is incompressible, with a filling fraction of $\nu = \frac{p}{p+1}$ in the original sytem. Numerical evidence for the existence of composite fermion states in the spectrum of a rapidly rotating dilute Bose gas at $\nu = \frac{2}{3}, \frac{3}{4}, \frac{4}{5}$ has been found [47, 48, 49].

In two different groups, experimental researchers tried to approach the vortex liquid regime as close as possible. Schweikhard *et al.* [40] reached filling fractions of $\nu \sim 500$ at $\omega = .99\omega_0$, as said before. However, this is still far away from the (expected) melting transition. Because of the instabillity at $\omega = \omega_0$, experimental detection of a vortex liquid in atomic systems typically will involve a superpotential steeper than the harmonic trap to avoid the system flying apart. Bretin *et al.* [55] performed an experiment on a rapidly rotating condensate in a confining potential of the form $\tilde{V}(\mathbf{r}) = \frac{1}{2} m_b \omega_0^2 r_\perp^2 + \frac{1}{4} k_4 r_\perp^4$, in which they pushed the angular velocity beyond ω_0. Despite the fact that dramatic changes where observed in the appearence of the quantum gas, the nature of the observed state remains unclear at the present day. In any case, it seems very unlikely that it has anything to do with a fractional quantum Hall liquid, because of the high filling fractions in this experiment.

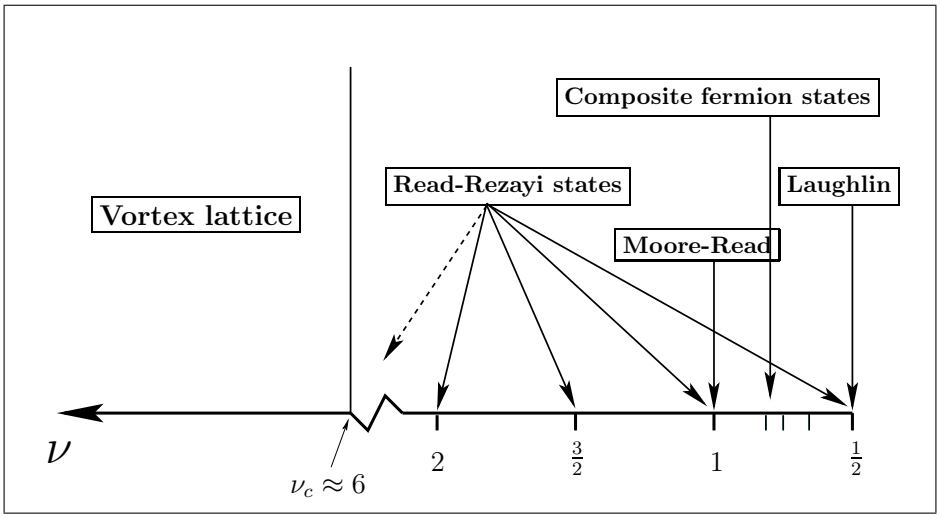

Figure 2.3: Theoretical survey of the atomic quantum Hall states in a rapidly rotating, harmonically trapped dilute Bose gas.

2.2.2 Multi-component condensates and rotation

Storing angular momentum in multi-component Bose-Einstein condensate may lead to the stabilization of topological defects, analogous to the appearence of vortex states in a rotating one-component (scalar) condensate. However, in the multi-component case the structure of these objects is much more complicated.

In section 2.1.2 we explained the appearance of two types of ordered Bose-Einstein condensates for spin-1 bosons. In these the order is constant in space. More generally, a condensate will prefer to have the same type of order locally at almost all points in order to lower the energy, but there are types of excitations in which the order as described by a point in the order parameter manifold can vary in space. Some excitations of this type are stable under continuous deformations of the order.

In the spin-1 case, the main important types of topological defects are the π-disclination and the coreless vortex. One can think of a π-disclination as (spin rotations of) a configuration in which half of the bosons form a vortex in the $F_z = \uparrow$ state with a core filled by the other half of the bosons occupying the $F_z = \downarrow$ state. A coreless vortex, or skyrmion, is a topologically-nontrivial texture in the order that carries nonzero vorticity quantized in integers. Mean field states of coreless vortices for rotating spin-1 bosons have been investigated theoretically by solving the spin-full Gross-Pitaevskii equations [56, 57, 58, 59].

At higher rotation rates one expects to find[3] lattices, built from the coreless vortices, similar to the Abrikosov lattice of singly quantized vortices in a rotating scalar

[3]Experimentally, spin textures and lattices thereof may be imaged by using polarized light [60].

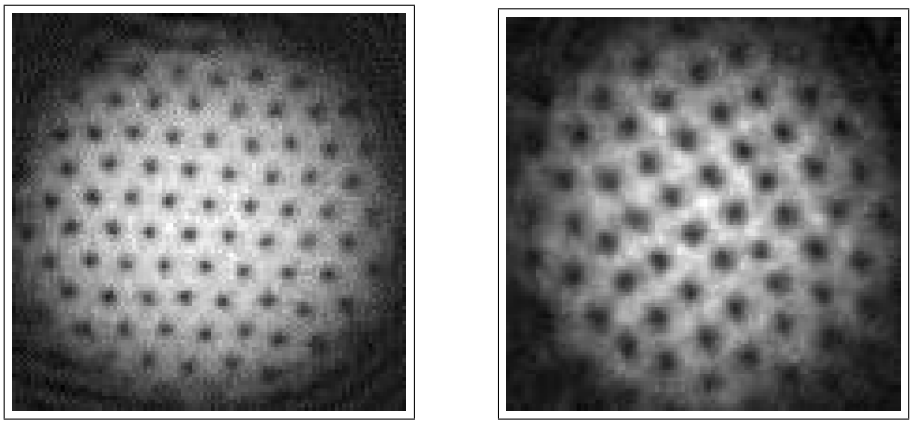

Figure 2.4: A square vortex lattice (right panel) in a two-component condensate of ^{87}Rb atoms. The picture displays the imaging of one of the two components. To emphasize the structural difference we displayed also a hexagonal vortex lattice (left panel). Pictures by courtesy of V. Schweikhard.

condensate. For a spin-1 condensate, the lattice geometry depends crucially on the relative strength $\gamma = c_2/c_0$ of the spin-dependent interaction. For $\gamma = 0$, where the $SU(3)$ symmetry between the different spin components is not broken, the lattice that is expected upon rotation is composed of three intertwined triangular lattices. The vortex cores do not overlap, so that the density is (almost) uniform. This lattice has been shown to be independent of the absolute strength of the interaction by Kita *et al.* [61]. The vortex lattice shows a rich phase diagram, however, when the interaction is spin-dependent ($\gamma \neq 0$). For a range of positive values of γ, a rectangular lattice composed of π-disclinations has been predicted [61].

In a recent experiment [62] on rotating *two-component* condensates, square vortex lattices in both components [63, 64] were observed (see figure 2.4). In these systems, the vortex cores in either component are filled by the fluid of the other component. This interlocked vortex configuration can be interpreted as a lattice composed of coreless vortices and indicates that these topological excitations indeed play an important role in the physics of rotating multi-component condensates.

In the limit of extremely fast rotation, the above mentioned lattices are expected to melt, by analogy with the quantum melting of the Abrikosov vortex lattice in scalar Bose-Einstein condensates. The resulting states are translationally invariant quantum fluids. The nature of these fluids is highly dependent on the ratio of the interaction strengths γ. In reference [7, 8] three series of fractional quantum Hall states for rotating spin-1 bosons where proposed and analyzed.

Chapter 3

Pinning of vortices

We[1] *consider the ground state of vortices in a rotating Bose-Einstein condensate that is loaded in a co-rotating two-dimensional optical lattice. Due to the competition between vortex interactions and their potential energy, the vortices arrange themselves in various patterns, depending on the strength of the optical potential and the vortex density. We outline a method to determine the phase diagram for arbitrary vortex filling factor. Using this method, we discuss several filling factors explicitly. For increasing strength of the optical lattice, the system exhibits a transition from the unpinned hexagonal lattice to a lattice structure where all the vortices are pinned by the optical lattice. The geometry of this fully-pinned vortex lattice depends on the filling factor and is either square or triangular. For some filling factors there is an intermediate half-pinned phase where only half of the vortices is pinned. We also consider the case of a two-component Bose-Einstein condensate, where the possible coexistence of the above-mentioned phases further enriches the phase diagram. In addition, we calculate the dispersion of the low-lying collective modes of the vortex lattice and find that, depending on the structure of the ground state, they can be gapped or gapless. Moreover, in the half-pinned and fully-pinned phase, the collective mode dispersion is anisotropic. Possible experiments to probe the collective mode spectrum, and in particular the gap, are suggested.*

A common feature of the experiments with ultra cold atomic gases is that these systems are very clean. What distinguishes the physics of vortices in atomic Bose-Einstein condensates from superfluid Helium and superconductors, is that in the latter systems the pinning of vortices due to intrinsic disorder in the system plays an important role [65, 66, 67, 68, 69, 70, 71]. This, together with the discovery of high-temperature superconductors, has led to many theoretical studies of the effects of pinning on the melting of the vortex lattice [72, 73, 74, 75]. Furthermore, in the context of type-II superconductivity, there has been a lot of interest in the effects of a periodic array of

[1] This chapter is based on a collaboration with R. A. Duine, see [81, 82].

pinning centers on the groundstate of the vortices [76, 77, 78, 79, 80]. In particular, it turns out that, due to the competition between vortex interactions and pinning, the system exhibits a rich ground state phase diagram, as a function of the vortex density and the strength of the pinning potential [80]. However, since the pinning potential in the case of vortices in type-II superconductors is known only phenomenologically, a detailed comparison between theory and experiment seems unfeasible.

Very recently, we have shown that a rotating Bose-Einstein condensate in a so-called optical lattice is a very attractive system to study the pinning of vortex lattices in a superfluid [81]. Such an optical lattice is formed by laser fields that trap the atoms using the dipole force. Recently, the experimental control over the strength of the optical lattice enabled Greiner *et al.* [11] to experimentally explore the Mott-Insulator to superfluid quantum phase transition [12, 13]. By rotating the optical lattice at the same frequency of rotation as the Bose-Einstein condensate, the vortices experience a static pinning potential that is determined by the optical lattice [81, 83, 84]. Such a co-rotating optical lattice can be made by rotating holographic phase plates or amplitude masks [85, 86, 87, 88]. Since the strength of the optical lattice determines the strength of the pinning potential, and the rotation frequency controls the density of vortices, the phase diagram can be studied in detail experimentally.

Complementary to our work, Pu *et al.* [89] studied a Bose-Einstein condensate in a co-rotating optical lattice with an additional harmonic confining potential numerically. The harmonic trapping potential leads to finite-size effects which further enrich the phase diagram of the system. Unfortunately, including an additional harmonic potential in our variational calculations makes analytical results unfeasible. Therefore, we consider the homogeneous case, which brings out the physics of the competition between vortex interactions and pinning potential most clearly.

This chapter is organized as follows. In section 3.1 we derive the pinning potential and vortex interaction energy. Using these results, we calculate in section 3.2 the energy of an arbitrary vortex lattice in a periodic potential. This result is used to determine the ground state phase diagram in section 3.3. In section 3.3.1 we discuss the inluence of a one-dimensional optical potential on the vortex lattice and in section 3.4 we calculate the vortex phase diagram of a two-component condensate in a two-dimensional periodic potential.

3.1 Vortex interactions and potential energy

In this section we calculate the interaction energy of two vortices, as well as the potential energy of a vortex in the optical lattice, i.e., the pinning potential, by means of a variational *ansatz*. These results are needed later on to determine the phase diagram.

3.1.1 Pinning potential

Since we assume the system to be at zero temperature, the most convenient starting point is the hamiltonian functional which gives the total energy of the system in terms of the macroscopic condensate wave function $\Psi(\mathbf{x})$, and reads

$$H[\Psi^*,\Psi] = \int d\mathbf{x}\Psi^*(\mathbf{x})\Big[-\frac{\hbar^2\nabla^2}{2M} + \frac{1}{2}g|\Psi(\mathbf{x})|^2 + V_{\rm OL}(\mathbf{x}) - \mu\Big]\Psi(\mathbf{x}) \ . \tag{3.1}$$

Here, M denotes the mass of one atom which interacts with the other atoms via a two-body contact interaction of strength $g = 4\pi a_s\hbar^2/M$, with $a_s > 0$ the s-wave scattering length. The two-dimensional optical lattice potential is given by

$$V_{\rm OL}(\mathbf{x}) = sE_{\rm R}\left[\sin^2(qx) + \sin^2(qy)\right] \ , \tag{3.2}$$

with $E_{\rm R}$ the recoil energy, q the wavenumber of the optical lattice, and $s \geq 0$ a dimensionless number indicating the strength of the optical lattice. The chemical potential that fixes the number of atoms in the condensate is given by μ.

Throughout this chapter we consider for simplicity a condensate with infinite extent in the x-y-plane which is tightly confined in the z-direction by an harmonic trap with frequency ω_z. This approach is motivated by the fact that a Bose-Einstein condensate that is rotated around the z-axis will extend in the x-y-plane due to the centrifugal force. Assuming that modes in the z-direction are frozen out, such that the wave function is gaussian in this direction, effectively leads to a condensate thickness $d_z \equiv \sqrt{\pi\hbar/(M\omega_z)}$. These assumptions allow us to neglect the curvature of the vortex lines along the z-direction. Note also that we can safely omit the term proportional to the external rotation frequency in equation (3.1), since we intend to work with a variational ansatz which has a fixed vortex density, and, moreover, we assume that the harmonic magnetic trapping potential approximately cancels the centrifugal force.

We consider the system in the Thomas-Fermi limit where the kinetic energy of the condensate atoms is neglected with respect to their potential energy and mean-field interaction energy. Minimizing the hamiltonian of equation (3.1) in this limit, the global density profile of the condensate without vortices is given by

$$n_{\rm TF}(\mathbf{x}) = |\Psi(\mathbf{x})|^2 = n - [V_{\rm OL}(\mathbf{x}) - sE_{\rm R}]/g \ , \tag{3.3}$$

with $n = [\mu - sE_{\rm R}]/g$ the average density of the condensate.

As already mentioned, to find the potential energy of a vortex in a Bose-Einstein condensate in an optical lattice, as a function of its coordinates (u_x, u_y), we use a variational *ansatz* for the condensate wave function. It is given by

$$\Psi(\mathbf{x}) = \sqrt{n_{\rm TF}(\mathbf{x})}\ \Theta\big[|\mathbf{x}-\mathbf{u}|/\xi - 1\big]\exp[i\phi(\mathbf{x},\mathbf{u})] \ , \tag{3.4}$$

with $\xi = 1/\sqrt{8\pi a_s n}$ the healing length that sets the size of the vortex core, $\phi(\mathbf{x},\mathbf{u}) = \arctan[(y-u_y)/(x-u_x)]$ the phase configuration corresponding to one vortex, and $\Theta(z)$ the unit step function. For the above *ansatz* to be a good approximation, we have

assumed that the vortex core is much smaller then an optical lattice period, $q\xi \ll 1$, and that the strength of the potential is sufficiently weak, $sE_{\rm R} < \mu$. The use of a unit step function for the density profile of the vortices is justified because the main contribution to the energy of the vortices is due to the superfluid velocity pattern and not due to the inhomogeneity of the condensate density [37].

Substituting the *ansatz* in equation (3.4) in the hamiltonian in equation (3.1) and integrating over the entire x-y-plane gives the total energy of the vortex in the optical lattice. This energy diverges with the system size. However, we need to isolate the finite, position dependent contribution to the energy due to the presence of the vortex, which is the only relevant contribution for our purposes.

There are two position dependent terms which contribute significantly to the energy. The first one is largest and is entirely due to the kinetic energy of the condensate. Neglecting the effect of the laplacian on the global density profile, which is consistent with the Thomas-Fermi limit, we have

$$U_{\rm kin}(u_x,u_y) = -\frac{d_z s E_{\rm R}}{8a_s}\int dxdy\left[\frac{\sin^2(qx)+\sin^2(qy)}{(x-u_x)^2+(y-u_y)^2}\right] . \tag{3.5}$$

The integral can be done by shifting the integration variables to $x = \rho\cos\theta + u_x$ and $y = \rho\sin\theta + u_y$. A little algebra yields

$$\begin{aligned} U_{\rm kin}(u_x,u_y) &= \frac{d_z s E_{\rm R}}{8a_s}\left[\cos(2qu_x)+\cos(2qu_y)\right]\int_0^{2\pi} d\theta\int_\xi^\infty \frac{d\rho}{2\rho}\cos(2q\rho\cos\theta) \\ &\quad -\frac{d_z s E_{\rm R}}{8a_s}\left[\sin(2qu_x)+\sin(2qu_y)\right]\int_0^{2\pi} d\theta\int_\xi^\infty \frac{d\rho}{2\rho}\sin(2q\rho\sin\theta) . \end{aligned} \tag{3.6}$$

When integrated over polar angle, the second part on the righthand side of this expression gives zero. The integral in the remaining part can be further simplyfied by using a Jacobi expansion and integrating out the polar angle

$$\sum_{n=-\infty}^{\infty}(-1)^n\int_\xi^\infty\frac{d\rho}{2\rho}J_{2n}(2q\rho)\int_0^{2\pi}d\theta e^{2in\theta} = \pi\int_\xi^\infty\frac{d\rho}{\rho}J_0(2\rho q) \equiv \pi Q_{\rm kin}(q\xi) , \tag{3.7}$$

where J_l is the l-th orther Bessel function of the first kind.

The second vortex position dependent contribution to the energy comes solely from the core. Let us consider the energy contribution

$$U = d_z\int d^2x\Psi^*(\mathbf{x})\left[V_{\rm OL}(\mathbf{x})+\frac{g}{2}|\Psi(\mathbf{x})|^2-\mu\right]\Psi(\mathbf{x}) . \tag{3.8}$$

Alternatively, this term is written as $U = E_\infty - U_{\rm core}(\mathbf{u})$, where E_∞ is a divergent constant equal to the energy of the condensate without a vortex and $U_{\rm core}(\mathbf{u})$ the contribution of the region excluded by the core of the vortex. Since the latter depends

on the vortex coordinates this contribution must be taken into account which gives

$$\begin{aligned} U_{\rm core}(\mathbf{u}) &= -d_z \int_{\rm core} d^2x \left[\frac{g}{2} n_{\rm TF}(\mathbf{x}) n_{\rm TF}(\mathbf{x}) + (V_{\rm OL}(\mathbf{x}-\mathbf{u}) - \mu) n_{\rm TF}(\mathbf{x})\right] \\ &= \frac{d_z}{2g} \int_{\rm core} d^2x [\mu - V_{\rm OL}(\mathbf{x}-\mathbf{u})]^2 \\ &\simeq -\frac{d_z \mu}{g} \int_{\rm core} d^2x V_{\rm OL}(\mathbf{x}-\mathbf{u}) + O(s^2 E_{\rm R}^2) \; . \end{aligned} \tag{3.9}$$

Performing the integral on a disk with radius ξ we arrive at the same form as in equation (3.6). The only difference is the prefactor, which depends on $q\xi$,

$$Q_{\rm core}(q\xi) = \frac{J_1(2q\xi)}{2q\xi} \; . \tag{3.10}$$

Consistent with our previous remarks, this contribution of the vortex core to the position dependent energy is smaller than the kinetic energy contribution. It adds to the latter contribution given in equation (3.7) and hence we define $Q \equiv Q_{\rm kin} + Q_{\rm core}$. Putting things together, the potential energy of a vortex described by the *ansatz* of equation (3.4) in a two dimensional optical lattice is given by[2]

$$U_{\rm pin}(\mathbf{u}) = \frac{d_z}{8a_s} s E_{\rm R} Q(q\xi) [\cos(2qu_x) + \cos(2qu_y)] \; . \tag{3.11}$$

It is clearly seen that the potential energy is minimal if the vortices are located at the maxima of the optical potential. This is expected, since at these maxima the condensate density, and hence the kinetic energy associated with the superfluid motion, is minimal. The expression in equation (3.11) is regarded as a pinning potential experienced by vortices in a condensate loaded in a optical lattice.

3.1.2 Vortex interactions

The interaction energy of two vortices must be known explicitly to calculate the ground state structure of vortex lattices. We calculate this interaction energy by using the following *ansatz* for the condensate wave function

$$\Psi(\mathbf{x}) = \sqrt{n}\, \Theta(R - |\mathbf{x}|)\, \Theta\big[|\mathbf{x}-\mathbf{u}|/\xi - 1\big]\, \Theta\big[|\mathbf{x}+\mathbf{u}|/\xi - 1\big] \exp[i\phi(\mathbf{x},\mathbf{u}) + i\phi(\mathbf{x},-\mathbf{u})] \; . \tag{3.12}$$

This form is a generalization of the *ansatz* in equation (3.4) to the case of two vortices in a disk-shaped condensate with radius R and average density n, oppositely displaced over a distance $|\mathbf{u}|$ from the origin. The reason that we do not explicitly take into account the spatial inhomogeneity of the condensate density due to the optical lattice potential in the calculation of the vortex interaction energy, is that most of the vortices in the vortex lattice are separated by more than one optical lattice constant,

[2] See also reference [83], which treats the limit of a small number of condensate atoms, as opposed to the Thomas-Fermi regime we consider here.

such that the effect of a spatially varying density profile on the vortex interactions is averaged out. In the relevant limit where the healing length is small compared to the system size, the only significant contribution comes from the kinetic energy of the condensate. For simplicity we place the vortices along the x-axis, $(u_x, u_y) = (\frac{r}{2}, 0)$, which leads for the energy of the system to

$$\begin{aligned} V(r) &= \frac{\hbar^2 d_z n}{2M} \int_0^{2\pi} d\theta \int_0^R d\rho\rho \frac{-64\rho^2}{r^4 + 16\rho^4 - 8r^2\rho^2 \cos 2\theta} \\ &= 128\pi \frac{\hbar^2 d_z n}{2M} \int_0^R d\rho\rho \frac{\rho^2}{16\rho^4 - r^4} \mathrm{sgn}(4\rho^2 - r^2) \ . \end{aligned} \tag{3.13}$$

Here ρ is the radial coordinate and θ is the polar angle. The effect of the condensate density profile is incorporated by simply excluding the contribution of the vortex cores from the expression in equation (3.13) such that

$$\begin{aligned} V(r) &= \frac{64\pi\hbar^2 d_z n}{M} \left[-\int_0^{(r-\xi)/2} d\rho\rho \frac{\rho^2}{16\rho^4 - r^4} + \int_{(r+\xi)/2}^R d\rho\rho \frac{\rho^2}{16\rho^4 - r^4} \right] \\ &= -\frac{\pi\hbar^2 d_z n}{M} \lim_{\tilde{R}\to\infty} \log \left[\frac{16\tilde{r}^6 - 4\tilde{r}^4 + 4\tilde{r}^2 - 1}{\tilde{r}^4(16\tilde{R}^4 - \tilde{r}^4)} \right] \ , \end{aligned} \tag{3.14}$$

where we defined $\tilde{R} \equiv R/\xi$ and $\tilde{r} \equiv r/\xi$ and also took the limit $\tilde{R} \to \infty$. The latter result is divergent with increasing system size. The finite, interaction energy of the two vortex configuration is isolated by subtracting the divergent constant $\frac{\pi\hbar^2 d_z n}{M} \lim_{\tilde{R}\to\infty} \log[1/\tilde{R}^4]$ from the expression in equation (3.14) and evaluating the limit $\tilde{R} \to \infty$. The resulting expression does not depend on the system size and behaves like

$$V(r) = -\frac{2\pi\hbar^2 d_z n}{M} \log\left(\frac{r}{\xi}\right) \ , \tag{3.15}$$

for $r \gg \xi$. This is the well-known long range interaction potential experienced by singly quantized vortices in two dimensions [90].

In the next section we will use the results for the vortex pinning potential and the vortex interaction energy to calculate the energy of a lattice of vortices.

3.2 Energy of a vortex lattice in a periodic potential

In principle, to calculate the equilibrium positions of the vortices, we have to minimize the total energy as a function of the coordinates of the vortices. Clearly, for a large number of vortices this is unfeasible. It is known, however, that in the limit of strong pinning, the vortices form regular lattices [76, 77, 78, 79, 80]. Therefore, to find the phase diagram of the system, we minimize the energy of the system assuming that the vortices form a regular lattice. This procedure neglects the fact that for small pinning potential the hexagonal Abrikosov vortex lattice is slightly distorted by the pinning potential [80].

To carry out the above minimization procedure, it is easiest to parameterize a unit cell of the vortex lattice for a given filling factor ν. The filling factor is defined as the number of vortices per pinning center, i.e., per minima of the pinning potential. In terms of the density of vortices it is equal to $\nu = n_v a^2$, where n_v is the two-dimensional density of vortices that is set by the rotation frequency Ω as $n_v = M\Omega/(\pi\hbar)$ [37], and $a = \pi/q$ is the optical lattice constant.

We consider commensurate filling factors smaller than one, i.e, $\nu = \frac{1}{k}$, with k a positive integer. All possible vortex lattice unit cells corresponding to such commensurate vortex lattices at a particular filling factor can be found by factorizing k in products $l \cdot m$, with l and m positive integers, and arranging vortices on the sides of rectangles of size $la \times ma$, as shown in figure 3.1. Varying the vortex positions along the sides of the rectangle, keeping the area of the unit cell constant, gives all possible primitive commensurate lattice structures for the vortex lattice. For a vortex lattice of filling ν this procedure is parameterized by

$$\mathbf{u}(\alpha, \beta\ ;\ l, m) \ = \ a \begin{pmatrix} \sqrt{1+\alpha l \beta m} & \alpha l \\ \beta m & \sqrt{1+\alpha l \beta m} \end{pmatrix} \begin{pmatrix} l n_x \\ m n_y \end{pmatrix} , \tag{3.16}$$

with $n_i \in \mathbb{Z}$ and $0 \leq \alpha, \beta \leq \frac{1}{2}$. Notice that the transformation matrix in the above expression preserves the area of the unit cell, since its determinant equals unity. This ensures that we are considering lattice configurations with equal vortex density. The more familiar parameters of a unit cell of a two-dimensional lattice, the angle φ between the primitive lattice vectors and the ratio of their lengths, $\kappa = L_1/L_2$, are related to α and β by

$$\begin{aligned} \frac{\cos\varphi}{\kappa} &= \frac{m(\alpha l + \beta m)\sqrt{1+\alpha l \beta m}}{l[1+\beta m(\alpha l + \beta m)]} , \\ \frac{\sin\varphi}{\kappa} &= \frac{m}{l[1+\beta m(\alpha l + \beta m)]} . \end{aligned} \tag{3.17}$$

The interaction energy $E_{\rm int}$ per unit cell as function of φ and κ for an infinite two-dimensional lattice of vortices subject to the logarithmic interaction potential of equation (3.15) was calculated by Campbell *et al.* [91]. Cast in a dimensionless form their result reads

$$\begin{aligned} \tilde{E}_{\rm int} \equiv \frac{E_{\rm int}}{(\pi\hbar^2 d_z n/M)} &= \frac{\pi}{6}\frac{\sin\varphi}{\kappa} - \log\left[2\pi\left(\frac{\sin\varphi}{\kappa}\right)^{\frac{1}{2}}\right] \\ &- \log\left\{\Pi_{j=1}^{\infty}[1 - 2e^{-2\pi j|\sin\varphi|/\kappa}\cos\left(2\pi j\frac{\cos\varphi}{\kappa}\right)\right. \\ &\left. + e^{-4\pi j|\sin\varphi|/\kappa}]\right\} . \end{aligned} \tag{3.18}$$

It is important to realize that the interaction energy per vortex is divergent for an infinite vortex lattice, and that the above expression gives the relative interaction energy for configurations with equal vortex density. The absolute minimum of the dimensionless interaction energy in equation (3.18) corresponds to a hexagonal vortex

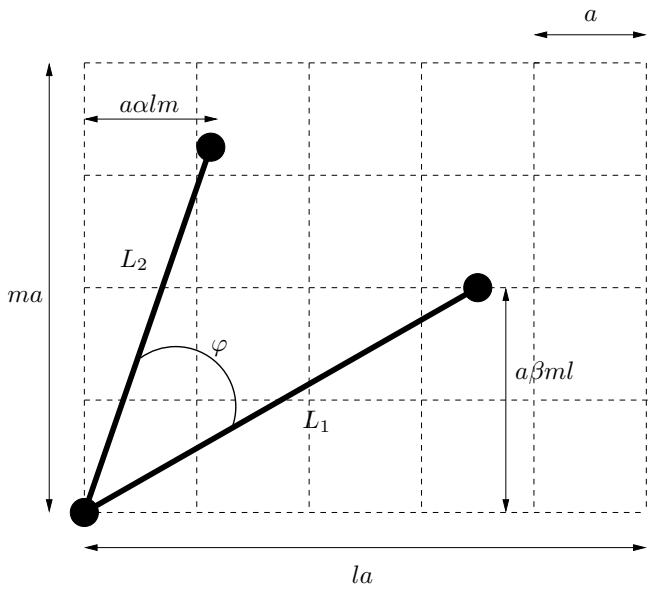

Figure 3.1: Two ways to parametrize the unit cell of a vortex lattice, using parameters $(\alpha l, \beta m)$ and (φ, κ), with $\kappa = L_1/L_2$. The relation between those parametrizations is given by the expressions in equation (3.17). The grid indicates the pinning potential with lattice constant a.

lattice structure, i.e., the Abrikosov vortex lattice with $l = m = \sqrt{k}$ and $\alpha l = \beta m = \sqrt{1/\sqrt{3} - 1/2}$ or $(\varphi, \kappa) = (\pi/3, 1)$, and is equal to $\tilde{E}_{\rm int} = -1.32112$. Note that this lattice is incommensurate with the optical lattice.

The pinning energy per unit cell is found by substituting equation (3.16) in equation (3.11), summing over all n_x and n_y, and dividing the result by the number of unit cells,

$$\begin{aligned} E_{\rm pin}(\alpha, \beta\,;\, l, m) &= \lim_{P\to\infty} \frac{1}{4P^2} \sum_{n_x=-P}^{P} \sum_{n_y=-P}^{P} U_{\rm pin}[\mathbf{u}(\alpha, \beta\,;\, l, m)] \\ &= -\frac{d_z}{8a_s} s E_{\rm R} Q(q\xi)[\delta_{\beta m\in\mathbb{Z}} + \delta_{\alpha l\in\mathbb{Z}}]\,. \end{aligned} \tag{3.19}$$

This form of the pinning energy per unit cell is what we expect on an infinite lattice. Only if the vortices form a lattice that is commensurate with the optical lattice, they give a nonzero contribution to the pinning energy. This is why we consider only commensurate fillings, since we expect structural transitions at these fillings. Incommensurate vortex lattices have zero potential energy per unit cell on average. For $\nu \leq 1$ there are three possible outcomes for the pinning energy in equa-

tion (3.19). *i*) A phase in which all the vortices are pinned by optical lattice maxima at $E_{\rm pin} = -\frac{d_z}{4a_s} s E_{\rm R} Q(q\xi)$, *ii*) a phase in which a half of the vortices is pinned at $E_{\rm pin} = -\frac{d_z}{8a_s} s E_{\rm R} Q(q\xi)$, and *iii*) an unpinned phase at $E_{\rm pin} = 0$ for any vortex lattice that is incommensurate with the optical lattice. The precise geometry of the unit cell of these vortex lattices is determined further by minimization of the interaction energy in equation (3.18). Of course, the structure of the unpinned phase is always hexagonal, corresponding to the global minimum of the interaction energy.

To end this section, we would like to point out that, since the interaction energy of the vortex lattice is derived by summing the expression for the interaction energy of two vortices over all pairs of vortices, we have implicitly assumed that the vortex density is so low that the vortex cores never overlap, and that we are therefore allowed to neglect three-vortex interactions, and interactions of higher order. A similar argument validates the derivation of the pinning energy of the vortex lattice by summing the single-vortex pinning potential over the number of vortices. In the numerical calculations of Pu *et al.* [89], these authors observed that for filling larger than one the vortices form pinned phases where pairs of vortices are pinned, and hence two vortices get very close together. Since our approximations break down in this case, we study only phases with a filling factor smaller than one.

3.3 Phase diagrams

The energy per unit cell of the vortex lattice, obtained by adding the pinning energy of equation (3.19) and the interaction energy of equation (3.18), enables us to calculate the zero-temperature phase diagram of the vortex lattice structure at a certain filling. As already mentioned, we consider systems with filling factor $\nu = \frac{1}{k}$ with k a nonnegative integer larger than one.

The dimensionless energy per unit cell of the vortex lattice reads

$$\left(\frac{4a_s}{\mu d_z}\right) E(\alpha, \beta\,;\, l, m) = \tilde{E}_{\rm int}(\alpha, \beta\,;\, l, m) - \frac{1}{2}\frac{s E_{\rm R}}{\mu} Q(q\xi)[\delta_{\beta m \in \mathbb{Z}} + \delta_{\alpha l \in \mathbb{Z}}]\,, \qquad (3.20)$$

where we used that $\mu \simeq gn$. It is most convenient to minimize this expression in the plane spanned by the dimensionless parameters $q\xi$ and $\frac{sE_{\rm R}}{\mu}$. This leads to the three phases discussed in the previous section. However, the presence of the half-pinned vortex configuration depends on the filling factor, implying different phase diagrams for even and odd k. Since the structure of the lattice does not change continuously, the phases are separated by a first-order transition.

In the case of even k, the half-pinned lattice is absent, since the pinning centers are distributed such that the minimum energy configuration is always a fully-pinned lattice. The phase diagram thus contains two distinct phases: a fully-pinned vortex lattice and the hexagonal Abrikosov lattice. The geometry of the fully-pinned vortex lattice is determined such that the interaction energy is minimal [76, 77, 78, 79, 80].

If k is an odd integer, the half-pinned lattice is present in the phase diagram if the

pinning energy and the interaction energy are of the same order. However, this phase exists only if the inter-vortex distance and the optical lattice constant are comparable in size.

We now discuss three specific examples in detail, that of $\nu = 1$, shown in figure 3.2, and that of $\nu = \frac{1}{2},\ \frac{1}{4}$ and $\nu = \frac{1}{5}$, which are shown in figure 3.3.

$\nu = 1$

If there is one pinning centre per vortex the phasediagram has the following structure. For a very weak optical potential we find that vortices arrange themselves on a triangular Abrikosov lattice (AB), with $\alpha = \beta = \sqrt{1/\sqrt{3} - 1/2}$, as expected. In this phase, with $\tilde{E}_{\rm int} = -1.32112$, the interactions dominate over the pinning. On the other hand, when the pinning energy dominates over the interaction, we find the square pinned lattice ($\alpha = \beta = 0$) [80]. This phase has $\tilde{E}_{\rm int} = -1.31053$. In the intermediate regime, where the pinning and interactions are equally important, we find a phase in which half of the vortices are pinned (HP) [80], and the lattice has a triangular structure ($\alpha = \frac{1}{2},\ \beta = 0$ and $\tilde{E}_{\rm int} = -1.31800$). In the zero-temperature phase diagram, shown in figure 3.2, the different phases are separated by first-order phase transitions and the phase boundaries are given by

$$\left(\frac{sE_{\rm R}}{\mu}\right)_{\rm hexagonal-halfpinned} = \frac{.00623}{Q(q\xi)}, \quad \left(\frac{sE_{\rm R}}{\mu}\right)_{\rm halfpinned-squarepinned} = \frac{.01494}{Q(q\xi)}. \tag{3.21}$$

$\nu = \frac{1}{2}$

For $\nu = \frac{1}{2}$ the phase diagram contains two phases and is depicted in figure 3.3 (a). For weak pinning the vortices are not pinned and form a hexagonal Abrikosov lattice. For strong pinning all vortices are located on the minimum of the pinning potential, and form a square lattice with $(\alpha, \beta) = (0, \frac{1}{2})$ and $(l, m) = (1, 2)$. Note that, as opposed to the $\nu = 1$ case, which also has a square and pinned vortex lattice in the strong pinning regime, in this case the vortex lattice is rotated over an angle $\frac{\pi}{4}$ with respect to the optical lattice.

$\nu = \frac{1}{4}$

If there are four pinning centra per vortex, corresponding to $k = 4$, we find for large strength of the optical lattice a fully pinned vortex lattice[3] with $(\alpha, \beta) = (\frac{1}{2}, 0)$, $l = 4$

[3]Apart from breaking the translational symmetry, such a triangular vortex lattice also breaks a discrete symmetry, because there are several distinct possibilities to form the triangular lattice configuration. In this particular case the discrete symmetry is Z_4. This additional symmetry breaking implies the existence

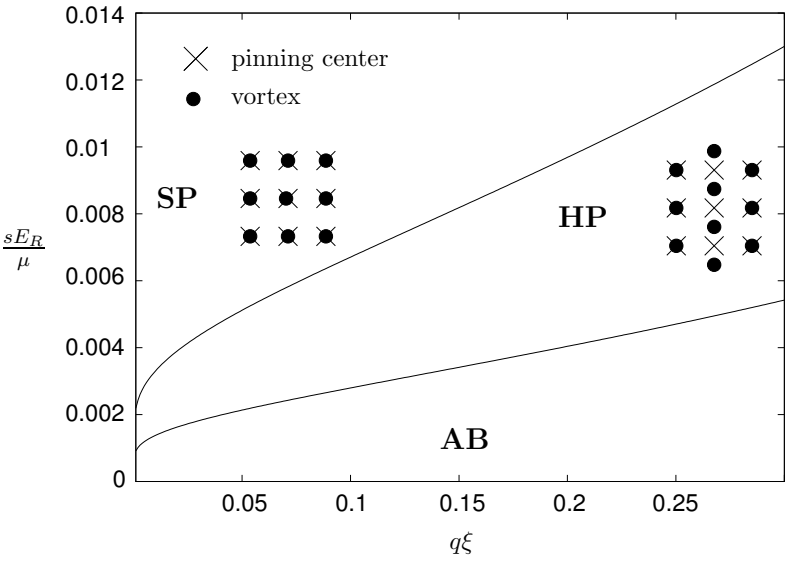

Figure 3.2: Vortex phase diagram of a Bose-Einstein condensate in a two-dimensional optical square lattice, with one vortex per unit cell of the optical lattice. Three phases are relevant: a square and fully-pinned configuration (SP), a triangular configuration where half of the vortices are located at the pinning centers (HP), and the unpinned triangular Abrikosov vortex lattice (AB).

and $m = 1$. The interaction energy per unit cell of the vortex lattice of this configuration is $\tilde{E}_{\rm int} = -1.31055$. At small optical lattice strength we find the unpinned triangular Abrikosov or hexagonal vortex lattice. The phases are separated from each other by a first order phase transition. The phase boundary is given by

$$\left(\frac{sE_{\rm R}}{\mu}\right)_{\rm hexagonal-pinned} = \frac{0.01057}{Q(q\xi)}. \tag{3.22}$$

It is important to note that, contrary to the case of $\nu = \frac{1}{2}$ and $\nu = 1$ [81], the geometry of the fully-pinned vortex lattice is in this case triangular. Since a fully-pinned square lattice has the same pinning energy as this triangular lattice, the interaction energy favors the latter. The phase diagram for this filling is shown in figure 3.3 (b).

of domain walls between triangular vortex lattices that are oriented differently. We do not consider such configurations here.

$\nu = \frac{1}{5}$

At $k = 5$ we find three phases. First, for large strength of the optical lattice we have a fully-pinned vortex lattice with $(\alpha, \beta) = (\frac{2}{5}, 0)$, $l = 5$, $m = 1$ and interaction energy $\tilde{E}_{\rm int} = -1.31055$. At intermediate optical lattice strengths we find an half pinned phase with $(\alpha, \beta) = (\frac{1}{2}, 0)$, $l = 5$ and $m = 1$. The interaction energy per unit cell of this configuration equals $\tilde{E}_{\rm int} = -1.31849$. At small lattice strength we find again the Abrikosov vortex lattice. The phase boundaries between these phases are given by

$$\left(\frac{sE_{\rm R}}{\mu}\right)_{\rm pinned-halfpinned} = \frac{0.01588}{Q(q\xi)}, \qquad \left(\frac{sE_{\rm R}}{\mu}\right)_{\rm hexagonal-halfpinned} = \frac{0.00526}{Q(q\xi)}. \tag{3.23}$$

Similar to the $\nu = \frac{1}{2}$ case. we find that the fully-pinned vortex lattice has a square geometry, and is now rotated over an angle $\tan^{-1}\left(\frac{1}{2}\right)$ with respect to the optical lattice. Generally, if the fully-pinned vortex lattice has a square geometry, then for filling factor $\nu = \frac{1}{k_1^2+k_2^2}$, with k_1 and k_2 integer, the fully-pinned vortex lattice will be rotated over an angle $\tan^{-1}\left(\frac{k_2}{k_1}\right)$ with respect to the optical lattice.

Contrary to the above mentioned filling factors, but similar to the $\nu = 1$ case, there is an intermediate triangular vortex lattice, where half of the vortices is pinned.

3.3.1 One-dimensional optical lattice

For a one-dimensional optical lattice the pinning potential experienced by a single vortex equals $U_{\rm 1D}(\mathbf{u}) = \frac{d}{8a_s} sE_{\rm R}Q(q\xi)\cos(2qu_x)$ and hence the minima of $U_{\rm 1D}$ act as pinning "valleys". The pinning energy per vortex reads $E^{\rm 1D}_{\rm pin} = -\frac{d}{8a_s} sE_{\rm R}Q(q\xi)\delta_{\beta,0}$ within the parametrization in equation (3.16). Two phases are distinguished in this case, i.e., a pinned triangular lattice (PT), shown in figure 3.4, and the unpinned Abrikosov vortex lattice. Interestingly, the interactions always favor a triangular lattice since the vortices are allowed to arrange freely in the y-direction.

Consider now the case that the wavenumber of the optical lattice is such that the AB lattice and the PT lattice coincide, i.e., $q_0 \equiv 2\pi\sqrt{3}/(3L)$, with L the intervortex distance. If this configuration is disturbed by changing the optical lattice wavenumber to arbitrary q there will be a competition between the AB lattice and the PT lattice. The unit cell of the latter is, for wavenumber q and at equal vortex density, described by

$$\frac{\cos\varphi}{\kappa} = \frac{2}{1+3\left(\frac{q_0}{q}\right)^4}, \qquad \frac{\sin\varphi}{\kappa} = \frac{2\sqrt{3}\left(\frac{q_0}{q}\right)^2}{1+3\left(\frac{q_0}{q}\right)^4}. \tag{3.24}$$

The interaction energy per unit cell is found by substitution of equation (3.24) in equation (3.18). From this we find the zero-temperature phase diagram, depicted in figure 3.4 for various values of the healing length. The generic behavior is such that for given strength of the optical lattice and for small deviations from q_0, the vortex

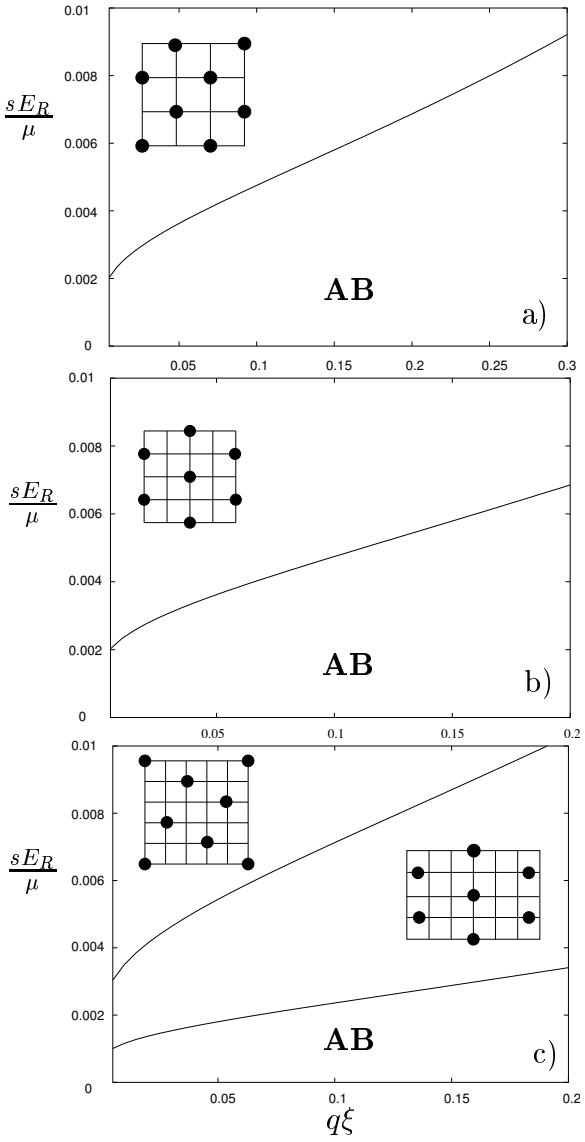

Figure 3.3: Vortex phase diagram, at zero temperature, of a Bose-Einstein condensate in a two dimensional optical square lattice, with filling factor $n_v = \frac{1}{2}$ (a), $n_v = \frac{1}{4}$ (b) and $n_v = \frac{1}{5}$ (c) respectively.

lattice stays pinned, i.e., the vortices are dragged along with the pinning valleys.

At certain q the phase boundary is crossed. Then the vortices "jump" back to their original positions, forming an Abrikosov lattice again.

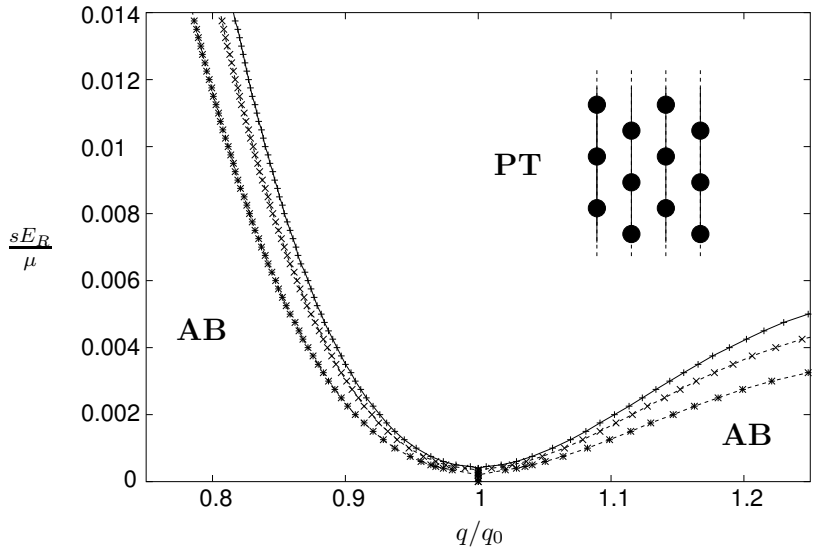

Figure 3.4: Vortex phase diagram of a Bose-Einstein condensate in a one-dimensional optical lattice. Two phases are relevant: a pinned triangular configuration (PT), and the unpinned triangular Abrikosov vortex lattice (AB). We calculated the phase boundaries for $\xi = .01\pi/q_0$ (+), $\xi = .005\pi/q_0$ ($\times$) and $\xi = .001\pi/q_0$ ($*$). Note that at the line $q/q_0 = 1$ the phases coincide.

3.4 Pinning of vortices in two-component condensates

In this section we study the influence of a two-dimensional optical potential on vortex lattices in a mixture of Bose-Einstein condensates of two different species. Our results also apply to a Bose-Einstein condensate that consists of two hyperfine components, provided the number of atoms in each component is conserved. Along the lines of section 3.1, 3.2 and 3.3 we calculate the ground state phase diagram for two coupled condensates each containing a vortex lattice at filling $\nu_i = 1$ with the optical potential. Note that the fact that we take the filling factor to be the same in both species implies that the masses of both species are approximately equal.

A system of two coupled Bose-Einstein condensates is described by the following

hamiltonian

$$H = \sum_{i=1,2} \int \mathrm{d}\mathbf{r} \Psi_i^* \left[\frac{-\hbar^2 \nabla^2}{2M_i} + V_{\mathrm{OL}}(\mathbf{x}) - \mu_i \right] \Psi_i + \int \mathrm{d}\mathbf{r} \left[\frac{1}{2} g_1 |\Psi_1|^4 + \frac{1}{2} g_2 |\Psi_2|^4 + g_{12} |\Psi_1|^2 |\Psi_2|^2 \right], \quad (3.25)$$

with $g_i = 4\pi\hbar^2 a_i / M_i$ and $g_{12} = 2\pi\hbar^2 a_{12}/M_{ij}$. Here a_{12} is the scattering length between unlike species and the reduced mass is given by $M_{ij} = M_i M_j/(M_i + M_j)$.

In the absence of the optical potential, Mueller and Ho [63] and Kasamatsu *et al.* [64] theoretically predicted smooth transitions between hexagonal lattices in both components at small (intra species) interactions and interlaced square vortex lattices at larger interaction. These square lattices where observed very recently by Schweikhard *et al.* [40]. However, the above-mentioned transition is caused by the fact that the interaction energy is minimized if the overall density is as smooth as possible. Since we take a step function for the density profile of the vortex, this density effect is not included in our calculations. Therefore our results only make sense in the regime where this density effect is dominated by the optical potential, i.e., in the strong-pinning limit. To ensure this, the requirement $\left(\frac{sE_R}{\mu_i}\right) Q(q\xi_i) \gg \frac{g_{12}}{g_i}$ must be satisfied. This implies that we must have that $g_i \gg g_{12}$, since we assumed that $sE_R < \mu_i$. It must be stressed that this is quite restricting as at the present day there is no experimental atomic system known which meet these requirements. However, one might expect that near an interspecies Feshbach resonance this regime of parameters is realizable. Therefore, we study the fully-pinned and half-pinned lattices and the phase transition between them.

A non-rotating two-component condensate phase separates if $g_{12} > \sqrt{g_1 g_2}$ [92, 93]. The condensates mutually exclude each other, even in the absence of external potentials [94] or *with* rotation [64]. The vortex ground state in the latter case will not be given by a regular lattice, in general. In our calculations we restrict ourself to the regime where the system does not phase separate. In this regime, the coupling parameters satisfy $g_i > 0$ and $g_1 g_2 > g_{12}^2$, which falls safely within the approximation discussed above. We define the dimensionless parameter $\chi^2 \equiv g_{12}^2/g_1 g_2$, for which these criteria imply $0 < \chi^2 < 1$.

Solving the coupled equations for the condensate wave functions, derived from the hamiltonian of equation (3.25) in the Thomas-Fermi approximation, leads to the following density profile in component i

$$n_{\mathrm{TF}}^i(\mathbf{r}) = |\Psi_i|^2 = \frac{1}{g_i} \frac{[\mu_i - V_{\mathrm{OL}}(\mathbf{r})]}{1-\chi^2} + \frac{1}{g_{12}} \frac{[\mu_j - V_{\mathrm{OL}}(\mathbf{r})]}{1 - \frac{1}{\chi^2}}, \quad j \neq i \quad (3.26)$$

We use the variational *ansatz* for the condensate wave function containing a vortex in component i

$$\Psi_i(\mathbf{x}) = \sqrt{n_{\mathrm{TF}}^i(\mathbf{x})}\, \Theta\big[|\mathbf{x} - \mathbf{u}|/\xi_i - 1\big] \exp[i\phi_i(\mathbf{x}, \mathbf{u})], \quad (3.27)$$

with $\xi_i = 1/\sqrt{8\pi a_i n_i}$ and $n_i = (\mu_i - sE_{\rm R})/g_i$. Furthermore, we assume that vortices in different components do not interact. As explained before, in particular we neglect the effect of the density profile caused by a vortex in one component on the vortices in the other component, which, in the absence of an optical potential, leads to the structural transitions discussed by Mueller and Ho [63] and Kasamatsu *et al.* [64]. Within each component, the vortex interactions are logarithmic, as derived in section 3.1.2.

The pinning potential which is experienced by the vortex can be calculated along the lines of section 3.1.1. The first contribution, coming from the kinetic energy term of the hamiltonian in equation (3.25), is equal to

$$U^i_{\rm kin}(\mathbf{u}) = \frac{d_z}{8a_i} sE_{\rm R} Q_{\rm kin}(q\xi_i) G_i(g_1, g_2, g_{12}) \left[\cos(2qu_x) + \cos(2qu_y)\right] \ , \tag{3.28}$$

with $Q_{\rm kin}$ given by equation (3.7). The difference with the single component case is the appearance of the factor

$$G_i(g_1, g_2, g_{12}) = \frac{g_{12} - g_i\chi^2}{g_{12}(1-\chi^2)} \ . \tag{3.29}$$

This factor is completely dependent on the various interaction strengths. The other significant (position-dependent) contribution, coming from the vortex core, involves more work,

$$\begin{aligned}
U^i_{\rm core}(\mathbf{u}) &= -d_z \int_{\rm core} {\rm d}^2x \left[\frac{1}{2} g_i |\Psi_i|^4 + (V_{\rm OL} - \mu_i)|\Psi_i|^2 + \frac{1}{2} g_{12} |\Psi_1|^2 |\Psi_2|^2\right] \\
&= -d_z \int_{\rm core} {\rm d}^2x \left\{ \frac{g_i}{2} \left[\frac{(\mu_i - V_{\rm OL})^2}{g_i^2(1-\chi^2)^2} + \frac{(\mu_j - V_{\rm OL})^2}{g_{12}^2(1-1/\chi^2)^2} \right.\right. \\
&\qquad \left.\left. + 2\frac{(\mu_i - V_{\rm OL})(\mu_j - V_{\rm OL})}{g_i g_{12}(1-\chi^2)(1-1/\chi^2)} \right] \right. \\
&+ \left[V_{\rm OL} - \mu_i + \frac{g_{12}}{2} \left(\frac{(\mu_j - V_{\rm OL})}{g_j(1-\chi^2)} + \frac{(\mu_i - V_{\rm OL})}{g_{12}(1-1/\chi^2)} \right) \right] \\
&\qquad \left. \times \left[\frac{(\mu_i - V_{\rm OL})}{g_i(1-\chi^2)} + \frac{(\mu_j - V_{\rm OL})}{g_{12}(1-1/\chi^2)} \right] \right\} \\
&= -\frac{d_z}{g_i} \frac{1}{\chi^2 - 1} \left[\frac{g_{12}(\mu_i + \mu_j)}{2g_j} - \mu_i \right] \int_{\rm core} {\rm d}^2x V_{\rm OL}(\mathbf{x} - \mathbf{u}) + {\rm O}(s^2 E_R^2) \ .
\end{aligned} \tag{3.30}$$

If we assume that $\mu_i \approx \mu_j$ we find a contribution similar to equation (3.28). The prefactor in this case is given by $Q_{\rm core}(q\xi)$ which is defined in equation (3.10). The total pinning potential experienced by a vortex in component i due to the optical lattice is equal to

$$U^i_{\rm pin}(\mathbf{u}) = \frac{d_z}{8a_i} sE_{\rm R} [Q_{\rm kin}(q\xi_i) + Q_{\rm core}(q\xi_i)] G_i(g_1, g_2, g_{12}) \left[\cos(2qu_x) + \cos(2qu_y)\right] . \tag{3.31}$$

This energy is dependent on the ratio of the coupling parameters. The pinning energy is minimized on lattice maxima in both components in the regime where it is the dominant energy scale. Therefore, vortices in both components tend to be on the same position.

In order to find the vortex phase diagram we minimize the interaction and pinning energy in each component, as in section 3.3. We assume (again) $\mu_i \approx \mu_j = \mu$. This implies $\xi_i \approx \xi_j = \xi$. As mentioned before, we are only interested in lattice types which are fully-pinned or half-pinned. The phase boundary between the fully-pinned and half-pinned vortex lattices (commensurable with the optical lattice) in each component is given by

$$\left(\frac{sE_{\mathrm{R}}}{\mu}\right)_i = \frac{0.01494}{Q(q\xi)G_i(g_1,g_2,g_{12})} \,. \tag{3.32}$$

To find all possible lattice types in the two-component system it is most convenient to parametrize the coupling parameters by $g_1 = \kappa g_{12}\sin(\gamma)$ and $g_2 = \kappa g_{12}\cos(\gamma)$. By varying γ one scans along an circle segment in the (g_1, g_2)-plane. The non-phase separated regime in terms of the new parameters is given by $\kappa > \sqrt{2}$ and $\gamma_- < \gamma < \gamma_+$ with

$$\gamma_\pm = \arccos\left[\sqrt{\frac{1}{2}\left(1 \pm \frac{\sqrt{\kappa^4-4}}{\kappa^2}\right)}\right] \,. \tag{3.33}$$

We find that the phase diagram contains four different vortex lattices. In figure (3.5) the phase diagram and the lattice geometry are displayed for $q\xi = 0.05$ and $\kappa = 100$. Notice that the two-component phase diagram has a straightforward interpretation in terms of coexistence of phases found in the single-component case. For strong pinning the vortex lattices are both fully-pinned. For the filling under consideration ($\nu = 1$) the vortices in both components therefore form a square lattice. Depending on the relative strength of the interaction, determined by the parameter γ, the vortex lattice in one of the components will change first to the half-pinned triangular geometry, as one lowers the strength of the optical potential. For sufficiently weak pinning potential both vortex lattices assume this structure.

3.5 Collective modes

In this section we calculate the dispersion of the collective modes of the pinned vortex lattices. In principle, this requires the calculation of the energy of the system for small displacements $\mathbf{u}(\mathbf{r}_i)$ of the vortices from their equilibrium positions $\mathbf{r}_i \equiv r_{ix}\hat{x} + r_{iy}\hat{y}$. In first instance, the energy of the system is then given by

$$\begin{aligned} E[\mathbf{u}] &= \frac{d_z s E_{\mathrm{R}} Q(q\xi)}{8a_s} \sum_i \left\{\cos\left[2q(r_{ix}+u_x(\mathbf{r}_i))\right] + \cos\left[2q(r_{iy}+u_y(\mathbf{r}_i))\right]\right\} \\ &- \frac{\pi\hbar^2 d_z n}{M} \sum_{i\neq j} \log\left|\frac{\mathbf{r}_i + \mathbf{u}(\mathbf{r}_i) - \mathbf{r}_j - \mathbf{u}(\mathbf{r}_j)}{\xi}\right| \,. \end{aligned} \tag{3.34}$$

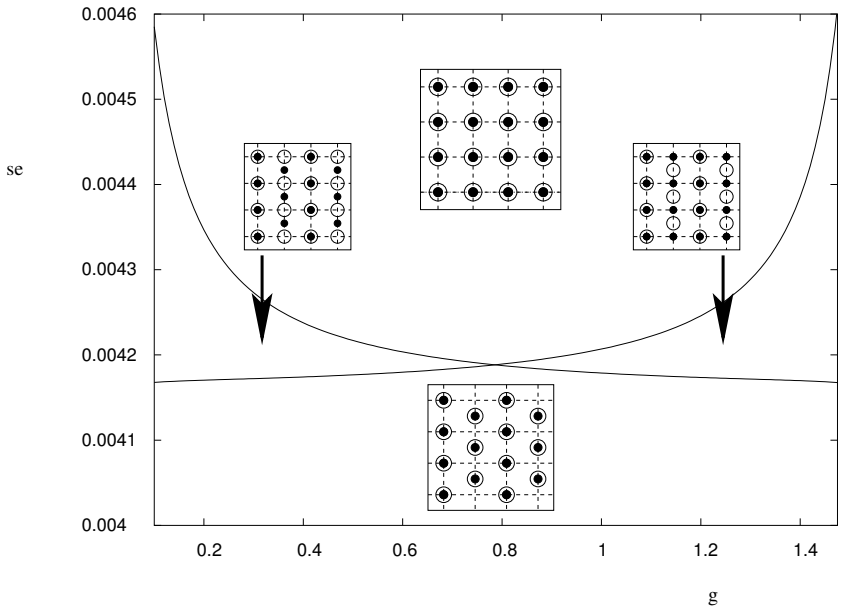

Figure 3.5: Vortex phase diagram of a rotating two-component condensate in the presence of an optical lattice, at commensurate filling, $\nu_i = 1$. The phase diagram is plotted as function of the dimensionless parameter $\gamma = \arctan(g_1/g_2)$. Black dots and circles represent vortices in different components. The dashed lines represent the pinning potential. We took $\kappa = 100$ and $q\xi = 0.05$ which implies $Q(0.05) \approx 3.612$.

We perform a Fourier transform

$$\mathbf{u}(\mathbf{r}_i) = \frac{1}{\sqrt{N_x N_y}} \sum_{\mathbf{k}} \mathbf{u}(\mathbf{k}) e^{i\mathbf{k}\cdot\mathbf{r}_i} \ , \tag{3.35}$$

where N_α is the number of vortices along the α direction of the vortex lattice, and the momentum sum is restricted over values $k_\alpha = 2\pi n_\alpha / L_\alpha$ in the first Brillouin zone, where n_α is an integer and L_α is the size of the vortex lattice in the α direction. Note that throughout this section we use Greek symbols to indicate two-dimensional Cartesian components, i.e., $\alpha, \beta \in \{x, y\}$. We also sum over repeated Greek indices.

We expect that after this Fourier transformation the energy of the vortex lattice for small displacements will, up to an irrelevant constant, be given by

$$E\left[\mathbf{u}\right] = \frac{1}{2} \sum_{\mathbf{k}} D_{\alpha\beta}(\mathbf{k}) u_\alpha(-\mathbf{k}) u_\beta(\mathbf{k}) \ , \tag{3.36}$$

where the so-called dynamical matrix is the sum of three contributions

$$D_{\alpha\beta}(\mathbf{k}) = D^{\mathrm{EL}}_{\alpha\beta}(\mathbf{k}) + D^{\mathrm{LR}}_{\alpha\beta}(\mathbf{k}) + D^{\mathrm{OL}}_{\alpha\beta}(\mathbf{k}) \ . \tag{3.37}$$

The first contribution $D^{\mathrm{EL}}_{\alpha\beta}(\mathbf{k})$ takes into account the interaction between neighboring vortices and follows from elasticity theory. Although the elastic constants that will enter in the expression for $D^{\mathrm{EL}}_{\alpha\beta}(\mathbf{k})$ can in principle be calculated from the interaction energy in equation (3.34), such a calculation is beyond the scope of this chapter, and we will adopt a more phenomenological point of view and write down the most general form for $D^{\mathrm{EL}}_{\alpha\beta}(\mathbf{k})$ allowed by symmetry arguments, for each lattice under consideration [95]. The second contribution

$$D^{\mathrm{LR}}_{\alpha\beta}(\mathbf{k}) = \frac{8\pi^2\hbar^2 d_z n}{AM} \frac{k_\alpha k_\beta}{k^2 + \lambda^{-2}} \ , \tag{3.38}$$

where A is the area of the unit cell of the vortex lattice, is independent of the structure of the lattice and follows from the long-range nature of the logarithmic interactions, which has to be taken into account separately [96, 97, 42]. Note that we have explicitly included a finite range λ of the logarithmic interactions, to ensure that $D^{\mathrm{LR}}_{\alpha\beta} \to 0$ as $k \to 0$. After taking the long wavelength limit, we can safely take $\lambda \to 0$. The final contribution $D^{\mathrm{OL}}_{\alpha\beta}(\mathbf{k})$ is due to the optical lattice.

The dispersion of the collective modes is determined by putting the determinant of the matrix

$$M_{\alpha\beta}(\mathbf{k}, \omega) = D_{\alpha\beta}(\mathbf{k}) - \epsilon_{\alpha\beta} 4\pi i n d_z \hbar\omega \ , \tag{3.39}$$

equal to zero. Here, $\epsilon_{\alpha\beta}$ is the antisymmetric Levi-Cevita tensor in two-dimensions, that takes into account the Euler dynamics of the vortices [37, 90].

We will now calculate the dynamical matrix for each type of vortex lattice considered in the previous section, i.e, for the hexagonal, half-pinned, and fully-pinned vortex lattice, in the long-wavelength limit, and use these results to calculate the phonon spectrum of the vortex lattice.

3.5.1 Hexagonal vortex lattice

For a hexagonal vortex lattice we have that [95]

$$D^{\mathrm{EL}}_{\alpha\beta}(\mathbf{k}) = K_H k_\alpha k_\beta + \mu_H \delta_{\alpha\beta} k^2 \,, \tag{3.40}$$

where K_H is the bulk modulus, and μ_H is the shear modulus of the hexagonal vortex lattice. Using this result together with equation (3.38), we find for the frequency of the collective modes in the absence of an optical lattice that

$$\hbar\omega_{\mathbf{k}} = \frac{k}{4\pi n d_z}\sqrt{\mu_H\left[\frac{8\pi^2\hbar^2 d_z n}{a_v^2 M} + (K_H+\mu_H)\,k^2\right]} \,. \tag{3.41}$$

For large wavelengths we have that $\hbar\omega_{\mathbf{k}} \simeq c_T k$, where the sound velocity of the so-called Tkachenko waves is given by

$$c_T = \frac{1}{4\pi n d_z}\sqrt{\frac{8\pi^2\mu_H\hbar^2 d_z n}{a_v^2 M}} \,. \tag{3.42}$$

We could now fix the value for the shear modulus of the vortex lattice μ_H by demanding that the Tkachenko sound velocity is equal to $\sqrt{\hbar\Omega/(4M)}$, the result known from the hydrodynamic theory of a vortex lattice [26, 98]. This would, however, not be consistent, since the value for μ_H should follow from the expression for the energy of the vortex lattice in equation (3.34), and may lead to a different sound velocity due to the variational approximations we have made in the description of the vortex lattice. Note that is crucial to take into account the long-range interactions of the vortices by means of the dynamical matrix in equation (3.38) to get a linear dispersion at long wavelengths, since an omission of this part in the dynamical matrix would lead to a quadratic dispersion. Moreover, we would like to point out that due to the fact that vortices are described by Euler dynamics we find only one mode, instead of two modes for the case of a lattice of particles that obey Newtonian dynamics.

The polarization of the vortex lattice phonons is determined by the eigenvector of the matrix in equation (3.39), corresponding to the eigenfrequency in equation (3.41). Generally, the displacements are given by $\mathbf{u}(\mathbf{r}_i,t) = \mathbf{u}_{\mathbf{k},0}e^{i\mathbf{k}\cdot\mathbf{r}_i - i\omega_{\mathbf{k}}t}$, where $\mathbf{u}_{\mathbf{k},0}$ is the eigenvector. For a wave in the y-direction we have that

$$\mathbf{u}_{\mathbf{k},0} \propto \begin{pmatrix} \frac{i\left[\frac{8\pi^2\hbar^2 d_z n}{a_v^2 M}+k_y^2\right]}{k_y\sqrt{\mu_H\left[\frac{8\pi^2\hbar^2 d_z n}{a_v^2 M}+(K_H+\mu_H)k^2\right]}} \\ 1 \end{pmatrix} \approx \begin{pmatrix} \frac{i}{\mu_H k_y}\sqrt{\frac{8\pi^2\mu_H\hbar^2 d_z n}{a_v^2 M}} \\ 1 \end{pmatrix} \,, \tag{3.43}$$

which shows that the vortices move on an ellipse with the long axis perpendicular to the direction of propagation. In the limit $\mathbf{k}\to 0$, the wave is almost transverse.

The translation symmetry of the system is broken explicitly in the presence of an optical lattice. The collective modes therefore acquire a gap, i.e., there is a minimum

amount of energy required to excite a phonon. Considering the part of the energy of equation (3.34) which corresponds to the pinning energy of the vortices and expanding it, we have, up to an irrelevant constant,

$$E^{\mathrm{OL}}[\mathbf{u}] = -2q^2 \frac{d_z s E_{\mathrm{R}} Q(q\xi)}{8a_s} \quad \sum_{\mathbf{k},\mathbf{k}'} \quad \left\{ u_x(\mathbf{k}) u_x(\mathbf{k}') \sum_j \cos[2qr_{jx}] e^{i(\mathbf{k}+\mathbf{k}')\cdot\mathbf{r}_j} \right.$$
$$\left. + \quad u_y(\mathbf{k}) u_y(\mathbf{k}') \sum_j \cos[2qr_{jy}] e^{i(\mathbf{k}+\mathbf{k}')\cdot\mathbf{r}_j} \right\}, \tag{3.44}$$

with the positions of vortices in the hexagonal lattice given by

$$\mathbf{r}_i = a_v \sqrt{\frac{2}{\sqrt{3}}} \left[(i_x + \frac{1}{2} i_y)\hat{x} + \frac{1}{2}\sqrt{3} i_y \hat{y} \right]. \tag{3.45}$$

Summing over these lattice coordinates in equation (3.44) gives zero. This is in contradiction with the fact, that on symmetry grounds we expect a finite gap for the collective modes. To overcome this problem we must take into account that the real unpinned vortex ground state in a weak periodic pinning potential is a slightly distorted hexagonal lattice [80]. This comes about because the periodic potential exerts a small net force on the vortices arranged in the hexagonal lattice. The small distortion of the vortex positions is a modulation around the equilibrium of the hexagonal lattice $\mathbf{r}_i \mapsto \mathbf{r}_i + \mathbf{R}(\mathbf{r}_i)$. Following Pogosov *et al.* [80] we find for a square two-dimensional periodic potential

$$R_\alpha(\mathbf{r}_i) = \frac{s E_{\mathrm{R}}}{2q\mu_H A} \frac{d_z}{8a_s} Q(q\xi) \sin[2qr_{i\alpha}]. \tag{3.46}$$

The modulation of the vortex coordinates around the positions of the regular hexagonal lattice involves a factor $\eta = \frac{s E_{\mathrm{R}}}{\mu_H A}$. To keep the displacements small, the condition $\eta \ll 1$ must be satisfied.

Summing over the displaced hexagonal vortex lattice in equation (3.44) indeed leads to a non-zero energy gap. Numerical evaluation of equation (3.44) on a large lattice gives a contribution to the dynamical matrix which is roughly linear in η,

$$D^{\mathrm{OL}}_{\alpha\beta} \approx 0.5\eta \; s E_{\mathrm{R}} \left[\frac{q d_z Q(q\xi)}{4a_s} \right]^2 \delta_{\alpha\beta}, \qquad \eta \ll 1. \tag{3.47}$$

Including this in the calculation of the collective modes, we find

$$\hbar\omega_{\mathbf{k}} = \quad \frac{1}{4\pi n d_z} \left[0.5\eta \; s E_{\mathrm{R}} \left(\frac{q d_z Q(q\xi)}{4a_s} \right)^2 + \mu_H k^2 \right]^{\frac{1}{2}} \times$$
$$\left[\frac{8\pi^2 \hbar^2 d_z n}{a_v^2 M} + 0.5\eta \; s E_{\mathrm{R}} \left(\frac{q d_z Q(q\xi)}{4a_s} \right)^2 + (K_H + \mu_H) k^2 \right]^{\frac{1}{2}}. \tag{3.48}$$

The gap takes the form

$$\hbar\omega_{\mathbf{0}} \approx \frac{0.5\eta\ sE_{\mathrm{R}}}{4\pi n d_z}\left[\frac{qd_zQ(q\xi)}{4a_s}\right]^2 . \tag{3.49}$$

3.5.2 Half-pinned vortex lattice

In the case of the half-pinned vortex lattice, which is always triangular, the dynamical matrix that follows from elasticity theory is given by [95]

$$D^{\mathrm{EL}}_{\alpha\beta}(\mathbf{k}) = K_T k_\alpha k_\beta + \mu_T\delta_{\alpha\beta}k^2 + \kappa_T(1-\delta_{\alpha\beta})k_\alpha k_\beta + \delta\mu_T\tau^z_{\alpha\beta}k_\alpha k_\beta\ , \tag{3.50}$$

where K_T is the bulk modulus of the triangular vortex lattice, and κ_T and μ_T denote the Lamé constants. For a square lattice we have that the parameter $\delta\mu_T$ is equal to zero, as we will see below. In the above expression $\tau^z_{\alpha\beta}$ denotes the Pauli matrix.

To find the contribution due to the optical lattice, we consider specifically the half-pinned case at filling $\nu = \frac{1}{5}$, as shown in figure 3.3. We parametrize the equilibrium position of the vortices as

$$\mathbf{r}_i = \frac{5}{2}i_x a\hat{x} + 2\left[\frac{1-(-1)^{i_x}}{4}\right]a\hat{y} + 2i_y a\hat{y}\ . \tag{3.51}$$

With the use of this parametrization we find that the energy of the vortex lattice due to the pinning of the optical lattice is, for small displacements $\mathbf{u}(\mathbf{r}_i)$ from the equilibrium positions, given by

$$\begin{aligned} E^{\mathrm{OL}}[\mathbf{u}] &= \frac{d_z sE_{\mathrm{R}}Q(q\xi)}{8a_s}\sum_i\left\{\cos\left[2q(r_{ix}+u_x(\mathbf{r}_i))+\pi\right]+\cos\left[2q(r_{iy}+u_y(\mathbf{r}_i))+\pi\right]\right\} \\ &\simeq \frac{d_z sE_{\mathrm{R}}q^2Q(q\xi)}{4a_s}\left[\sum_i(-1)^{i_x+1}u_x^2(\mathbf{r}_i)+u_y^2(\mathbf{r}_i)\right]\ , \end{aligned} \tag{3.52}$$

where we have omitted an irrelevant constant. Note that we have translated the optical lattice potential to ensure that there is a vortex at the origin, consistent with the parametrization in equation (3.51). Using that

$$\sum_i e^{i\mathbf{k}\cdot\mathbf{r}_i} = N_xN_y\delta_{\mathbf{k},\mathbf{0}}\ , \tag{3.53}$$

we find after a Fourier transform in first instance that

$$E^{\mathrm{OL}}[\mathbf{u}] = \frac{d_z sE_{\mathrm{R}}q^2Q(q\xi)}{4a_s}\sum_{\mathbf{k}}\left[\sum_i\sum_{\mathbf{k}'}(-1)^{i_x}e^{i(\mathbf{k}+\mathbf{k}')\cdot\mathbf{r}_i}u_x(\mathbf{k})u_x(\mathbf{k}')+u_y(\mathbf{k})u_y(-\mathbf{k})\right] . \tag{3.54}$$

The sum i_x in the second term of this equation is evaluated by splitting it into a sum over i_x even and i_x odd. If we denote $\mathbf{k}+\mathbf{k}' = (2\pi n_x/L_x, 2\pi n_y/L_y)$, we have that

$$\begin{aligned}
\sum_i (-1)^{i_x+1} e^{i(\mathbf{k}+\mathbf{k}')\cdot\mathbf{r}_i} &= -\sum_{i_x,i_y} (-1)^{i_x} e^{2\pi i n_x i_x/N_x + 2\pi i n_y/N_y \left\{\left[\frac{1-(-1)^{i_x}}{4}+i_y\right]\right\}} \\
&= -N_y\delta_{n_y,0}\left[\sum_p e^{2\pi i n_x(2p)/N_x} - \sum_l e^{2\pi i n_x(2p+1)/N_x - \pi i n_y/N_y}\right] \\
&= -N_x\delta_{n_x,0}N_y\delta_{n_y,0}\left[\frac{1}{2} - \frac{1}{2}e^{2\pi i n_x/N_x - \pi i n_y/N_y}\right]. \qquad (3.55)
\end{aligned}$$

With the use of this result we have that

$$E^{\mathrm{OL}}[\mathbf{u}] = \frac{d_z s E_{\mathrm{R}} q^2 Q(q\xi)}{4a_s}\sum_{\mathbf{k}} u_y(\mathbf{k})u_y(-\mathbf{k}) \equiv \frac{1}{2}\sum_{\mathbf{k}} D^{\mathrm{OL}}_{\alpha\beta}(\mathbf{k})u_\alpha(\mathbf{k})u_\beta(-\mathbf{k}) \ , \quad (3.56)$$

so that the contribution to the dynamical matrix due to the optical lattice is given by[4]

$$D^{\mathrm{OL}}_{\alpha\beta}(\mathbf{k}) = \frac{d_z s E_{\mathrm{R}} q^2 Q(q\xi)}{2a_s}\delta_{\alpha,y}\delta_{\alpha\beta} \ . \qquad (3.57)$$

With the above results, we find that the collective mode dispersion is given by

$$\begin{aligned}
(4\pi n d_z \hbar\omega_{\mathbf{k}})^2 &= \mu_T^2 k^4 + \mu_T^2 k^2\left(K_T k^2 + \frac{8\pi^2\hbar^2 d_z n}{a_v^2 M}\right) \\
&- \kappa_T\left[\frac{16\pi^2\hbar^2 d_z n}{a_v^2 M} + (2K_T+\kappa_T)k^2\right]\frac{k_x^2 k_y^2}{k^2} \\
&- \frac{1}{4}\delta\mu_T^2 k_x^2 k_y^2 + \mu_T\delta\mu_T k^2(k_x^2 - k_y^2) \\
&+ \frac{d_z s E_{\mathrm{R}} q^2 Q(q\xi)}{2a_s}\left[k_x^2\left(K_T + \mu_T - \frac{\delta\mu_T}{2} + \frac{8\pi^2\hbar^2 d_z n}{a_v^2 M k^2}\right) + \mu_T k_y^2\right] . \qquad (3.58)
\end{aligned}$$

Interestingly, this dispersion is gapless, i.e., $\hbar\omega_{\mathbf{0}} = 0$. The eigenvector corresponding to this eigenfrequency is given by $(1,0)$, and so the displacement of the vortices is along the x-axis. Physically, this is understood because it does not cost any energy to uniformly displace all the vortices in the x-direction when the vortices are forming a half-pinned lattice with the geometry shown in figure 3.3. This comes about because under a uniform translation of the vortices in the x-direction, half of the vortices move away from an energy minimum and therefore increase their energy, the other half moves downhill from an energy saddle-point, precisely compensating this increase.

[4]Note that if we rotate the vortex lattice over an angle $\pi/4$, we we would find the the dynamical matrix is proportional to $\delta_{\alpha,x}$ instead of $\delta_{\alpha,y}$.

3.5.3 Fully-pinned vortex lattice

The structure of the fully-pinned vortex lattice at certain filling is triangular, in general. Therefore, the contribution to the dynamical matrix due to the elasticity of the vortex lattice takes the form of equation (3.50) with elastic constants $K_P,\ \mu_P\ ,\kappa_P$ and $\delta\mu_P$. In the special cases for which the fully-pinned vortex lattice has a square structure, we have that $\delta\mu_P = 0$. Since all the vortices are positioned at the minimum of the pinning potential, the contribution of the optical lattice to the dynamical matrix is constant and diagonal, and given by

$$D^{\mathrm{OL}}_{\alpha\beta}(\mathbf{k}) = \frac{d_z s E_{\mathrm{R}} q^2 Q(q\xi)}{2a_s}\delta_{\alpha\beta}\ . \tag{3.59}$$

Hence, we find for the phonon dispersion

$$\begin{aligned}(4\pi n d_z \hbar\omega_{\mathbf{k}})^2 \quad = \quad & \left(\mu_P k^2 + \frac{d_z s E_{\mathrm{R}} q^2 Q(q\xi)}{2a_s}\right)^2 \\ & + \left(\mu_P k^2 + \frac{d_z s E_{\mathrm{R}} q^2 Q(q\xi)}{2a_s}\right)\left[K_P k^2 + \frac{8\pi^2\hbar^2 d_z n}{a_v^2 M k^2} + \frac{\delta\mu_P}{2}\left(k_x^2 - k_y^2\right)\right] \\ & + \left[\frac{\delta\mu_P^2}{4} - \kappa_P^2 - 2\kappa_P\left(K_P + \frac{8\pi^2\hbar^2 d_z n}{a_v^2 M k^2}\right)\right] k_x^2 k_y^2\ .\end{aligned} \tag{3.60}$$

At zero momentum we find for the gap[5]

$$\hbar\omega_{\mathbf{0}} = \frac{q^2 s E_{\mathrm{R}} Q(q\xi)}{8 n a_s}\ , \tag{3.61}$$

corresponding to an eigenvector $\propto (1, i)$. From this eigenvector we therefore conclude that the zero-momentum mode physically corresponds to a precession of the vortices around the maxima of the optical lattice potential, as expected.

3.5.4 The gap

If one tunes the strength of the periodic potential, the vortex lattice changes, depending on the filling ν. The energy gap of the collective modes is different in the three vortex lattice phases. To summarize the results on the gap, we have

$$\hbar\omega_{\mathbf{0}} = \begin{cases} 0.5\ \eta\ \frac{d_z}{8a_s}[q\xi Q(q\xi)]^2 s E_{\mathrm{R}} & \text{hexagonal vortex lattice,} \\ 0 & \text{half-pinned vortex lattice,} \\ (q\xi)^2 Q(q\xi) s E_{\mathrm{R}}/\pi & \text{fully-pinned vortex lattice.} \end{cases} \tag{3.62}$$

It is clear that the gap in the hexagonal phase is much smaller than the gap in the fully-pinned vortex phase. This is because in the hexagonal phase, the non-zero contribution comes entirely from the displacements of the vortices from the equilibrium

[5]Note that in equation (10) of reference [81] there should be an additional factor of 2π.

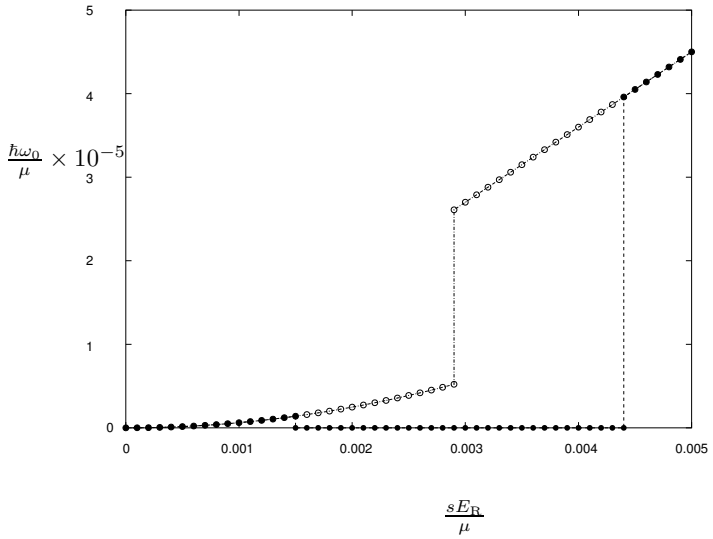

Figure 3.6: The energy gap to the collective modes of a vortex lattice in the presence of a periodic optical potential as function of the lattice strength, for $\nu = \frac{1}{4}$ (open circles) and $\nu = \frac{1}{5}$ (filled circles). We used $\eta = 0.64\left(\frac{sE_{\rm R}}{\mu}\right)$ (*) and $q\xi = .05$.

positions of the hexagonal lattice. The gap is then of second order in $sE_{\rm R}$, since $\eta \propto sE_{\rm R}$.

For the half-pinned and fully-pinned vortex lattices, there is no second order contribution to the gap. This is because in these phases the vortices are located on minima and saddle points of the pinning potential. The fact that the energy gap in the half-pinned phases is zero, relies on the fact that we consider infinite vortex lattices. In a trapped system there will be a gap to collective excitations, that becomes smaller with increasing system size.

In figure 3.6 we display the gap as function of the dimensionless parameter $\frac{sE_{\rm R}}{\mu}$ for the cases $\nu = \frac{1}{4}$ and $\nu = \frac{1}{5}$ which we have considered in this chapter. We used the estimate[6] $\eta = .64\left[\frac{sE_{\rm R}}{\mu}\right]$. It is clearly seen that the gap has a discontinuity if $\frac{sE_{\rm R}}{\mu}$ is tuned through a phase boundary. It must be emphasized that in the Abrikosov phase only the qualitative features of the behavior of the gap can be deduced from figure 3.6. This is because the gap then depends on the shear modulus μ_H which is a

[6]We obtained this estimate using the expression for the shear modulus following from hydrodynamic theory. We have $e_{\rm shear} = \mu_H A = \mu_H^{\rm 3D} d_z A = \frac{n\hbar\Omega}{8} d_z \pi \ell^2$, with $\ell^2 = \frac{\hbar}{M\Omega}$. The ratio between the chemical potential $\mu = gn$ and $e_{\rm shear}$ is constant, $\frac{e_{\rm shear}}{\mu} = \frac{d_z}{32 a_s}$. We then use $a_s \approx 5$ nm for ^{87}Rb and $d_z \approx 10\ \mu$m to find $\eta = \frac{sE_{\rm R}}{e_{\rm shear}} = 0.64\left[\frac{sE_{\rm R}}{\mu}\right]$.

phenomenological constant in our calculations.

Finally, we would like to comment on the experimental implications of the collective mode spectra we have calculated. Although our calculations contain phenomenological parameters, there are nonetheless some qualitative predictions that could be tested experimentally. First of all, for the half-pinned and fully-pinned vortex lattices the collective mode spectrum is anisotropic, i.e., the frequency of the collective modes depends on the direction of propagation. By performing the same experiment as Coddington *et al.* [27], in which the collective modes are excited by a perturbation at the center of the condensate, one could probe this anisotropy. Another prediction of our theory is that the collective modes are in general gapped in the presence of the vortex lattice. An exception is the triangular half-pinned vortex lattice, which has a gapless mode, corresponding to the translation of the vortices in one direction. (For the illustration in figure 3.3 this direction is the x-direction.) For the propagation of the modes in the other direction there will be a gap. This strong anisotropy should be experimentally observable by the above-mentioned experiment. The excitations of the fully-pinned vortex lattice are also gapped. As mentioned before, the zero-momentum mode corresponds in this case to a simultaneous in-phase precession of all the vortices around the maxima of the optical potential. This mode could be excited by slightly displacing the optical lattice. Because this zero-momentum mode of the vortex lattice does not have shear or compression, it does not depend on the elasticity constants, which are phenomenological in our calculation. Hence equation (3.62) should give an accurate prediction for the gap in this case, which is directly experimentally verifiable.

3.6 Discussion

Since we have considered the ground state of vortices, we have implicitly assumed that the optical lattice is co-rotating with the Bose-Einstein condensate. Although this is very difficult to achieve experimentally, it has, however, recently been proposed to create effective magnetic fields, and therefore effective rotation, by optical methods [99, 100]. We believe that the calculations presented here are relevant for such a situation.

There are several interesting directions for further investigation of the influence of a periodic potential on the physics of rotating Bose-Einstein condensates. For instance, it would be interesting to consider more strongly-correlated regimes that occur at fast rotation, and to study the effects of the periodic optical potential on the melting of the vortex lattice [42]. One would expect that in this regime the effect of quantum fluctuations, i.e., quantum tunnelling of the vortices through the potential barriers of the pinning potential, becomes important. Aspects of this were studied by Sørensen *et al.* [101], who showed that for ultra low particle and vortex density the ground state of rotating bosons (with $\frac{N}{N_v} = \frac{1}{2}$) in a periodic potential is given by the Laughlin liquid. It would be challenging to investigate the system with high particle and vortex density and a large number of vortices per boson.

Yet another interesting possibility for future work is to study a rotating spin-full condensate in the presence of a periodic potential. Rotating spin-full condensates are expected to form spin-textures (skyrmions) [102] and regular lattices thereof [61, 8], analogous to the formation of vortices in a single component condensate. The pinning effects in each spin component of the condensate caused by the periodic potential will further enrich the phase diagram in these systems.

Chapter 4

Rotating spin-1 condensates: exact states

We[1] *provide results on the phase diagram for rotating spin-1 bosons in the lowest Landau level (LLL). Employing the* $SU(3)$ *symmetry, we discuss how in a slowly-rotating system without spin-spin interactions (*$c_2 = 0$*) the exact quantum ground state evolves from the non-rotating one towards the so-called boson triplet condensate [7] (BTC) at angular momentum* $L = N$*, which is the spin-1 analogue of the vortex in scalar condensates. Furthermore we compute the ground state angular momentum* $L(\omega)$ *as a function of the rotation frequency* ω *in a disk and spherical geometry.*

Including spin in a rotating Bose-Einstein condensate significantly enriches the phase diagram. In a scalar condensate, slow rotation results in the sudden appearance of a quantized vortex. This sequence changes when spin is present. Here we start our analysis of a slowly rotating spin-1 condensate without any spin-dependent interactions. The results clearly emphasize the role of spin.

This chapter is organized as follows. In section 4.1 we define the model by discussing LLL truncation in a disc, sphere or torus geometry, specifying the interaction Hamiltonian, and make remarks on the general symmetry properties for later use. In section 4.2, we study the phase diagram by direct numerical diagonalization. In section 4.3 exact quantum ground state wave functions and energies for a slowly rotating (angular momentum $L \leq N$) system in the $c_2 = 0$ limit are presented. We conclude this chapter with a short discussion of large degeneracies in the ground state at $c_2/c_0 = -1$ in section 4.4.

[1] This chapter is based on a collaboration with F. J. M. van Lankvelt, K. Schoutens and N. Read, see [7, 8].

4.1 Lowest Landau level model Hamiltonian and its symmetry

In this section we describe the truncation of the space of single-particle states to those in the LLL, and then explain the use of different geometries (sphere, torus) once this truncation has been made. Then we give the form of the interaction Hamiltonian that will be assumed, and some analysis of the symmetries of the model, with particular reference to certain limits and different geometries.

4.1.1 Truncation to the lowest Landau level

In a rotating frame of reference the Hamiltonian for N trapped, weakly-interacting spin-1 bosons is

$$H = \sum_i^N \left[\frac{\omega_0}{2}(-\vec{\nabla}_i^2 + r_i^2) - \vec{\omega}\cdot\vec{L}_i\right] + H_{\rm int}. \tag{4.1}$$

Here $\vec{\omega}$ is the frequency of the rotation drive, $\vec{L}_i$ the angular momentum of the i-th particle and $H_{\rm int}$ the interaction Hamiltonian, which we discuss below. We have set $\hbar$ and the harmonic oscillator length $l \equiv (\hbar/m_b\omega_0)^{1/2}$ of the trap (with ω_0 the trap frequency and m_b the boson mass) equal to one. Modes in the direction of the rotation axis are frozen out, leaving us effectively with a two-dimensional system. The energy eigenvalues of the single-particle part of the Hamiltonian are then $E_{n,m} = (2n+m+1)\omega_0 - m\omega$, with $n \geq 0$ the Landau level index and $m \geq -n$ the z-component of angular momentum, labeling the states within each Landau level, see figure 4.1.

We consider the model in which the single-particle states are restricted to the lowest ($n = 0$) Landau level (LLL) [45]. This is valid when the interactions are sufficiently weak, as we will explain momentarily. The normalized LLL wave functions are $\phi_m(z)\,\zeta^\alpha$ with the orbital part $\phi_m(z) \propto z^m e^{-|z|^2/2}$ ($z = x + iy$), and ζ^α a three-component complex vector representing the spin state; here α labels the eigenstates of the z-component of the spin S_z for each particle, $\alpha = \uparrow, 0, \downarrow$. [Later, in chapter 5 it will be convenient also to use the basis of Cartesian components for spin 1, labeled by $\mu = x, y, z$.] When we use second quantization, we will denote the boson creation and annihilation operators for these single-particle states by $b^\dagger_{m\alpha}$, $b_{m\alpha}$, and the corresponding occupation numbers by $n_{m\alpha} \equiv b^\dagger_{m\alpha} b_{m\alpha}$. Also, we sometimes use the field operator $\psi_\alpha(z) = \sum_m b_{m\alpha}\phi_m(z)$. The single particle contributions to the Hamiltonian add up to $(\omega_0 - \omega)L$, with $L = \sum_i L_{zi}$ the z-component of total angular momentum. We will refer to this geometry as the disc in view of the form of the fluid states (for repulsive interactions) which tend to form a disc or "pancake", because of the centrifugal force. Note that we must have $\omega \leq \omega_0$, otherwise the system becomes unstable.

To study the bulk properties of the quantum ground states, we will eliminate boundary effects by using instead two other geometries and taking the limit $\omega \to \omega_0$. In a spherical geometry [105], the orbital part of the LLL single-particle wavefunctions is

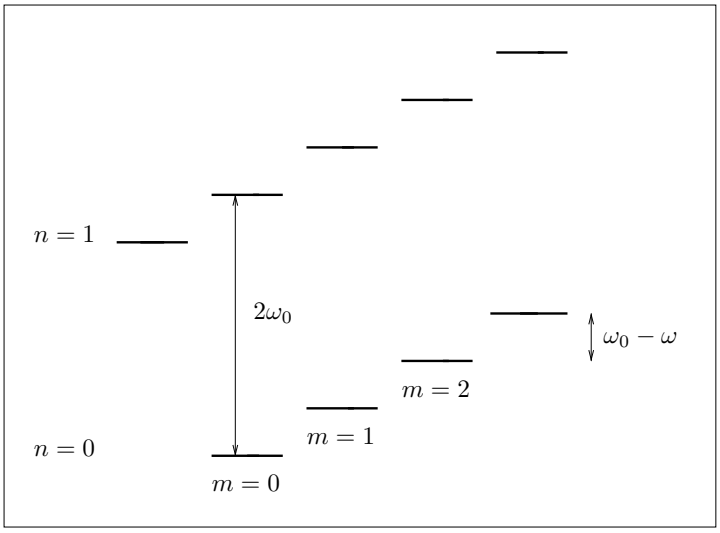

Figure 4.1: Structure of the single boson energy spectrum in the rotating harmonically trapped system.

$\phi_m(z) \propto z^m/(1+(\frac{|z|}{2R})^2)^{1+N_v/2}$, where z represents position on the sphere by stereographic projection to the plane, and R is the radius of the sphere. The number of orbitals is restricted by the vorticity N_v penetrating the sphere, $0 \leq m \leq N_v$. The $N_v + 1$ single-particle orbitals form a representation of orbital angular momentum equal to $N_v/2$, see reference [105]. In the limit $R \to \infty$, keeping N_v/R^2, N and z constant, the single-particle wave functions on the sphere reduce to those for the disc as above. The total angular momentum on the sphere is characterized by quantum numbers $\tilde{L}$ for the magnitude, and $\tilde{L}_z$ for the z-component. In terms of L which has eigenvalues $L = \sum_i m_i$ as before, $\tilde{L}_z = \frac{1}{2}NN_v - L$. We emphasize that our definition of L when used for the sphere does not have its usual meaning, but is related to the z-component in such a way that the $N_v \to \infty$ limit agrees with the plane.

The final geometry we use is the torus. Here the single-particle wave functions take the form $\phi(z) \propto f(z)e^{-y^2}$ in the Landau gauge, with f a quasi-periodic holomorphic function. With N_v flux quanta, f has N_v zeros in the unit cell. There are exactly N_v independent solutions, of the form $f(z) = \prod_{i=1}^{N_v} \vartheta_1(z - z_i|\tau)$, with τ describing the geometry of the unit cell and z_i the zeros of f. The use of ϑ-functions ensures that ϕ is periodic. Many-body states can be classified by their Haldane momentum [106].

4.1.2 Interaction Hamiltonian

In a model description, the Hamiltonian describing the 2-body interactions of a system of N spin-1 bosons is a contact interaction, and contains spin-independent (H_n) and spin-dependent (H_s) terms, of strengths c_0, c_2 respectively

$$\begin{aligned} H_{\rm int} &= H_n + H_s \\ &= 2\pi \sum_{i<j}^{N} \delta^{(2)}(\mathbf{r}_i - \mathbf{r}_j) \left[c_0 + c_2 \, \vec{S}_i \cdot \vec{S}_j \right]. \end{aligned} \tag{4.2}$$

Here $c_0 = (g_0 + 2g_2)/3$, $c_2 = (g_2 - g_0)/3$, $g_S = 4\pi\hbar^2 a_S/m_b$ and a_S ($S = 0, 2$) the 2D s-wave scattering phase shift in the spin-S channel [107, 23]. A factor 2π has been extracted for later convenience. One can obtain these parameters by integrating over the third direction. Assuming, for example, harmonic confinement with quantum length $l_\perp$ in the z-direction, one finds $a_S^{2D} = a_S^{3D}/\sqrt{2\pi} l_\perp$ when $l_\perp \ll l$. For the sphere, the coordinates $\mathbf{r}$ in this Hamiltonian take values on the surface of the sphere, with radius R.

The use of the LLL reduced Hamiltonian is justified when the interactions are weak. Physical quantities evaluated in the full model differ from those in the LLL model by relatively small corrections when the $\nu c_S \ll 2\omega_0$. Here ν is the typical filling factor (expectation of the occupation numbers, summed over α or μ) of the single-particle states. Notice that this condition becomes much less stringent as $\omega \to \omega_0$ in the repulsive regime, as then the particles spread out into a pancake, and the filling factor ν becomes of order 1.

Finally then, the LLL Hamiltonian in the rotating frame which we wish to analyze is

$$H_\omega = (\omega_0 - \omega) L + H_{\rm int} \, . \tag{4.3}$$

Note that we use precisely this definition in the case of the sphere as well as for the disc. It will be useful also to know the ground states of $H_{\rm int}$ for each L.

Second quantized form of the interaction hamiltonian

In this work we extensively make use of the hamiltonian expressed in second quantized language, and it may be instructive to discuss it shortly. Making use of the definition $\langle z | b^\dagger_{m,\alpha} | 0 \rangle = \phi_m(z) \zeta^\alpha$, the second quantized form of equation (4.2) is easily calculated. The spin-independent term of the hamiltonian on the sphere takes the form

$$H_n = c_0 \sum_{\alpha\beta} \sum_{m_1 \cdots m_4} V_{m_1 m_2 m_3 m_4} b^\dagger_{m_1 \alpha} b^\dagger_{m_2 \beta} b_{m_3 \alpha} b_{m_4 \beta},$$

with the matrix elements depending on the spatial orbitals

$$V_{m_1\cdots m_4} = \frac{1}{2}\frac{\sqrt{\begin{pmatrix} N_v \\ m_1 \end{pmatrix}\begin{pmatrix} N_v \\ m_2 \end{pmatrix}\begin{pmatrix} N_v \\ m_3 \end{pmatrix}\begin{pmatrix} N_v \\ m_4 \end{pmatrix}}}{\begin{pmatrix} 2N_v \\ m_3+m_4 \end{pmatrix}}\delta^{m_1+m_2}_{m_3+m_4}. \tag{4.4}$$

This form clearly demonstrates that angular momentum and the spin quantum numbers are conserved by the interactions. In the limit $N_v \to \infty$, where the spherical geometry effectively becomes that of a plane, these matrix elements reduce to

$$V_{m_1\cdots m_4} \to \delta^{m_1+m_2}_{m_3+m_4}\frac{(m_3+m_4)!}{2^{m_3+m_4+1}\sqrt{m_1!m_2!m_3!m_4!}}. \tag{4.5}$$

For the spin-dependent term of the interaction, the matrix elements consist of $V_{m_1\cdots m_4}$ multiplied by matrix elements of $\vec{S}_i \cdot \vec{S}_j$, which depend on the $\alpha_1, \ldots, \alpha_4$ labels of the bosons. These matrix elements can be found in standard quantum-mechanics texts,

$$\begin{aligned} H_s \;=\; & c_2 \sum_{m_1\cdots m_4} V_{m_1\cdots m_4}\Big[b^\dagger_{m_1\uparrow}b^\dagger_{m_2\uparrow}b_{m_3\uparrow}b_{m_4\uparrow} + b^\dagger_{m_1\downarrow}b^\dagger_{m_2\downarrow}b_{m_3\downarrow}b_{m_4\downarrow} \\ & -2b^\dagger_{m_1\uparrow}b^\dagger_{m_2\downarrow}b_{m_3\uparrow}b_{m_4\downarrow} + 2b^\dagger_{m_10}b^\dagger_{m_2\uparrow}b_{m_30}b_{m_4\uparrow} + 2b^\dagger_{m_10}b^\dagger_{m_2\downarrow}b_{m_30}b_{m_4\downarrow} \\ & +2b^\dagger_{m_10}b^\dagger_{m_20}b_{m_3\uparrow}b_{m_4\downarrow} + 2b^\dagger_{m_1\downarrow}b^\dagger_{m_2\uparrow}b_{m_30}b_{m_40}\Big]. \end{aligned} \tag{4.6}$$

This part of the interaction does not violate conservation of spin. However, because of the presence of the last two terms in equation (4.6), the particle number in a spin component of the condensate is not conserved (for $c_2 \neq 0$). This leads to interesting spin-dynamics [21, 22].

4.1.3 $SU(3)$ symmetry analysis for $c_2 = 0$

In general, the only symmetry in spin space of the Hamiltonians $H_{\rm int}$ and H_ω is spin-rotation symmetry $SO(3)_{\rm spin}$. This implies that spin states will come in multiplets of spin S with degeneracy $2S+1$ (with S integer since the particles have spin 1). However, at $c_2 = 0$, the interaction Hamiltonian reduces to the spin-independent interaction H_n. In this case the spin-rotation symmetry is enlarged from $SO(3)_{\rm spin}$ to $SU(3)_{\rm spin}$. It will be useful to understand what this implies about the spin multiplets in a finite size system. For $c_2 = 0$, the spectrum will contain degenerate spin multiplets labelled by $SU(3)$-quantum numbers (p, q). These tuples are the Dynkin indices labelling irreducible representations of dimension $\dim_{(p,q)} = \frac{1}{2}(p+1)(q+1)(p+q+2)$. Since $SO(3)$ is embedded in $SU(3)$, each multiplet can be decomposed into a set of $SO(3)$ multiplets. These $SO(3)$ spin quantum numbers can be deduced by using branching rules for $SU(3) \mapsto SO(3)$. The fundamental branching rule states that a

$(p,0)$ or $(0,p)$ multiplet contains $S = p,\, p-2,\, p-4,\, \ldots,\, 1\ (0)$ for p odd (resp., even). Using the fusion rule

$$(p,0) \otimes (0,q) = (p,q) \oplus (p-1,q-1) \oplus \cdots \oplus (p-q,0)\ , \tag{4.7}$$

which is valid for $p \geq q$, general branching rules can be derived. A multiplet (p,q) with q odd and $p \geq q$ decomposes in $SO(3)$ multiplets with highest weights S according to the branching rule

$$(p,q) \mapsto \bigoplus_{i=0}^{\frac{q-1}{2}} \bigoplus_{S=2i+1}^{p+q-2i} S \quad . \tag{4.8}$$

For q even we find

$$(p,q) \mapsto \left(\bigoplus_{i=0}^{\frac{q-2}{2}} \bigoplus_{S=2i+1}^{p+q-2i} S \right) \oplus \left(\bigoplus_{j=\frac{q+1}{2}}^{\frac{p}{2}} 2j \right), \quad p \text{ odd} \tag{4.9}$$

$$(p,q) \mapsto \left(\bigoplus_{i=0}^{\frac{q-2}{2}} \bigoplus_{S=2i+2}^{p+q-2i} S \right) \oplus \left(\bigoplus_{j=0}^{\frac{p}{2}} 2j \right), \qquad p \text{ even.} \tag{4.10}$$

Note that the highest $SO(3)$-spin in an $SU(3)$-multiplet (p,q) is always $S = p+q$, and the lowest $S = 0$ or 1.

4.1.4 Orbital symmetry in spherical geometry

In the plane geometry, $H_{\rm int}$ is invariant under translations and rotations in the plane. When working on the sphere, this symmetry group is replaced by the rotation group $SO(3)_{\rm orb}$ (strictly, we should say $SU(2)_{\rm orb}$ whenever N_v is odd) of the sphere. In the limit $R \to \infty$ described above, this symmetry becomes translations and rotations of the plane. When taking this limit, we also hold L fixed, and hence many-particle states of definite $SO(3)_{\rm orb}$ quantum numbers $(\tilde{L}, \tilde{L}_z)$ become in the limit infinite-dimensional multiplets of the Euclidean group of the plane. States within each multiplet differ only in the state of the center of mass variable (which has coordinate $z_c = \sum_i z_i/N$). Thus, if ψ_L is an eigenfunction of $H_{\rm int}$ at certain angular momentum L, then there exists a whole "tower" of states $\psi_{L+L'} \propto z_c^{L'} \psi_L$ with the same interaction energy at angular momentum $L + L'$.

We remark that in situations where only a few quantum orbitals are available to the bosons, the spectrum is largely determined by symmetry considerations. Particular examples are the spectrum for $N_v = 2$ on the sphere, where the exact N-body energies are given in terms of Casimir invariants of the orbital and spin-symmetries (see equation (4.13) below), and the case with $N_v = 4$ on the torus, where the topological degeneracy pertaining to particular quantum liquid states is recovered from the $SU(3)$ spin-symmetry [8].

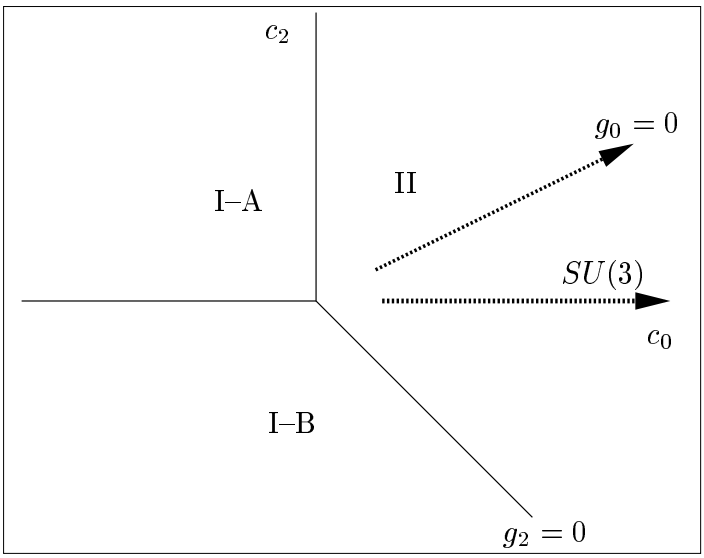

Figure 4.2: Overview of c_0–c_2 plane, with special regions and directions marked.

4.2 Main features of the phase diagram

In this section we make a first pass through the phase diagram with numerical results on moderate sizes. First we consider the ground states of $H_{\rm int}$ in the disc geometry for each L, then use this to find the ground states of H_ω as a function of ω. All this has to be done for general values of c_0, c_2.

4.2.1 Global structure of the phase diagram

First we point out that the magnitude $(c_0^2 + c_2^2)^{1/2}$ only sets the overall energy scale, so it can be divided out. Thus the phase diagram can be thought of as a circle, in which a point on the circle represents a ray in the c_0–c_2 plane. We wish to examine this for each L, or later for each ω. In figure 4.2 the c_0–c_2 plane is shown with certain special directions ($c_0 = 0$, $c_2 = 0$, $g_0 = 0$, $g_2 = 0$) that will be important later picked out.

For $L = 0$, the ground state has total spin $S = N$ for $c_2 < 0$ (ferro regime) and $S = 0$ (1) for N even (odd) for $c_2 > 0$ (anti-ferro regime). These states are the way that the broken symmetry states described in section 2.1.2 (the ferromagnetic and polar states respectively) appear in a finite size study. For $c_2 = 0$, there is a single $SU(3)$ multiplet of spin states, decomposing into one $SO(3)$ multiplet of each spin $S = N, N-2, \ldots$ The transition at $c_2 = 0$ can thus be viewed as levels crossing, with

a larger degeneracy on the line $c_2 = 0$. As L increases, these two phases at $c_2 \neq 0$ survive in part of the phase diagram, as compact drops of fluid, with the center of mass carrying all the angular momentum. Meanwhile, the positive c_0 axis gradually opens into a region that contains other phases. By the time L is $\geq N$, the c_0–c_2 plane contains the three regions labelled I–A, I–B, and II in figure 4.2.

The ground states in regions I–A and I–B are similar to the one in the "attractive" regime in the scalar case [43]. The orbital part of the ground state wavefunction is of the form $\tilde{\Psi}(z_i) \propto z_c^L$. In region I–A ($c_0 < 0$, $c_2 > 0$), the spin state is the same spin-singlet as for the $L = 0$ ground state, and the energy [108] becomes $[c_0 N(N - 1)/2 - N c_2]$. In region I–B ($c_2 < 0$, $c_0 < -c_2$), the spin state is ferro, $S = N$, giving energy [43] $(c_0 + c_2)N(N-1)/2 < 0$. At $c_2 = 0$, $c_0 < 0$, the spin states again form the $SU(3)$ multiplet. In the remaining "repulsive" region II, the ground state is in general not a common eigenstate of the c_0 and c_2 parts of the interaction, and the ground state energy depends non-linearly on the ratio $\gamma = c_2/c_0$. Note that we have now located the repulsive region more precisely than in our previous characterization of it simply as $c_0 > 0$. Most of the following analysis focuses on region II only, which can be parametrized by $\gamma = c_2/c_0$ alone.

4.2.2 Finite size results in region II as a function of ω

In figure 4.4 we show the ground state quantum numbers (L, S) in region II for $N = 6$ bosons as a function of the rotation frequency ω. As the phase diagram for each ω is a circle (which in region II can be parametrized by $\gamma = c_2/c_0$, or by $\phi = \arctan\gamma$), we are free to plot ω radially. The parameters are shown in units of ω_0 and with $c_0 = 0.25$, but notice that the ground state quantum numbers can only depend on the dimensionless ratios of energies $(\omega_0 - \omega)/c_0$ and c_2/c_0, so that the structure shown is actually present (though with the radial variable rescaled and shifted) for all parameter values (unless c_0 is too large). The dashed rays are the lines $c_2 = -c_0$, $c_2 = 0$ and $c_2 = c_0/2$, and the outer dashed circle is the locus of $\omega = \omega_0$. The ground state angular momentum L and spins S at $c_2 = 0$ and as a function of ω, are shown in the inset. The degenerate spin values at $L \leq N$ are seen to correspond to the following irreducible $SU(3)$ multiplets: $(p, q) = (6, 0)$ for $L = 0$, $(p, q) = (4, 1)$ for $L = 1$, $(p, q) = (2, 2)$ for $L = 2$, $(p, q) = (0, 3)$ for $L = 3$ and $(p, q) = (0, 0)$ for $L = 6$. Note also that for $c_2 < 0$, $c_0 > -c_2$ the ground state spin gradually decreases from $S = 6$ at $\omega = 0$ to $S = 0$.

4.3 Slow rotation: exact ground states at $c_2 = 0$, $L \leq N$

For larger sizes, a brute-force numerical approach is not feasible, so we develop other approaches. In this section we determine the exact ground state energies and wavefunctions for slow rotation (angular momentum up to the boson number, $L \leq N$), for $c_0 > 0$ and $c_2 = 0$, exploiting the $SU(3)$ symmetry described in the section 4.1. Some of the ground states we find were described in reference [50]. We analyze a system

of N spin-1 bosons in spherical geometry with N_v quanta of vorticity, with the disc geometry emerging as the limit $N_v \to \infty$. We remark that for N sufficiently large, it becomes natural to discuss low energy properties in terms of mean field configurations that break the various symmetries and whose energy is slightly higher than that of the exact quantum ground state; this will be discussed in section 5.1.

4.3.1 Exact eigenstates of H_n

The ground state spectrum for $c_2 = 0$ and $L \leq N$ can be understood by exploiting the $SU(3)$ symmetry of the Hamiltonian H_n. In our analysis we proceed as follows. We consider two series of eigenstates of H_n, in which (roughly speaking) the bosons occupy at most the lowest three orbitals. Among these eigenstates, we identify the exact quantum ground states on the disc and the sphere, as a function of the angular momentum. This then allows us to compute the ω dependence of the ground state angular momentum for general N at $c_2 = 0$.

We write the first series of eigenstates as $|p, q, n\rangle^I$. These states contain doublets and triplets of spin-1 bosons that are fully antisymmetric in spin indices, and in the orbital indices (guaranteeing the overall symmetry that is required). The different numbers of single bosons, doublets and triplets correspond uniquely to the values of N and the quantum numbers (p, q) of the corresponding $SU(3)$ multiplets. The triplets, which appear n times, are singlets under $SU(3)$, and so do not affect the overall $SU(3)$ representation. The highest spin component ($S^z = p+q$) of the corresponding $SU(3)$ multiplet takes the following form (up to normalization)

$$|p, q, n\rangle^I \propto [\vec{e}_1 \cdot \vec{B}^\dagger_\uparrow]^p [\vec{e}_2 \cdot (\vec{B}^\dagger_\uparrow \times \vec{B}^\dagger_0)]^q [\vec{B}^\dagger_0 \cdot (\vec{B}^\dagger_\uparrow \times \vec{B}^\dagger_\downarrow)]^n |0\rangle, \tag{4.11}$$

with $\vec{e}_1 = (1, 0, 0)$, $\vec{e}_2 = (0, 0, 1)$ and $\vec{B}^\dagger_\alpha = (b^\dagger_{0,\alpha}, b^\dagger_{1,\alpha}, b^\dagger_{2,\alpha})$. Clearly, the total number of bosons is $N = p + 2q + 3n$. The energies corresponding to equation (4.11) are

$$\begin{aligned} E^I_{p,q,n}/c_0 &= \alpha_1^{N_v} n(n-1) + \alpha_2^{N_v} q(q-1) + \frac{1}{2}p(p-1) \\ &\quad + \alpha_3^{N_v} np + \frac{3}{2}qp + \alpha_4^{N_v} nq, \end{aligned} \tag{4.12}$$

with

$$\alpha_1^{N_v} = 3\tfrac{11N_v^2 - 20N_v + 6}{4(2N_v-3)(2N_v-1)} \quad \alpha_2^{N_v} = \tfrac{5N_v-2}{2(2N_v-1)}$$
$$\alpha_3^{N_v} = \tfrac{7N_v-4}{2(2N_v-1)} \qquad \alpha_4^{N_v} = \tfrac{5\alpha_2^{N_v}}{2}.$$

This energy is for spherical geometry, and it depends on the number N_v of flux quanta. In appendix A we give more details on how to calculate eigen values and expectation values of the state in equation (4.11). For $N_v \to \infty$ equation (4.12) gives the energy in a disc geometry; $N_v = 2$ gives the energy on a sphere with 3 orbitals. On the basis of exact diagonalization studies for $N = 6, 9, 12, 15, 18$ particles we claim that on the

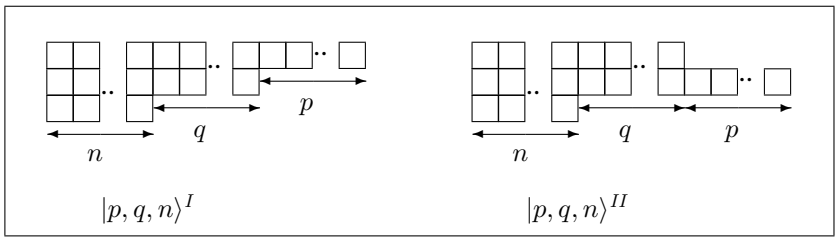

Figure 4.3: The structure of the two different series of eigenstates of H_n, displayed in a form similar to Young tableaux. In both cases, the corresponding $SU(3)$-representation has Dynkin labels (p, q).

disc for $L \leq N/2$, the ground state multiplet is precisely $|p, q, 0\rangle^I$, with $p = N - 2L$, $q = L$.

On the sphere with $N_v = 2$, we have obtained a much stronger result [109], namely a closed form result for *all* eigenvalues of H_n. It turns out that these energies can be given in terms of the number N of bosons, the total angular momentum $\tilde{L}$ and the (p, q) labels of the $SU(3)$ representation, according to

$$E^{N_v=2}_{p,q}/c_0 \quad = \quad \frac{5}{18}N(N-1) + \frac{1}{6}T^2_{p,q} + \frac{1}{6}\tilde{L}(\tilde{L}+1), \tag{4.13}$$

where $T^2_{p,q} = (p^2 + q^2 + pq)/3 + p + q$ is the quadratic Casimir operator for $SU(3)$ in the representation (p, q). Specializing this expression to the states in series I, by eliminating N in favor of n and using the fact that $\tilde{L} = p + q$, reproduces the result in equation (4.12) for $N_v = 2$.

Analyzing the ground state on the disc for $L > N/2$, we identified a second series of states $|p, q, n\rangle^{II}$. One can think of the type II states as having the p single bosons in $m = 1$ rather then $m = 0$, so that now $\vec{e}_1 = (0, 1, 0)$. That is not quite correct for the energy eigenstates, as we will explain below, but it does give the correct quantum numbers. The states in series I, II share the property of having p single bosons and q doublets, leading to $SU(3)$ Dynkin labels (p, q). It may be illuminating to display the structure of the states in terms of diagrams similar to Young tableaux as in figure 4.3. For the orbital structure of the highest-weight states in either series I or II, the lengths of the three rows represent the number of bosons in the orbitals $m = 0$, 1, 2 respectively (in the rough point of view, which will be corrected below), while the differences p, q and n in the lengths correspond to the SU(3) structure. Essentially, these diagrams are ordinary Young tableaux for the states, but with the first two rows exchanged in the case of series II.

For the case of the type II states, the following correction must be made to obtain the energy eigenstates. In the case of scalar bosons, it is known [45, 110, 111] that the ground state configuration at $L = p$ of p bosons is a vortex located at their center of mass, with wavefunction $\prod_i (z_i - z_c)$ with $z_c = \sum_i z_i/p$. This state is not entirely

restricted to the $m = 1$ orbital, as there are components in which other orbitals in the range $0 \leq m \leq p$ are occupied as well. The p bosons in the state $|p, q, n\rangle^{II}$ form such a vortex. This complication makes it difficult to write down the closed form expression for the states in series II; based on numerical analysis for small N and mean field results for large N (see section 5.1), we do propose the following closed form expression for the corresponding energy on the disc

$$\begin{aligned} E^{II}_{p,q,n}/c_0 &= \frac{33}{16}n(n-1) + \frac{5}{4}q(q-1) + \frac{1}{4}p(p-2) \\ &+ \frac{25}{8}nq + \frac{11}{8}np + qp. \end{aligned} \tag{4.14}$$

Note that the p-independent terms in this formula are identical to those for type I states with $N_v = \infty$. The state $|p, 0, 0\rangle^{II}$, has energy $p(p-2)/4$, which is exactly the ground state energy of a rotating scalar Bose-Einstein condensate at $L = p = N$. This justifies the interpretation of the polarized subsystem with p bosons forming a vortex at the center of mass. However, it turns out that $|p, 0, 0\rangle^{II}$ will never be the lowest energy configuration for a rotating spin-1 system.

Among the type I/II states the following are special. First, $|p, 0, 0\rangle^{I}$ is the non-rotating ground state, corresponding to the $(p, 0)$-multiplet. Second, $|0, q, 0\rangle$ gives a wavefunction composed of anti-symmetrized pairs of bosons, a Boson-Doublet-Condensate (BDC) or $(0, q)$-multiplet. Third, $|0, 0, n\rangle$ is composed of 3-body singlets. It is a condensate of triplets or boson-triplet-condensate [7] (BTC); we shall see that it forms the ground state at $L = 3n = N$. In figure 4.5 we plotted the two-dimensional density profiles of the BTC and the nonrotating condensate. The BTC-state can be regarded as a symmetrized version of the core-less vortices observed in mean field studies (see section 5.1 for more on this).

More generally, the type I/II states are examples of "(multi-) fragmented" condensates [112], see also [108], in the sense that they contain several macroscopically occupied elements in the density matrix. For instance, for the BTC- and for (any component of) the BDC-state we have $\langle n_{m\alpha}\rangle_{\rm BDC} = (1 - \delta_{m,2})(1 - \delta_{\alpha\downarrow})q/2$, $\langle n_{m\alpha}\rangle_{\rm BTC} = n/3$. Since the spin is fixed in these states, $(\Delta n_\alpha)^2 \equiv \langle (n_\alpha - \langle n_\alpha\rangle)^2\rangle = 0$, where $n_\alpha = \sum_{m=0,1,2} n_{m\alpha}$ (see the appendix A). However, within each spin component, the fluctuations of the boson number between orbitals is of the order of the system size: $(\Delta n_{m\alpha})^2_{\rm BDC} = q(q+2)/12$, $(\Delta n_{m\alpha})^2_{\rm BTC} = n(n+3)/18$. This is an indication that, as in the case of the singlet ground state at $L = 0$ in the antiferromagnetic regime and the related "polar" mean field state [108], it may be best to think of these states as broken symmetry states. That is the approach we will take in section 5.1.

4.3.2 Exact ground states at $c_2 = 0$ as a function of L or ω

The ground state of a rotating gas with N spin-1 bosons in the LLL and a spin-independent ($c_2 = 0$) interaction is formed by a sequence of type I or II states lying on a certain path in (p, q)-space as L increases. To find the ground state in a rotating frame of reference, we need to find the ground state of H_ω, equation (4.3), instead.

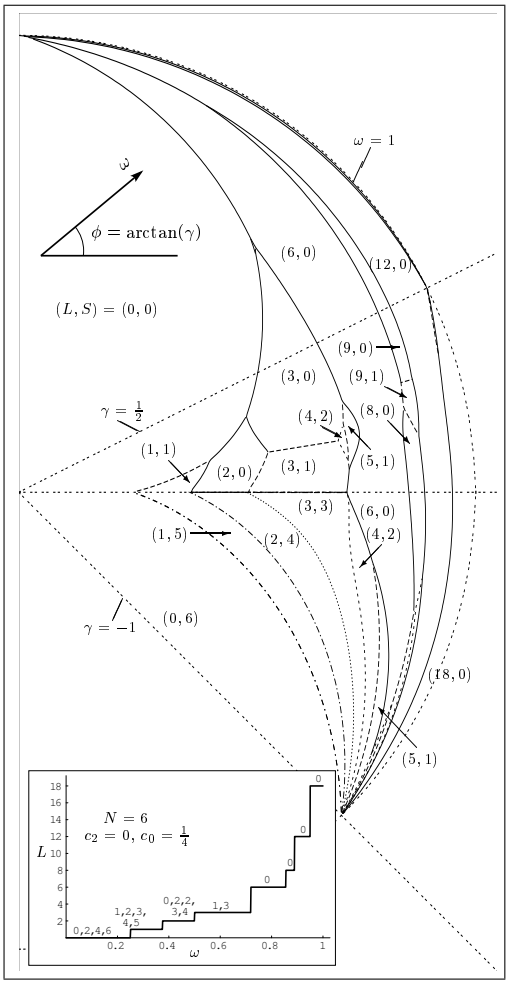

Figure 4.4: Ground state quantum numbers (L, S) in region II for $N = 6$ spin-1 particles in the planar (disc) geometry, as a function of the driving frequency ω (plotted radially) and the ratio γ (corresponding to the angle with respect to the horizontal axis). The special directions $g_2 = 0$, $c_2 = 0$, $g_0 = 0$, $c_0 = 0$ are shown as double-dotted radial lines. The inset shows a cut along the $c_2 = 0$ direction, with the angular momentum given on the vertical axis and the (degenerate) spin values S marked at each of the steps. In this figure, the parameters c_0, c_2, and ω are in units of ω_0, and the value $c_0 = 0.25$ is used in the main figure as well as in the inset. For additional discussion, see the main text.

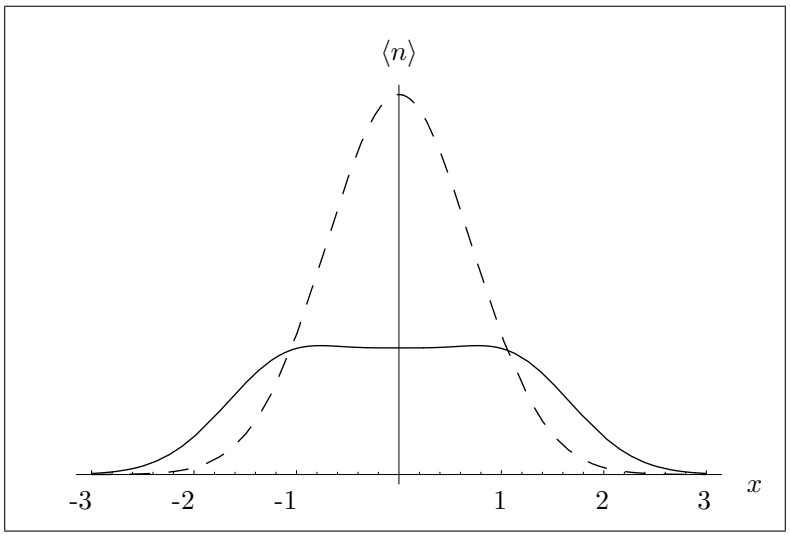

Figure 4.5: Two dimensional density profiles versus x at $y = 0$ in the LLL model: BTC (solid line) and nonrotating Bose-Einstein condensate (broken line). The vertical axis is in units of the particle number $N = 3n$.

Since this Hamiltonian contains only two energy scales, the ground state angular momentum per particle L/N can be written as a function of the ratio $(\omega - \omega_0)/(Nc_0)$. For finite boson number this function consists of a sequence of steps, as can be seen in figure 4.4. It turns out that (thanks to our judicious choices of factors of N) the limit $N \to \infty$ with L/N and $(\omega - \omega_0)/c_0N$ fixed of this function exists, and this is the most convenient information to display. In the following we determine the path of the ground states in (p, q)-space as a function of L, and the $L(\omega)/N$ behavior of the ground states in this limit for both the sphere ($N_v = 2$) and the disc ($N_v = \infty$) in the regime $L/N \leq 1$.

Ground states on the sphere at $N_v = 2$

On the sphere, our notion of rotation is such that the $SO(3)_{\rm orb}$-angular momentum $\tilde{L}$ decreases as the system rotates faster and faster. With three orbitals ($N_v = 2$) we have $\tilde{L}_z = N - L$ (see section 4.1.1). (We consider $N_v = 2$ because this case can just accommodate $L \leq N$.) At $\tilde{L} = N$, we know already that the $|N, 0, 0\rangle^I$ multiplet forms the ground state. As $\tilde{L}$ starts to decrease, again a type I state has the lowest energy; the (p, q)-path is parametrized by $(2\tilde{L} - N, N - \tilde{L})$. Bosons are gradually added to the $m = 1$ orbital and form anti-symmetrized pairs with the remaining ones. The point up to which this continues can be found by comparing the energies of $|2\tilde{L} - N, N - \tilde{L}, 0\rangle^I$ and $|2\tilde{L} - N + t, N - \tilde{L} - t, t/3\rangle^I$. After minimizing with respect to t this yields the critical $SU(3)$-indices $(p, q)_c = (N/3, N/3)$. At this point, with $\tilde{L} = 2N/3$, ground

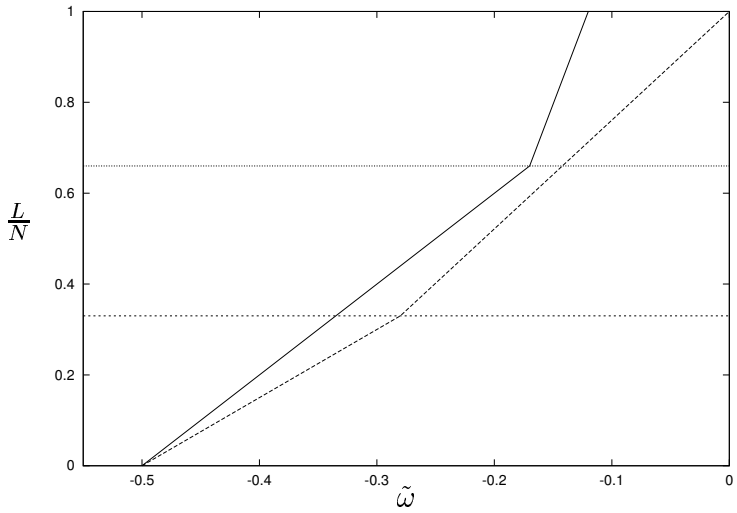

Figure 4.6: L/N as $N \to \infty$ of the ground state on the disc (bold line) and on the sphere with $N_v = 2$ (dashed line), as functions of $\tilde{\omega} = (\omega - \omega_0)/c_0 N$ at $c_2 = 0$. The horizontal lines mark the values $L/N = 1/3$ and $L/N = 2/3$. The cusps in both curves indicate the point where the $m = 2$ quantum orbital is first used in the ground state.

states with a nonzero ($n > 0$) number of triplets become energetically favorable. In the remaining region, $2N/3 \geq \tilde{L} \geq 0$, type I states are the ground states following the path $(p, q) = (\tilde{L}/2, \tilde{L}/2)$. Eventually this terminates on the BTC at $\tilde{L} = 0$. L/N of the ground state as a function of the rotation drive ω shows a cusp at $\tilde{L}/N = 2/3$ ($L/N = 1/3$), as is shown in figure 4.6.

Ground states on the disc

For a system on the disc ($N_v = \infty$), the results are rather different. We will again present the ground states in order of increasing L. At $L = 0$, the $|N, 0, 0\rangle^I$-multiplet forms the ground state as we know. For $L \leq N/2$ the ground state is formed by a type I state with $n = 0$ and $SU(3)$-quantum numbers $(p, q) = (N - 2L, L)$. This state terminates on the BDC at $L = N/2$. In this range, increasing L leads, as on the sphere, to more bosons occupying the $m = 1$ orbital, forming anti-symmetrized pairs with the ones in the $m = 0$ orbital. For $L \geq N/2$, the type II states have the lowest energy. As L increases, bosons move from the $m = 0$ into the $m = 1$ orbital, decreasing the number of doublets, and giving type II states at $(p, q) = (2L - N, N - L)$. Comparing the energies of $|tN, (1-t)N/2, 0\rangle^{II}$ and $|(t-s)N, (1-t)N/2, sN/3\rangle^{II}$, we can determine the point where it becomes favourable for triplets to enter the ground state. We find a critical angular momentum $L = (1 - t_c)N$ with $t_c \sim 1/3 - 3/N$, which approaches $L = 2N/3$ for N large. For $L \geq 2N/3$ the number of triplets is gradually increasing as L grows. Minimizing $|2L - N - s, N - L, s/3\rangle^{II}$ with respect to s, we find that the ground state is now the type II state with $s(N, L) = 3L - 2N$, giving $(p, q, n) = (N - L, N - L, L - 2N/3)$. For $L = N$ the ground state is the BTC with $p = q = 0$, $n = N/3$.

To summarize the above results, for $0 \leq L \leq N/2$ the ground state is given by $|N - 2L, L, 0\rangle^I$ and for $N/2 \leq L \leq 2N/3$ by $|2L - N, N - L, 0\rangle^{II}$. In the remaining range $2N/3 \leq L \leq N$ the number of 3-body singlets is nonzero, and the ground state is given by $|N - L, N - L, L - 2N/3\rangle^{II}$. Minimizing the energy in a rotating frame of reference leads to the $L(\omega)/N$-dependence of the ground states for $N \to \infty$ which is depicted in figure 4.6. In this figure, the curve shows a cusp at the point where the $m = 2$ orbital first enters the ground state configuration, which is at $L/N = 2/3$ for the disc with N large. A signature of this cusp in an experimental system might be a change in the expansion rate (the rate of change of the outer radius of the drop with respect to ω) if the angular momentum exceeds $2N/3$. We shall see that the cusp survives in the anti-ferromagnetic regime, $c_2 > 0$.

It is important to contrast all this with the well-known behavior of scalar bosons in a rotating trap [45, 43]. In the latter case there is a jump from $L/N = 0$ to $L/N = 1$ (for all N) when one vortex enters the system, whereas for spin-1 bosons we find a continuous $L(\omega)/N$ curve with a discontinuous slope.

$S\backslash\tilde{L}$	0	1	2	3	4	5	6
0	1						
1		1					
2			1				
3				1			
4	1		1		1		
5		1	1	1	1	1	
6	1		1		1		1

$S\backslash\tilde{L}$	$\frac{1}{2}$	$\frac{3}{2}$	$\frac{5}{2}$	$\frac{7}{2}$	$\frac{9}{2}$	$\frac{11}{2}$	$\frac{13}{2}$	$\frac{15}{2}$
0	1		1					
1	1	2	1	1				
2	1	2	2	1	1			
3	1	2	2	2	1	1		
4	1	2	2	2	2	1	1	
5		1	1	1	1	1		1

$S\backslash L$	0	1	2	3	4	5	6	...
0							1	...
1						1	1	...
2					1	1	3	...
3				1	1	3	5	...
4			1	1	3	4	8	...
5		1	1	2	3	5	6	...
6	1		1	1	2	2	4	...

Figure 4.7: Degeneracies of zero-energy ground states on the sphere at $\gamma = -1$ for $N = 6$, $N_v = 2$ (top left), $N = 5$, $N_v = 3$ (top right) and $N = 6$, $N_v = \infty$. All multiplicities refer to highest weight states of the orbital $SO(3)$ symmetry.

4.4 The boundaries of region II

The behavior at the phase boundaries I–A/II and I–B/II (see figure 4.2) deserves special attention. At the boundary I–B/II, where $\gamma = c_2/c_0 = -1$, the Hamiltonian simplifies as $g_2 = 0$ and only the contact interaction which projects onto the spin-singlet channel remains. As a result of this, large degeneracies occur. For example, all fully-polarized states ($S = N$) have zero energy. We have not obtained analytic expressions for these degeneracies. That they are not due to the specific geometry was observed on the torus. The zero energy states are not sensitive to changes in the geometry. As examples of these degeneracies, we have in figure 4.7 tabulated the $\tilde{L}$, S quantum numbers of the zero energy states for $N = 6$, $N_v = 2$ and for $N = 5$, $N_v = 3$ on the sphere, and for $N = 6$ particles in the disc geometry.

A Appendix: differential operator representation

Here we briefly describe a technique which is useful for a systematic calculation of eigen values and expectation values of some of the wavefunctions discussed in this chapter. Second quantized wavefunctions can be expressed as derivatives of the coherent state

$$|\Psi(\{\vec{r}_\alpha\})\rangle = \exp\big[\sum_\alpha \vec{B}^\dagger_\alpha \cdot \vec{r}_\alpha\big]|0\rangle. \tag{4.15}$$

Here $\vec{B}^\dagger_\alpha = (b^\dagger_{0,\alpha}, b^\dagger_{1,\alpha}, b^\dagger_{2,\alpha})$ is a vector containing the Fock operators in a spin component $\alpha \in \{0, \uparrow, \downarrow\}$. We emphasize that the auxiliary variables $\{\vec{r}_\alpha\}$ *do not* represent spatial coordinates. For instance, the $SU(3)$-symmetric type I states of equation (4.11) can be represented in the following way

$$|p,q,n\rangle^I \propto \Big\{[\vec{e}_1 \cdot \vec{\nabla}_\uparrow]^p [\vec{e}_2 \cdot (\vec{\nabla}_\uparrow \times \vec{\nabla}_0)]^q [\vec{\nabla}_0 \cdot (\vec{\nabla}_\uparrow \times \vec{\nabla}_\downarrow)]^n |\Psi(\{\vec{r}_\alpha\})\rangle\Big\}_{\vec{r}_\alpha = 0}. \tag{4.16}$$

For a system containing N particles, the constraint $N \equiv p + 2q + 3n$ must be satisfied. The differential operators $\{\vec{\nabla}_\alpha\}$ act on the coherent state and generate the creation operators in the spin-level α. Setting $\vec{r}_\alpha = 0$ afterwards indeed produces the second quantized wave functions of the form of equation (4.11). Note that the type II states discussed in this chapter can *not* easily be expressed using this representation.

In the following we use the type I states as example. As long as physical operators can be expressed in second quantized form, they can also be represented as a certain combination of differential operators acting on the state of equation (4.15). These operators can therefore be evaluated analytically on a given wavefunction. The crucial identity for calculating expectation values is given by

$$\langle \Psi(\{\vec{r}_\alpha\}) | \Psi(\{\vec{r}'_\alpha\})\rangle = e^{\sum \vec{r}_\alpha \cdot \vec{r}'_\alpha}. \tag{4.17}$$

The norm of the wavefunctions in equation (4.16) (for instance) can be calculated by expanding the exponent and evaluating the operator $\hat{O}^{p,q,n}_r \hat{O}'^{p,q,n}_r$, with $\hat{O}^{p,q,n}_r \equiv [\vec{e}_1 \cdot \vec{\nabla}_\uparrow]^p [\vec{e}_2 \cdot (\vec{\nabla}_\uparrow \times \vec{\nabla}_0)]^q [\vec{\nabla}_0 \cdot (\vec{\nabla}_\uparrow \times \vec{\nabla}_\downarrow)]^n$, on the resulting terms

$$\begin{aligned} \langle p,q,n|p,q,n\rangle &= \frac{1}{N!}\Big\{\langle 0|\hat{O}^{p,q,n}_{r'} \hat{O}^{p,q,n}_r \big(\sum \vec{r}'_\alpha \cdot \vec{r}_\alpha\big)^N |0\rangle\Big\}_{\vec{r}_\alpha, \vec{r}'_\alpha = 0} \\ &= p! \prod_{k=1}^{q} k(k+p+1) \prod_{l=1}^{n} l(l+q+1)(l+q+p+2)\,. \end{aligned} \tag{4.18}$$

Only the N-th order term gives a non-zero contribution, since the operator $\hat{O}^{p,q,n}_r$ is of order N. Lower order terms will be annihilated by the differential operators and higher order terms will be set to zero afterwards because of $\vec{r}_\alpha, \vec{r}'_\alpha = 0$.
When calculating expectation values using the described method, one must make sure that operators are normally ordered before evaluating the differential operators on the coherent state. The calculation only makes sense if normal ordering is taken

into account because the differential operators are commuting objects and the Fock operators are not. The role of normal ordering becomes clear in the following example where the density in a spin component α is calculated

$$\begin{aligned}
\langle \rho_\alpha \rangle &= \sum_m \frac{\langle p,q,n|\ b^\dagger_{m\alpha} b_{m\alpha}\ |p,q,n\rangle}{\langle p,q,n|p,q,n\rangle} \\
&= \sum_m \frac{\langle p,q,n|\ b_{m\alpha} b^\dagger_{m\alpha} - [b_{m\alpha}, b^\dagger_{m\alpha}]\ |p,q,n\rangle}{\langle p,q,n|p,q,n\rangle} \\
&= \frac{\left\{ \langle 0|\hat{O}^{p,q,n}_{r'} \vec{\nabla}^{r'}_\alpha \cdot \vec{\nabla}^{r}_\alpha \hat{O}^{p,q,n}_{r} \big(\sum \vec{r}'_\beta \cdot \vec{r}_\beta \big)^{N+1} |0\rangle \right\}_{\vec{r}_\beta, \vec{r}'_\beta = 0}}{\langle p,q,n|p,q,n\rangle\ (N+1)!} - 3 \\
&= n + p\delta_{\alpha\uparrow} + (1-\delta_{\alpha\downarrow})q\ .
\end{aligned}$$

Note that in this calculation the relevant operator is of order $N+1$. From the above result, it is straightforward to calculate the number fluctuations in a spin level α

$$\begin{aligned}
\langle (\rho_\alpha - \langle \rho_\alpha \rangle)^2 \rangle &= \sum_{m,n} \langle b_{m\alpha} b_{n\alpha} b^\dagger_{m\alpha} b^\dagger_{n\alpha} \rangle - (3 + \langle \rho_\alpha \rangle)(4 + \langle \rho_\alpha \rangle) \\
&= \frac{\left\{ \langle 0|\hat{O}^{p,q,n}_{r'} \vec{\nabla}^{r'}_\alpha \vec{\nabla}^{r'}_\alpha : \vec{\nabla}^{r}_\alpha \vec{\nabla}^{r}_\alpha \hat{O}^{p,q,n}_{r} \big(\sum \vec{r}'_\beta \cdot \vec{r}_\beta \big)^{N+2} |0\rangle \right\}_{\vec{r}'_\beta, \vec{r}_\beta = 0}}{\langle p,q,n|p,q,n\rangle\ (N+2)! \qquad -(3 + \langle \rho_\alpha \rangle)(4 + \langle \rho_\alpha \rangle)} \\
&= 0.
\end{aligned}$$

Other expectation values can be found in principle as long as the operator and the used wavefunction can be expressed in second quantized language. Although it is relatively easy to obtain the above results for the type I states of equation (4.11), we can not analyze the type II states in this way, because they cannot easily be expressed using second quantized language.

Chapter 5

Rotating spin-1 condensates: mean field analysis

Continuing our analysis of rotating spin-1 bosons, we[1] *use mean field theory within the lowest Landau level, for slow rotation and general nonzero spin-dependent interactions. We describe ground state spin textures at different interaction strengths, and discontinuous transitions between distinct spin textures as function of the angular momentum. Furthermore, the various skyrmion and vortex lattices which occur at higher angular velocities are described.*

5.1 Slow rotation: lowest Landau level mean field theory

At low rotation rates, the typical boson occupation numbers $\langle n_{m\alpha} \rangle$ of the occupied ($n_{m\alpha} \neq 0$) single-particle states are large compared with 1. In this situation, a mean field (or classical) approach to the problem is generally expected to be quantitatively accurate. In such an approach, the boson operators are replaced by expectation values, which are complex c-numbers: $b^\dagger_{m\alpha} \to b^*_{m\alpha}$, and the second-quantized Hamiltonian is then minimized with respect to both the magnitude and phase of these numbers to find the ground states. In essence the resulting state is a Bose condensate with the bosons condensed in one linear combination of the single-particle states. This typically involves breaking the orbital and spin symmetries, as well as particle number conservation. (States with definite values of the good quantum numbers such as N, S, L can be obtained afterwards by applying a projection to the mean field quantum state.) In the case of very low rotation, where $L \leq N$, we have seen that (neglecting the subtleties that arose for type II states) the states essentially involve

[1] This chapter is based on a collaboration with F. J. M. van Lankvelt, K. Schoutens and N. Read, see [7, 8].

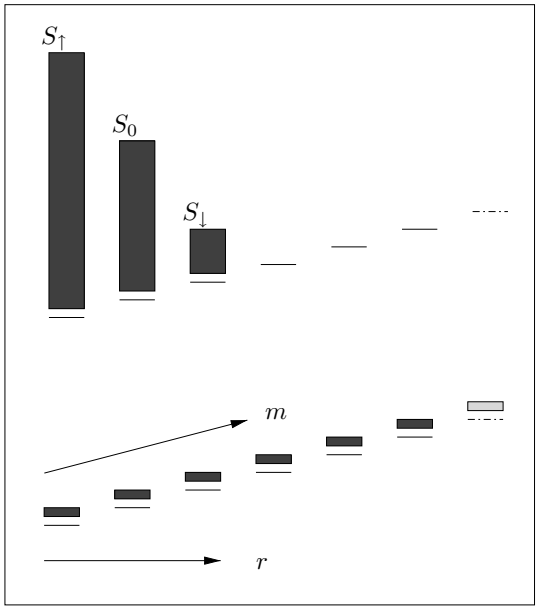

Figure 5.1: Schematic picture of typical LLL-orbital occupation numbers (black bars) of a mean field configuration (upper part) and an exact quantum ground state (lower part).

only the $m = 0$, 1, and 2 states, so that the basis set for the mean field calculation is particularly small, see figure 5.1. In these cases, the mean occupation numbers of the single particle states are of order N, and their energies exceed the exact ground state energy (which is of order N^2) by an amount of order N. In this section we pursue this mean field calculation for this regime. This gives us easy access to the ground states at large N for $c_2 \neq 0$ in[2] region II. In the following section, we study instead the mean field states at larger rotation, which can be assumed to be states in which the translational and rotational symmetry group of the plane is broken to that of a lattice.

In terms of the complex numbers $b_{m\alpha}$, $b^*_{m\alpha}$, the energy becomes a quartic polynomial and the ground state can be found by minimizing this polynomial with respect to these variables. This is done here with the *mean* boson number $\langle N\rangle = \sum_{m\alpha} b^*_{m\alpha} b_{m\alpha}$ and angular momentum $\langle L\rangle = \sum_{m\alpha} m b^*_{m\alpha} b_{m\alpha}$ fixed at the values N, L, respectively. The spin is not constrained at all. For $c_2 = 0$ the Hamiltonian on the sphere takes the

[2]For a focused study of the ground states at slow rotation and $|c_2|/|c_0| \simeq .05$, see [113].

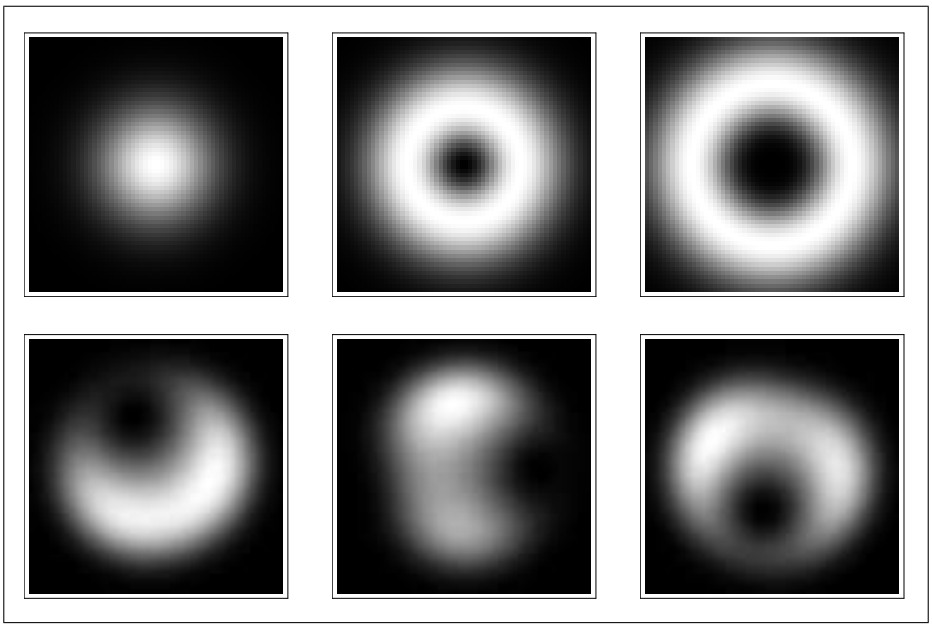

Figure 5.2: Two-dimensional density profile of each of the spin components of two LLL mean field ground state configurations at $c_2 = 0$, $L = N$. The upper panels shows the axi-symmetric spin-vector configuration $(\phi_0(z), \phi_1(z), \phi_2(z))$. The two configurations share the same distribution of the total density, and they are related by the $SU(3)$ symmetry. For $c_2 \neq 0$, there are similarly distinct profiles related by $SO(3)$ symmetry.

form

$$H_n = c_0 \sum_{\alpha\beta} \sum_{m_1 \cdots m_4} V_{m_1 m_2 m_3 m_4} b^*_{m_1 \alpha} b^*_{m_2 \beta} b_{m_3 \alpha} b_{m_4 \beta},$$

with matrix elements given by equation (4.4). For $c_2 \neq 0$, the matrix elements in the additional term consist of $V_{m_1 \cdots m_4}$ multiplied by matrix elements of $\vec{S}_i \cdot \vec{S}_j$, which depend on the $\alpha_1, \ldots, \alpha_4$ labels of the bosons. The second quantized form of this term is given by equation (4.6).
The fact that mean-field configurations break the various symmetries implies that the minima of the mean field energy form orbits under the action of these same symmetries. On a disc, and at $c_2 \neq 0$, one expects and finds that, typically, from a generic minimum there are 5 flat directions leading to adjacent minima with equal energy. These flat directions correspond to the 3 generators of the $SO(3)$ spin symmetry, an overall phase, and an orbital $O(2)$ rotation. For spin-independent interactions the symmetry orbits are generically 10-dimensional.

One convenient quantity to plot is the expectation value $\langle \vec{S} \rangle$ of the spin, whose length is conserved under global spin rotations. Usually this quantity is expressed as

$\sum_m \sum_{\alpha\beta} b^*_{m\alpha} \vec{S}_{\alpha\beta} b_{m\beta}$, with the spin-1 matrices given by

$$S^{(x)}_{\alpha\beta} = \frac{1}{\sqrt{2}} \begin{pmatrix} 0 & 1 & 0 \\ 1 & 0 & 1 \\ 0 & 1 & 0 \end{pmatrix}, \qquad S^{(y)}_{\alpha\beta} = \frac{1}{\sqrt{2}} \begin{pmatrix} 0 & -i & 0 \\ i & 0 & -i \\ 0 & i & 0 \end{pmatrix},$$
$$S^{(z)}_{\alpha\beta} = \begin{pmatrix} 1 & 0 & 0 \\ 0 & 0 & 0 \\ 0 & 0 & -1 \end{pmatrix}. \tag{5.1}$$

In special cases, the expectation value $\langle \vec{S} \rangle$ is axi-symmetric; in the more general case it is non-axisymmetric and the mean field configuration breaks the orbital $O(2)$ symmetry. Another useful quantity is the three-component condensate wavefunction (analogous to the familiar spinor for spin-1/2), which is the expectation value of the field operator, $\langle \psi_\alpha(z) \rangle = \sum_m b_{m\alpha} \phi_m(z)$ (see section 4.1.1). It is a vector in the $\alpha = \uparrow$, 0, $\downarrow$ basis. From this we can plot the density in each spin component in position space. This could be accessed experimentally if after switching off the trap to allow the particle cloud to expand, a Zeeman term is switched on, which causes the three α components to separate as they expand.

As an example, we plot in figure 5.2 the two-dimensional density profile in each spin component of two different mean field ground state configurations at $c_2 = 0$, $L = N$. The top frame shows the densities for the condensate proportional to (ϕ_0, ϕ_1, ϕ_2); the lower frame shows a configuration that is related to this by an $SU(3)$ rotation. The total density in each of the $m = 0$, 1, 2 orbitals is an $SU(3)$ invariant, and it is the same for both configurations shown in figure 5.2. The mean field energy of these configurations is $E_{MF} = \frac{11}{48} N^2$, in agreement with order N^2 term in the energy of the exact quantum (BTC) ground state, equation (4.12) with $N_v = 2$, $p = q = 0$ and $n = N/3$. First we consider the disc geometry with $c_2 = 0$. Carrying out the mean field minimizations, we find in terms of $\ell = L/N$ that for $0 \le \ell \le 2/3$ the number densities $\langle n_m \rangle = \sum_\alpha b^*_{m\alpha} b_{m\alpha}$ in the orbitals of the mean field ground states behave like (here and in the remainder of this section, these numbers are normalized so that they sum to 1) $\langle n_0 \rangle = 1 - \ell$, $\langle n_1 \rangle = \ell$ and $\langle n_2 \rangle = 0$. For $\frac{2}{3} \le \ell \le 1$ we find $\langle n_0 \rangle = \frac{1}{3}$, $\langle n_1 \rangle = \frac{4}{3} - \ell$ and $\langle n_2 \rangle = \ell - \frac{2}{3}$. All this is in agreement with the results derived from the exact quantum ground states in section 4.3.

For very small interaction ratios $|\gamma| \ll 1$, the total densities in the orbitals remain the same as for $\gamma = 0$, but there is non-trivial structure in the spin dependence, leading to spin transitions at critical values of $\ell = L/N$, as we will describe shortly.

In figure 5.3 we have plotted region II of the phase diagram, this time with ℓ radially. The shaded regions show where only the first two orbitals ($m = 0, 1$) are present in the condensate. One region is a tiny strip near $\ell = 1$ for $\gamma \ge (7 + 4\sqrt{2})/17 \approx 0.75$, where the $(m, \alpha) = (1, 0)$ state is occupied by all the bosons. This state can be seen as a "polar" vortex, since it has the same spin state as the polar Bose-Einstein condensate. The other region, centered (roughly) around the $c_2 = 0$ axis, contains states in which both the $m = 0$ and $m = 1$ orbitals are used.

In the anti-ferromagnetic regime for $\ell \le 1$ there is a large area where the $m = 3$

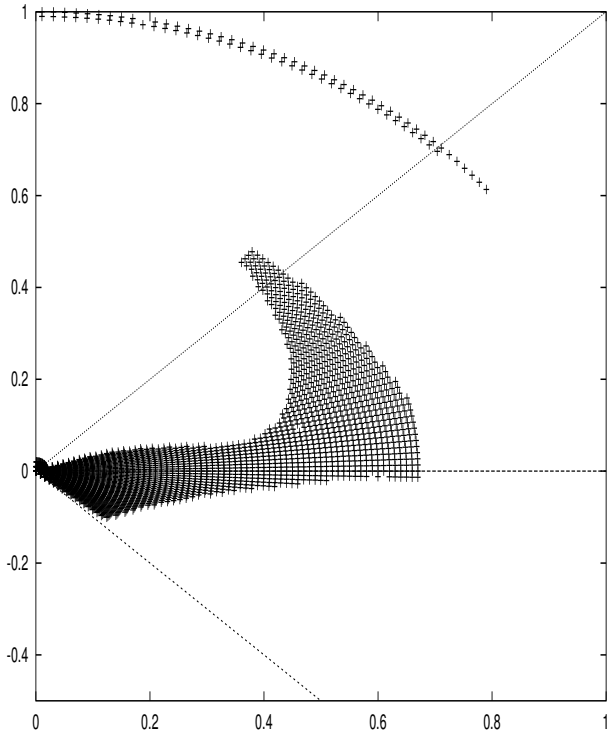

Figure 5.3: Regions in the γ, ℓ plane in which only the $m = 0$ and $m = 1$ orbitals are present in the mean field ground state on the disc are shaded. The angular coordinate is $\phi = \arctan\gamma$ and $\ell = L/N$ is plotted radially. In the shaded strip near $\ell = 1$, a "polar vortex" forms the ground state. The dotted lines mark the $\gamma = \pm 1$ and $\gamma = 0$ directions.

orbital requires a non-zero density; in this area, mean field theory in which only the first three orbitals are used is not valid. However, around and at the $SU(3)$-axis and around the polar vortex as well as in the ferromagnetic regime, the density in the $m = 3$ orbital is very small for $\ell \leq 1$ and can safely be ignored. Besides, if the energy H_ω in a rotating frame (see equation (4.3)) is minimized, only the states which use the first three orbitals $m = 0, 1, 2$ are of interest for $\ell \leq 1$. [This is with the exception of the vicinities of the boundaries of region II (see figure 4.2) at $\gamma \to \infty$ and at $\gamma = -1$.]

In the following subsections we present results for the LLL mean field ground state for $|\gamma| \ll 1$, in both the ferromagnetic and anti-ferromagnetic regimes, and we discuss the ground states at $\ell = 1$ for general values of γ.

Our mean field results pertain to the LLL, relevant for the regime of weak interactions, and they thus differ from the mean field solutions of the GP equations [59, 114]. Nevertheless, there is agreement on some of the important features, such as the smooth dependence of L on ω in the ferro regime, and the role of the state with a single π-disclination near $\ell = 0.5$ in the antiferromagnetic regime [114].

5.1.1 Anti-ferromagnetic interactions

We now specify the mean field ground states, given in the form of a three-component condensate wave function, for small, positive $\gamma = +\epsilon$, and for $\ell \leq 1$. As before, the condensate wave function is a vector in the $\alpha = \uparrow, 0, \downarrow$ basis. In the table below we specify the mean occupation numbers of the four states that we found.

	$\langle n_{0\uparrow}\rangle$	$\langle n_{0\downarrow}\rangle$	$\langle n_{10}\rangle$	$\langle n_{1\uparrow}\rangle$	$\langle n_{20}\rangle$	$\langle n_{2\uparrow}\rangle$
$0 \leq \ell \leq \ell_a^\epsilon$	$\frac{1}{2}(1-\ell)$	$\frac{1}{2}(1-\ell)$	ℓ	0	0	0
$\ell_a^\epsilon \leq \ell \leq \frac{2}{3}$	0	$1-\ell$	0	ℓ	0	0
$\frac{2}{3} \leq \ell \leq \ell_b^\epsilon$	0	$\frac{1}{3}$	0	$\frac{4}{3}-\ell$	$\ell-\frac{2}{3}$	0
$\ell_b^\epsilon \leq \ell \leq 1$	0	$\frac{1}{3}$	$\frac{4}{3}-\ell$	0	0	$\ell-\frac{2}{3}$

Table 5.1: Occupation numbers of the LLL mean field ground state with small anti-ferromagnetic interaction $\gamma = \epsilon$.

Note that the condensates given in this table are specific representatives of families of condensates that are related by the $SO(3)_{\rm spin}$ symmetry. There are two critical values, $\ell_a^\epsilon = \frac{4}{7} - \frac{\sqrt{2}}{7} \approx 0.37$ and $\ell_b^\epsilon = 10 - 4\sqrt{5} - \frac{4}{3}\sqrt{85 - 38\sqrt{5}} \approx 0.83$, where we see a discontinuous rearrangement of the condensate configuration and of $\langle \vec{S} \rangle$. For nonzero γ, these changes in the condensate are continuous; they become singular (discontinuous) only as $\gamma \to 0^+$.

For $\ell < \ell_a^\epsilon$, the condensate can be represented by $(\frac{\lambda}{\sqrt{2}}\phi_0(z), \eta\phi_1(z), \frac{\lambda}{\sqrt{2}}\phi_0(z))$ with $\lambda = \sqrt{N-L}$, $\eta = \sqrt{L}$. Applying $SO(3)_{\rm spin}$ rotations, one finds alternative representations such as $(\frac{1}{\sqrt{2}}[\lambda\phi_0(z) - \eta\phi_1(z)], 0, \frac{1}{\sqrt{2}}[\lambda\phi_0(z) + \eta\phi_1(z)])$. The $SO(3)_{\rm spin}$-invariant

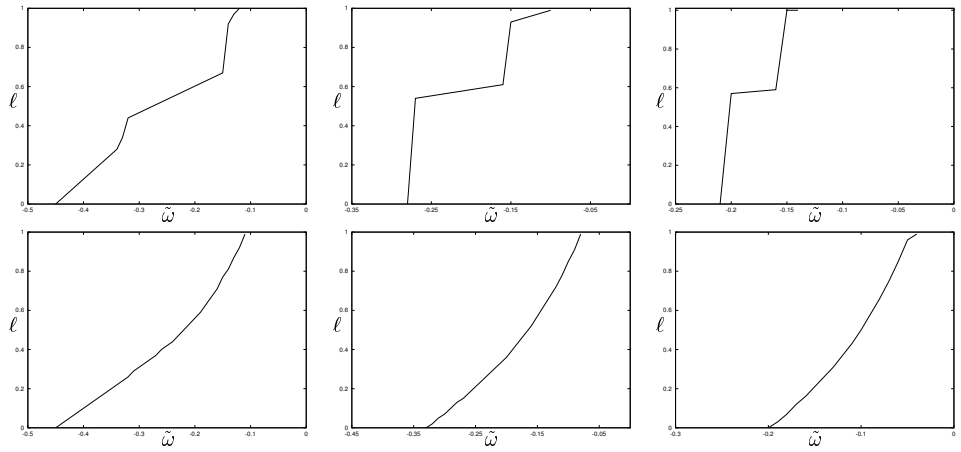

Figure 5.4: The ground state angular momentum per particle ℓ on the disc as a function of $\tilde{\omega} = (\omega - \omega_0)/c_0 N$ for various interaction strengths and slow rotation. Upper figures: anti-ferromagnetic regime, $\phi = .1,\ .5,\ .75$. Lower figures: ferromagnetic regime, $\phi = -.1,\ -.3,\ -.5$.

quantity $|\langle \vec{S} \rangle|^2$ is found to be

$$|\langle \vec{S} \rangle|^2 = \frac{N^2}{\pi^2} \ell(1-\ell)(z+\bar{z})^2 e^{-2|z|^2} \ . \tag{5.2}$$

The state that emerges at $\ell > \ell_a^\epsilon$ corresponds to $(\eta\phi_1(z), 0, \lambda\phi_0(z))$, leading to

$$|\langle \vec{S} \rangle|^2 = \frac{N^2}{\pi^2} ([1-\ell] - \ell|z|^2)^2 e^{-2|z|^2} \ . \tag{5.3}$$

For $\ell \neq 1/2$, the integrated value of $\langle \vec{S} \rangle$ for this state is non-zero and there is a spontaneous magnetization. In figure 5.5 a two-dimensional plot of $\langle \vec{S} \rangle$ at both sides of the spin transition at $\ell = \ell_a^\epsilon$ is shown. The state at $0 < \ell < \ell_a^\epsilon$ can be viewed as a configuration of two π-disclinations off the center of the trap, while the state in the regime $\ell_a^\epsilon < \ell < 2/3$ (or possibly even as far as ℓ_b^ϵ) can be understood as a single π-disclination in the polar state. The angular momentum for which the $m = 2$ orbital is first occupied in the mean field ground state, $\ell = \frac{2}{3}$, is robust against small anti-ferromagnetic interactions. For $\gamma = +\epsilon$, $2/3 < \ell < \ell_b^\epsilon$, the condensate can be represented as $(\tau\phi_1(z), \sigma\phi_2(z), \xi\phi_0(z))$, with $\xi = \sqrt{\frac{N}{3}}$, $\sigma = \sqrt{L - \frac{2N}{3}}$, $\tau = \sqrt{\frac{4N}{3} - L}$, while for $\ell_b^\epsilon < \ell \leq 1$ we have $(-\sigma\phi_2(z), \tau\phi_1(z), \xi\phi_0(z))$.

In figure 5.4, we have depicted the ground state angular momentum per particle, ℓ, as a function of the rotation frequency ω for some positive values of γ. It is seen that upon increasing γ a semi-plateau (a distinguished part of the curve on which

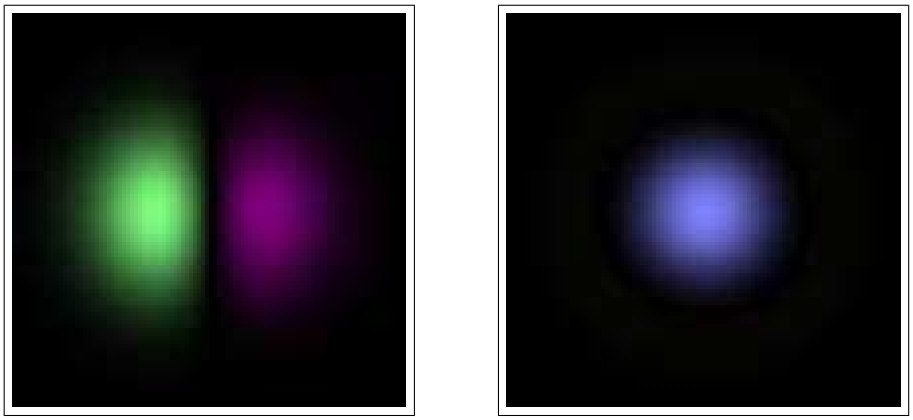

Figure 5.5: Two-dimensional plot of $\langle\vec{S}\rangle$ at both sides of the spin transition at $\ell = \ell_a^\epsilon$. The intensity codes the length $|\langle\vec{S}\rangle|$, while the color indicates the direction on the spin sphere as in figure 5.7 below. The left and right pictures correspond to eqs. (5.2) and (5.3), respectively.

the angular momentum increases gradually) develops. Upon increasing γ further, the semi-plateau becomes flatter and the width decreases, until for γ larger than some critical value $\gamma_c \approx 1.19$, $\ell(\omega)$ jumps from $\ell = 0$ to an $\ell = 1$ plateau at a critical frequency ω_c given by $\omega_0 - \omega_c \approx 0.15 c_0 N$. This is a transition from the non-rotating state to the polar vortex, analogous to what occurs in the scalar boson case.

5.1.2 Ferromagnetic interactions

With small negative $\gamma = -\epsilon$ the mean field ground states for slow rotation are characterized (up to $SO(3)_{\rm spin}$ rotations) by the occupation numbers given in table 5.2. Again, we find two spin transitions, the first at $\ell_a^{-\epsilon} = 2 - \sqrt{2} \approx 0.59$ and the second at $\ell_b^{-\epsilon} \approx 0.69$.

	$\langle n_{00}\rangle$	$\langle n_{0\downarrow}\rangle$	$\langle n_{10}\rangle$	$\langle n_{1\downarrow}\rangle$	$\langle n_{2\uparrow}\rangle$
$0 \le \ell \le \ell_a^{-\epsilon}$	0	$1-\ell$	ℓ	0	0
$\ell_a^{-\epsilon} \le \ell \le \frac{2}{3}$	$1-\ell$	0	0	ℓ	0
$\frac{2}{3} \le \ell \le \ell_b^{-\epsilon}$	$\frac{1}{3}$	0	0	$\frac{4}{3}-\ell$	$\ell-\frac{2}{3}$
$\ell_b^{-\epsilon} \le \ell \le 1$	0	$\frac{1}{3}$	$\frac{4}{3}-\ell$	0	$\ell-\frac{2}{3}$

Table 5.2: Mean occupation numbers of the LLL condensate for small ferromagnetic interaction $\gamma = -\epsilon$.

For $\ell < \ell_a^{-\epsilon}$ the condensate can be represented by $(0, \eta\phi_1(z), \lambda\phi_0(z))$ with λ and η

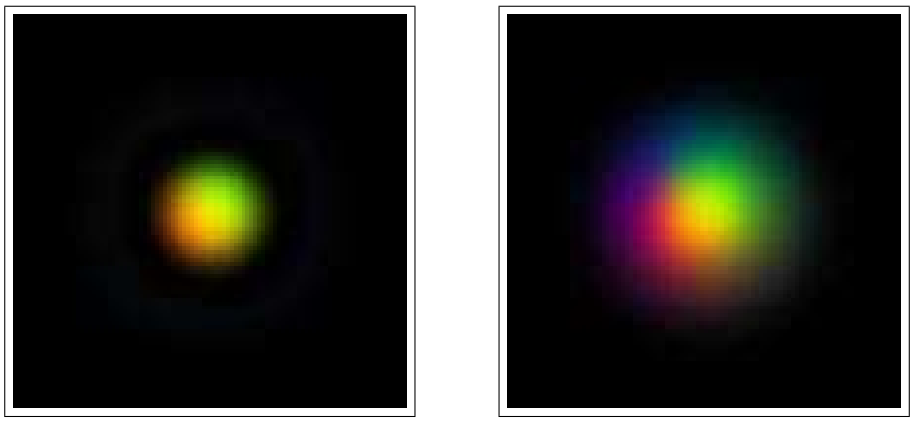

Figure 5.6: The spin texture at $l = 1$ for $\gamma = \pm\epsilon$. The left side is the anti-ferromagnetic case, the right is the ferromagnetic case. The color coding is as in figure 5.7.

as given above. In this state, the expectation values of the components of the spin vector take the following form

$$\begin{aligned}
\langle S_x \rangle &= \frac{N}{\pi\sqrt{2}}\sqrt{\ell(1-\ell)}(z+\bar{z})e^{-|z|^2} \\
\langle S_y \rangle &= \frac{N}{\pi\sqrt{2}}\sqrt{\ell(1-\ell)}(-i)(z-\bar{z})e^{-|z|^2} \\
\langle S_z \rangle &= \frac{N}{\pi}(1-\ell)e^{-|z|^2} \ . \qquad (5.4)
\end{aligned}$$

The state at $\ell_a^{-\epsilon} < \ell < 2/3$ corresponds to $(0, \lambda\phi_0(z), \eta\phi_1(z))$, leading to a spin vector that vanishes at the center of the disc.

For $\gamma = -\epsilon$, $2/3 < \ell < \ell_b^{-\epsilon}$, the condensate can be represented by the spin vector $(\sigma\phi_2(z), \xi\phi_0(z), \tau\phi_1(z))$, with ξ, σ and τ as above, while for $\ell_b^{-\epsilon} < \ell \leq 1$ we have $(\sigma\phi_2(z), \tau\phi_1(z), \xi\phi_0(z))$.

In the ferromagnetic regime the ω dependence of the ground state angular momentum becomes a smooth curve, see figure 5.4.

5.1.3 Mean field configuration at $L = N$

Assuming that only the first three $m = 0, 1, 2$ orbitals participate in the ground state, we find that the mean field ground states at the special value $\ell = 1$ take the form $(\mp\sigma\phi_2(z), \tau\phi_1(z), \xi\phi_0(z))$, with $\xi = \sigma = \sqrt{k_\pm}$ and $\tau = \sqrt{1-2k_\pm}$, and with the $(+)-$ sign corresponding to (anti-)ferromagnetic interactions. The parameters $k_\pm$ depend

on γ according to

$$k_{\pm}(\gamma) = \frac{\mp(19+28\sqrt{2})\gamma^2 + (42 \pm 4\sqrt{2})\gamma - 3}{71\gamma^2 + 126\gamma - 9} \ . \tag{5.5}$$

The orbital occupation numbers, given as

$$\langle n_{10} \rangle = 1 - 2k_{\pm}, \quad \langle n_{0\downarrow} \rangle = \langle n_{2\uparrow} \rangle = k_{\pm} \ , \tag{5.6}$$

are continuous for γ going through 0, but the spin-texture, which is sensitive to the phases in the condensate wave function, is not. We find that for $\gamma = \pm\epsilon$, up to an overall constant,

$$\begin{aligned} \langle S_x \rangle &= (1 \mp \frac{1}{\sqrt{2}}\bar{z}z)(z+\bar{z})e^{-|z|^2} \\ \langle S_y \rangle &= (1 \mp \frac{1}{\sqrt{2}}\bar{z}z)(-i)(z-\bar{z})e^{-|z|^2} \\ \langle S_z \rangle &= (1 - \frac{1}{2}(\bar{z}z)^2)e^{-|z|^2} \ . \end{aligned} \tag{5.7}$$

Note that in the anti-ferromagnetic case, the expectation value of the spin vector is vanishing on the circle $\bar{z}z = \sqrt{2}$, while in the ferromagnetic case we see a single skyrmion texture with $\langle \vec{S} \rangle$ non-vanishing everywhere. Figure 5.6 shows the spin texture at $\ell = 1$ for $\gamma = \pm\epsilon$.

From equation (5.5) it is possible to derive the critical anti-ferromagnetic interaction ratio for which the polar vortex appears, by simply solving $k_+(\gamma) = 0$. The critical value found then is $\gamma^* = (7+4\sqrt{2})/17 \approx 0.75$ (see figure 5.3). If γ increases towards γ^*, the density in the $m = 3$ orbital acquires a small value. So, strictly speaking, the states discussed here are not the true mean field ground state in the whole intermediate region. Around $\gamma = 0$ and $\gamma = \gamma^*$ however, $\langle n_{3\alpha} \rangle$ is zero and the value of γ^* is in agreement with numerical results.

In the ferromagnetic regime, upon lowering γ the parameter k_- gradually decreases from $k_- = 1/3$ at $\gamma = 0$ to $k_- = 1 - \frac{1}{\sqrt{2}}$ at $\gamma = -1$, with the corresponding occupation numbers given in equation (5.6).

5.1.4 The sphere with $N_v = 1, 2$

It is instructive to perform LLL mean field theory on a system of spin-1 bosons in a spherical geometry, with $N_v = 1$ or $N_v = 2$, meaning that 2 or 3 orbitals are available to the particles. To compare with the disc as before, we write these results in terms of $\ell = (\frac{1}{2}N_v - \tilde{L})/N$. Notice, however, that by flattening out the sphere by stereographic projection, the results are qualitatively similar to those for the disc when only the first two or three orbitals are occupied. This is especially true for the states at $N_v = 2$, $\ell = 1$. Even though the topological classification of textures does not strictly apply to

the plane, the form of the spin textures on the sphere is a useful guide to those in the disc for $\ell \leq 1$.

For the case $N_v = 1$ (two orbitals on the sphere), we mention the following results. With $0 < \gamma \leq \pi/4$ the ground state configuration is the same as the one we found on the disc for $\ell < \ell_a^{\epsilon}$. This configuration can be interpreted as two π-disclinations at opposite poles of the sphere. For $\pi/4 \leq \gamma < \pi/2$ all bosons occupy the $\alpha = 0$ spin component, forming a polar state with a single vortex. In the ferromagnetic regime, with very small γ we find the same spin transition as the one on the disc at $\ell = \ell_a^{-\epsilon}$. With $N_v = 1$ this transition lies at $\ell = 1/2$. These configurations can be interpreted as a half-skyrmion (or meron) in the spin texture. with the spin density vanishing at one point on the sphere, around which the spin density winds around the equator in $\vec{S}$-space, passing over one pole at the opposite end of the sphere. If the interaction is deformed by increasing N_v towards $N_v \to \infty$, the location of the spin transition is gradually shifted towards $\ell = \ell_a^{-\epsilon}$. With finite ferromagnetic interaction ($N_v = 1$ again), there is a finite region where the core traces a path over the sphere (from the south pole to the north pole, as ℓ increases) and connects the two sides of the transition. The interaction energy is clearly independent of ℓ. This region is bounded by $\gamma(\ell) = -|\arctan(2\ell - 1)|$ for $0 \leq \ell \leq 1$.

For $N_v = 2$ and $\gamma = 0$, the occupation numbers, summed over spin, in the three available orbitals are given by $\langle n_0 \rangle = 1 - \ell$, $\langle n_1 \rangle = \ell$ and $\langle n_2 \rangle = 0$ for $0 \leq \ell \leq \frac{1}{3}$, followed by $\langle n_0 \rangle = \frac{5}{6} - \frac{1}{2}\ell$, $\langle n_1 \rangle = \frac{1}{3}$, $\langle n_2 \rangle = \frac{1}{2}\ell - \frac{1}{6}$ for $\frac{1}{3} \leq \ell \leq 1$. These mean field results agree with the exact quantum ground state results obtained in section 4.3.

For $N_v = 2$ and small ferromagnetic interactions, $\gamma = -\epsilon$, the mean occupation numbers in the condensate are given in table 5.3 (up to $SO(3)_{\rm spin}$ and $SO(3)_{\rm orb}$ rotations). In the trajectory from $\ell = 0$ to $\ell = 1$ there are no spin transitions. The $\ell = 1$ state, which has $\langle n_{0\downarrow} \rangle = \langle n_{10} \rangle = \langle n_{2\uparrow} \rangle = \frac{1}{3}$, is the mean field ground state for arbitrary ferromagnetic spin interactions, $0 > \gamma > -1$. It is a single skyrmion texture with both uniform number density and magnitude of the spin density.

	$\langle n_{0\downarrow} \rangle$	$\langle n_{10} \rangle$	$\langle n_{2\uparrow} \rangle$
$0 \leq \ell \leq \frac{1}{3}$	$1 - \ell$	ℓ	0
$\frac{1}{3} \leq \ell \leq 1$	$\frac{5}{6} - \frac{1}{2}\ell$	$\frac{1}{3}$	$\frac{1}{2}\ell - \frac{1}{6}$

Table 5.3: Mean occupation numbers of the LLL mean field ground state in spherical geometry, $N_v = 2$, with small ferromagnetic interaction $\gamma = -\epsilon$.

In the case $N_v = 2$, and small anti-ferromagnetic interactions, $\gamma = +\epsilon$, for $0 \leq \ell \leq \frac{1}{3}$ the mean occupation numbers per orbital of the condensate are the same as in the ferromagnetic case, but the spin structure is different. For $\ell \geq \frac{1}{3}$ the spin expectation values in the $m = 0$ and 2 orbitals become non-zero (without a discontinuity) and are not linear functions of ℓ. Since $|\langle \vec{S}_{m=1} \rangle|^2 = 0$ and the number density is constant in the $m = 1$ orbital, the spin state describing the bosons in this orbital can be arranged by an $SO(3)$ rotation to be $(0, 1, 0)/\sqrt{3}$. The vectors representing the bosons in the $m = 0$, 2 orbitals then are simply constructed. Together with the

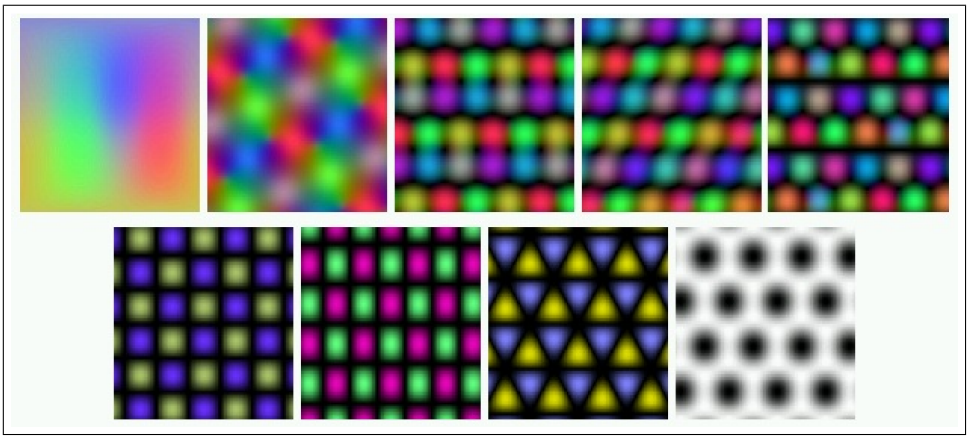

Figure 5.7: The different lattices found in rotating spin-1 boson condensates. The first picture is the mapping of the spin-sphere to the colors used. Top and bottom correspond respectively to the north and south pole. The intensity codes $|\langle\vec{S}\rangle|$, the size of the spin-vector. Other pictures are the spin expectations at different ratios c_2/c_0: $\phi = -0.1$, 0.01, 0.016, 0.04, 0.1, 0.54, 0.7 and 0.9. The last picture shows the density, as the spin vanishes.

previously-mentioned vector they form a mutually orthogonal set which minimizes H_n. Provided that the spin-vectors are properly normalized, the energy can be expressed in terms of one parameter $\alpha(\ell)$, which is connected to the spin densities by $\cos[2\alpha(\ell)] = |\langle\vec{S}_0\rangle|/\langle n_0\rangle = |\langle\vec{S}_2\rangle|/\langle n_2\rangle$. Minimizing the energy with respect to $\alpha(\ell)$ gives

$$\alpha(\ell) = \arccos\left[\sqrt{\frac{1}{2} + \frac{\frac{1}{4}\sqrt{\lambda(\frac{2}{3}-\lambda)}}{1-4\lambda+6\lambda^2}}\right], \tag{5.8}$$

with $\lambda = \frac{1}{2}(\ell - \frac{1}{3})$. The maximum of the anti-ferromagnetic energy is not dependent on the angular momentum and lies at $\alpha = \pi/2$. In the ferromagnetic case this point minimizes the energy, corresponding exactly to the occupation numbers in table 5.3.

At $\ell = 1$, there are solutions with uniform density, with an unbroken $SO(3)$ subgroup of the $SO(3)_{\rm orb} \times SO(3)_{\rm spin}$ symmetry, as the limiting case of the previous $\ell < 1$ states. There are also solutions in which the orbital distribution in the mean field configuration of the ground state is not unique. For instance, among the degenerate states at large γ we find the polar vortex with $\langle n_{10}\rangle = 1$ and a configuration with $\langle n_{20}\rangle = \langle n_{00}\rangle = \frac{1}{2}$.

5.1.5 Comparison with finite size exact states

It is of interest to try to match the mean field states with ground states found in diagonalization studies, such as those shown in Figure 4.4 for the disc. Since these have definite values of the quantum numbers, they can be compared with the mean field states only by projecting the latter to components with definite quantum numbers. For each N and L, the value of the spin picked out should reflect the form of the interaction, and should presumably be the maximal value in the ferromagnetic regime, and the minimal value in the antiferromagnetic. For the spin-independent case $c_2 = 0$, the lowest $SU(3)_{\rm spin}$ quantum numbers are favored as ground states.

We will not attempt to identify all the states in figure 4.4 in this way, but only some of the more prominent. We have already mentioned that the mean field state at $\ell = 1$ and $c_2 = 0$ corresponds to the BTC singlet state. Since the mean field state has equal mean occupation of $(m, \alpha) = (0, \downarrow)$, $(1, 0)$, and $(2, \uparrow)$, it does contain a unique singlet component which is exactly the BTC state. When c_2 is turned on, the quantum numbers remain at $(L, S) = (6, 0)$, but the state will be slightly altered in its details. The corresponding skyrmion spin textures on the sphere are discussed in the appendix of reference [8].

The BDC multiplet at $L = N/2$ for $c_2 = 0$ that uses only $m = 0$, 1 also deserves comment. This corresponds in mean field theory to the $N_v = 1$ case discussed briefly in the appendix of [8]. When $c_2 < 0$, it becomes a single skyrmion, which survives for all $-1 \leq \gamma \leq 0$. This skyrmion has no projection to spin 0, and anyway for this regime maximal spin is expected in the ground state. Indeed, for $N = 6$ the corresponding ($L = 3$) state has $S = 3$. The whole regime $L/N \leq 1$ for ferromagnetic interactions resembles what one expects for skyrmions, that is L (corresponding to $N - \tilde{L}$ on the sphere) decreasing as S increases, as $S = N - L$. For $c_2 > 0$ and $L = N/2$, the lowest-spin part of the BDC state becomes the ground state.

At larger positive γ, there is a prominent region of $(L, S) = (6, 0)$ in the $N = 6$ data. At the largest γ, we expect that this can be identified (in the same sense as the preceding discussion, or as in reference [108]) with the polar vortex state of this section. (In a finite size study, one would not expect to see a transition from the BTC state at $c_2 = 0$ to this polar vortex with the same quantum numbers at large γ.) The jump from $L = 0$ to $L = 6$ expected from the mean field is seen in figure 4.4. At smaller γ, a $(3, 0)$ region is seen. We speculate that this state corresponds to a single π-disclination at the center of the trap (with a second one at infinity, or the opposite pole on the sphere), and that the region corresponds to $\ell_a^\epsilon < \ell < 2/3$ in the mean field results. Notice also the prominent semi-plateaus near $\ell = 0.5$ in the plots in figure 5.4 at larger γ.

5.2 Vortex and skyrmion lattices

Upon driving the system faster, multiple skyrmions are induced. These are expected to form a lattice and can be well treated in a (quantum Hall) mean field analysis.

Such an analysis was performed by Kita *et al.* [61], who found a range of different lattices for $c_2 > 0$, depending on the relative strength to c_0 and the rotation. By including higher Landau levels, they were able to show that some of these lattices are qualitatively identical at high and low rotation. Near $c_2 = 0$, the (scalar) vortex breaks up into three vortices, one for each spin component, forming a triangular lattice. For $c_2 \geq .09c_0$, the vortex splits into two π-disclinations, which make up a square (anti-ferromagnetic) lattice.

We have carried out a program, similar to Mueller and Ho [63], appropriate for a mean field LLL description of a multi-component condensate. The LLL approximation (in the limit $\omega \to \omega_0$) fixes the vortex lattice spacing to be equal to the harmonic oscillator length. Note that this is different from the Thomas-Fermi regime, where the distance is fixed by the number of vortices, as the density of bosons is the same as in a non-rotating trap.

Under the assumption that the vortices in each spin component form a Bravais lattice, we can choose the one-particle wavefunctions to be the torus wavefunctions with N_v flux quanta (typically, $N_v = 1$ or $N_v = 2$). For a scalar condensate, the lattice is completely specified by the geometry τ of the torus. This wavefunction is periodic up to a gauge transformation, equivalent to requiring $A'(\mathbf{r}') = A(\mathbf{r})$.

In the case of multi-component condensates, however, more general boundary conditions are possible. We only need to demand

$$\psi'(\mathbf{r} + \mathbf{L}_i) \quad = \quad e^{i\Lambda_i(\mathbf{r})}\, U_i\, \psi(\mathbf{r}), \tag{5.9}$$

where $\mathbf{L}_i$ ($i = 1, 2$) define the geometry, and Λ_i is the gauge transformation mentioned above. The matrices U_1 and U_2 should commute, $U_1 U_2 U_1^{-1} U_2^{-1} = 1$, to obtain single-valued wavefunctions.

We require that U_1 and U_2 commute with the Hamiltonian, so that the energy of a unit cell is well-defined. For $\gamma \neq 0$, this implies $U_i \in SO(3)_{\rm spin}$. The common eigenvectors of U_1, U_2 then have eigenvalues $(1, e^{i\varphi_1}, e^{-i\varphi_1})$ and $(1, e^{i\varphi_2}, e^{-i\varphi_2})$. With an overall $SO(3)$ rotation, we can fix the direction of the vector with eigenvalue 1 to be parallel to $\hat{z}$ in spin space. With this, the unit cell of the magnetic order (seen in the spin density which is gauge invariant, for example) is larger than that of the density, but always contains an integer number of the latter.

Using this approach, we can confirm a large part of the phase diagram of Kita *et al* [61], but we also find additional phases in the ground states at large γ. These are polar phases, for which we use a unit cell with a single flux quantum. We will use $\gamma = \tan\phi$ as the parameter. The minimization procedure uses a simplex downhill algorithm in the geometry τ and the phases φ_1, φ_2. The wavefunction is obtained from the polynomial free energy by using a conjugate gradient algorithm, starting from a random point. The wavefunction in general is unique up to a phase and a $SO(3)$ rotation along the $\hat{z}$-axis.

The phases we obtain, as illustrated in figure 5.7, are as follows:

ferro lattice. A major part of the ferromagnetic phase diagram ($-\pi/4 \leq \phi \leq -0.08$) is covered by a lattice with $N_v = 2$ flux quanta in the unit cell. This is the

same lattice as one obtains for the spin-$\frac{1}{2}$ bosons with full $SU(2)$ symmetry or, equivalently, the quantum Hall ferromagnet with the Landé factor $g = 0$. If we consider the spin-1 to be composed of two spin-$1/2$ particles, then $N_v = 2$ for the spin-1 bosons corresponds to $N_v = 1$ for the spin-$\frac{1}{2}$ particles. This structure is related to the $N_v = 2$ skyrmions discussed in the Appendix of [8].

square ladder. The triangular vortex lattice of the $c_2 = 0$ case is essentially unchanged up to $\phi = 0.0143$, being squeezed only. However, the $SU(3)$ symmetry is broken. This spin shows a ladder structure, where adjacent ladders are shifted by $3/2$ rung-spacings.

canted ladder, $0.0143 \leq \phi \leq 0.0193$. The ladder structure stays intact, however the rungs are now canted.

triangular ladder, $0.0193 \leq \phi \leq 0.069$.

square π-disclination, at $\phi \approx 0.069$, there is a first order phase transition to the square π-disclination lattice. Only the $\uparrow$ and $\downarrow$ components are present in this lattice.

squeezed π-disclination, $0.428 \leq \phi \leq 0.62$. The lattice is squeezed in one direction and expanded in the other.

triangular π-disclination, $0.62 \leq \phi \leq 0.786$. At $\phi \approx 0.62$, there is a first order phase transition to a triangular π-disclination lattice.

polar Abrikosov, beyond $\phi \approx 0.786$, the π-disclinations are unstable and the systems prefers to have only one component, such that $\langle \vec{S} \rangle = 0$ everywhere. The vortices of this component form an Abrikosov lattice, with vanishing density at the cores.

We were unable to obtain conclusive results in the remaining region, $-0.08 \leq \phi \leq 0$. Possibly it involves the $N_v = 1$ type of skyrmions mentioned in the Appendix of [8]. The phases for $\phi > 0.428$ were not observed before.

To check whether the Ansatz is sufficiently general in the complete phase diagram, we have supplemented the above analysis by direct numerical computations of LLL mean field ground states in a disc geometry, with $\omega < \omega_0$. In these computations, which do not assume any lattice structure, dominant phases such as the square lattice of π-disclinations, are recovered correctly. Clearly, finite size effects are important here and this most probably accounts for the fact that not all the phases listed above have been recovered in these computations.

At special values of φ_1, φ_2, when they are both of the form $p\pi/q$ (p, q integer), it is possible to realize the lattice by using a larger unit cell and identical phases for all three spin components. An example of this is the triangular lattice at $c_2 = 0$, where $\varphi_1 = -\varphi_2 = 2\pi/3$. In this case, we can realize the same lattice by using a torus with 3 flux quanta. The other example is the square π-disclination lattice, which can be described by using 2 flux quanta. This can be compared to the spin-$1/2$ situation [63], where the lattice at $g_{12} = g_1 = g_2$ (unbroken $SU(2)$ symmetry) can equivalently be described by using a torus with 2 flux quanta [61, 115].

Chapter 6

Density profiles for atomic quantum Hall states

We[1] *analyze density profiles for atomic quantum Hall states, which are expected to form in systems of rotating atoms in the high-rotation limit. For a two-dimensional (single-layer) system we predict a density landscape showing plateaus at quantized densities, signaling the formation of incompressible ground states. For a set-up with coupled, parallel layers, we predict (i) at intermediate values of the inter-layer tunneling: a continuously varying density profile $\rho(z)$ across the layers, showing cusps at specific positions, (ii) at small values for the tunneling, quantum Hall-Mott phases, with individual layers at sharply quantized particle number, and plateaus in the density profile $\rho(z)$.*

Among the fascinating developments in the field of quantum gases is the possibility to study correlated states of matter in a setting that is entirely different from the traditional setting of electrons in a solid state environment. As discussed in section 2.2.1, a prime example are fractional quantum Hall states, which are expected when trapped atoms (bosons or fermions) are made to rotate at ultra-high angular momentum [44, 45, 46, 47, 48, 49, 116, 50, 7, 8]. While there has been steady progress in achieving high rotation rates [55, 40], the conditions for the actual realization of these states have not yet been met. [See [100, 101] for alternative proposals aimed at conditions where atomic quantum Hall states are expected].

The most direct experimental signature of electronic (fractional) quantum Hall states, the quantization of the Hall conductance, is not easily available for realizations of such states with neutral atoms. It is thus important to investigate the experimental signatures of atomic quantum Hall states. A number of largely complementary

[1] This chapter is based on a collaboration with N. R. Cooper, F. J. M. van Lankvelt and K. Schoutens, see [117].

proposals have been made

- fractional (braid) statistics [118]
- vanishing of condensate fraction [42]
- detection of gapless edge excitations [119]
- detection of density correlations in expansion image [120, 121]
- characteristic density profiles [122, 123]

In this chapter, we work out the proposals put forward in [122, 123] for the detection of atomic (fractional) quantum Hall states via characteristic density profiles in a suitably engineered experimental set up.

We will present results for density profiles in a single layer, and for a multi-layer configuration. The possibility of reaching the quantum Hall regime in a geometry with a large number of parallel layers (defined by an optical potential) is among the options presently pursued by experimental groups.

Among the predictions that we make are

- for a single layer system, with weak confining potential: a characteristic plateau landscape for the density, with steps at sharply quantized values of the density,
- for a multi-layer system: a characteristic profile for the particle number per layer, i.e. the density as a function of the coordinate transverse to the individual planes. The main feature here are cusps reflecting the onset of an additional stable liquid in the layers,
- for a multi-layer system: the prediction of quantum Hall-Mott phases, where the atom-number in each individual layer is sharply quantized.

If these features can be observed in experiments, they will stand as clear fingerprints of atomic quantum Hall states for rapidly rotating atoms.

6.1 Density profile in single layer

6.1.1 Phase separation in external potential

We first analyze a single layer situation, with rotation at or near the critical frequency[2] $\omega_\perp$. The characteristic length scales $\ell_\perp$ and $\ell_\parallel$ are set by the harmonic confinement $\omega_\perp$ in the $x-y$ (in-plane) direction and $\omega_\parallel$ in the z (out-of-plane) direction, according to

$$\ell_{\perp,\parallel} = \sqrt{\hbar/(m\omega_{\perp,\parallel})}\,. \tag{6.1}$$

[2] troughout this chapter we use $\omega_\perp$ for the critical angular velocity, instead of ω_0 which we used in the previous chapters.

In situations where we consider an optical lattice in the z-direction, $\ell_\parallel$ can be the Gaussian thickness of either the entire cloud, or a single slice, depending on whether there is not, or is, an optical lattice. In this set-up the energy scale for atom-atom interactions is

$$g_{\rm qH} = \frac{g}{(2\pi)^{3/2}\ell_\parallel \ell_\perp^2} \tag{6.2}$$

with $g = \frac{4\pi\hbar^2 a_s}{m}$, where a_s is the s-wave scattering length. Assuming $a_s = 5$ nm, $\hbar\omega_\perp \simeq 5$ nK, $\ell_\parallel = 50$ nm, $g_{\rm qH}$ is in the order of 1 nK.

We mostly focus on one of the following two situations: (i) harmonic confinement, rotation ω slightly below the critical frequency $\omega_\perp$, leaving a residual parabolic potential in the rotating frame of reference $V_2(r) = \frac{1}{2}k_2 r^2$ with $k_2 \propto (\omega_\perp - \omega)$, (ii) critical rotation $\omega = \omega_\perp$, but in the presence of an additional confining potential, which we take to be a quartic, $V_4(r) = \frac{1}{4}k_4 r^4$.

We refer to [43, 45, 44, 46, 47, 48, 49, 50, 7, 8] for extensive studies of the quantum liquids that form as a function of the rotation drive, after the point where the vortex lattice melts has been crossed. Studies in edge-less geometries (sphere or torus) have pointed at the existence of homogeneous quantum Hall liquids (at critical ω). These liquids have a single preferred filling fraction over the entire geometry. Exact diagonalization studies on a disc have revealed exact groundstates (for up to $N = 10$ particles, as a function of $\omega_\perp - \omega$). Due to finite size effects, the density profiles of these states show large fluctuations. Features of these states, their angular momentum in particular, have been understood in a picture invoking non-interacting composite fermions [44].

In this chapter we focus on inhomogeneous quantum Hall liquids, with density modulated by an external potential such as $V_2(r)$ or $V_4(r)$. The idea is the following. From the numerical studies cited earlier, we infer the existence of stable, incompressible quantum liquids at quantized densities ν_i, and we know the energy per particle ϵ_i in these liquids and the gaps for quasi-particle excitations. If we now consider a given number of particles in a slowly varying external potential, we can patch together regions where the particles form specific quantum liquids, such as to minimize the total energy. Clearly, this task is facilitated by the absence of any long-range forces, which guarantees that the energies can be considered locally, with the one global constraint of reproducing the total of number of particles in the trap.

We remark that non-interacting fermions in a rapid rotation regime, and subject to a slowly varying potential, will display density profiles similar to the ones we discuss here [124]. In that case, the result follows from the Landau level structure for non-interacting fermions, while all results discussed in this chapter are due to interaction effects.

For inhomogeneous systems, in which the potential $V(r)$ varies slowly in space compared to $\ell_\perp$, the density distribution, $n(r)$, averaged on scales large compared to $\ell_\perp$, can be obtained by minimizing the functional

$$E = \int d^2r \left[e[\nu(r)] + V(r)n(r) - \mu n(r) \right] , \tag{6.3}$$

where $e[\nu(r)]$ is the interaction energy per unit area, which is a function of the local filling fraction $\nu(r) \equiv n(r)/n_0$ [$n_0 = 1/\pi\ell_\perp^2$], and μ is the chemical potential (which controls the total number of particles).

That the interaction energy is purely local is a significant simplification, arising from the fact that the interactions are short ranged. Minimisation of the functional then poses a purely local problem. At each position, the density $n(r)$ is that which minimizes

$$e[\nu(r)] - \mu_L n(r) \tag{6.4}$$

where the local chemical potential is

$$\mu_L(r) \equiv \mu - V(r) \ . \tag{6.5}$$

For a vortex lattice (at large filling fraction), the energy density is

$$e[\nu] = n_0 b \nu^2 \times g_{\rm qH} \ , \tag{6.6}$$

where $b = 1.1596$ is the Abrikosov parameter for a triangular lattice. In this case, the dependence of density on local chemical potential is simple:

$$n(r) = \frac{n_0 \mu_L(r)}{2b} \ . \tag{6.7}$$

For filling fractions less than about 10 [46, 42], where the groundstates are incompressible quantum Hall fluids, the energy density is a complicated function of ν, containing cusps at the incompressible groundstates. The presence of these cusps gives rise to a step-like dependence of n on μ_L. Taken with equation (6.5), this step-like dependence of n on μ_L becomes a step-like dependence in space for a confined system (for which $V(r)$ is not constant in space).

6.1.2 Example: two liquids

As a simple example, we consider the possibility of two competing incompressible states: $\nu = \frac{1}{2}$ (for which the interaction energy is zero), and $\nu = \frac{2}{3}$ for which the interaction energy per particle is ϵ_2. These two liquids are the $p = 1, 2$ members of a series at $\nu_p = \frac{p}{p+1}$, which can be understood as integer quantum Hall liquids of composite fermions each consisting of a boson with a single flux quantum attached [44]. Since the system is bounded, we must also consider the case of no particles, $\nu = 0$. The energy per unit area take the values $e[\nu = 0] = e[\nu = \frac{1}{2}] = 0$, and $e[\nu = \frac{2}{3}] = \frac{2}{3} n_0 \epsilon_2$, so minimizing equation (6.4) with respect to these three possible values of the density, $n = \nu n_0$, we find:

$$\nu = \begin{cases} 0 \ , & \mu < 0 \\ \frac{1}{2} \ , & 0 < \mu < 4\epsilon_2 \\ \frac{2}{3} \ , & 4\epsilon_2 < \mu. \end{cases} \tag{6.8}$$

Let us take a harmonic confining potential $V(r) = \frac{1}{2}k_2 r^2$, such that $\mu_L(r) = \mu - \frac{1}{2}k_2 r^2$. The $\nu = \frac{1}{2}$ state forms a disc that extends out to $\mu_L = 0$ (beyond this $\mu_L < 0$ so $\nu = 0$), to a radius $r_1 = \sqrt{2\mu/k_2}$. We further see that there is a critical value of chemical potential, $\mu_c = 4\epsilon_2$, at which the $\nu = \frac{2}{3}$ state will first appear in the center of the trap (where μ_L is maximum). Evaluating the total number of atoms in the $\nu = \frac{1}{2}$ disc at μ_c, we find the critical number

$$N_c = \frac{1}{2} n_0 \pi r_1^2 = 2\epsilon_2/\lambda_2 \tag{6.9}$$

with $\lambda_2 = \frac{1}{2}k_2\ell_\perp^2$. Above this critical value, the disc of $\nu = \frac{2}{3}$ has a radius $r_2 = \sqrt{2(\mu - \mu_c)/k_2}$.

Thus, as the number of particles increases, at first they will form a disc of uniform density $\frac{1}{2}\, n_0$ the radius of which increases with increasing μ (N). Once N reaches N_c (or μ reaches μ_c) a second, inner, disc of density $\frac{2}{3}\, n_0$ will form, and start to expand with increasing N (or μ). In terms of N and N_c the two steps for $N > N_c$ are located at

$$\frac{r_2}{\ell_\perp} = \sqrt{\frac{3}{2}(N - N_c)}\ , \quad \frac{r_1}{\ell_\perp} = \sqrt{\frac{3}{2}N + \frac{1}{2}N_c}. \tag{6.10}$$

The energy as a function of N takes the form

$$E(N) = \lambda_2 \left[N^2 - \frac{1}{4}\Theta[N - N_c](N - N_c)^2 \right] \tag{6.11}$$

We note that the second derivative of $E(N)$ is discontinuous at $N = N_c$.

Note that, although we have only considered the possibilities that $\nu = 0, \frac{1}{2}, \frac{2}{3}$ (and we have not allowed for intermediate values), we do not expect intermediate densities to appear in the density distribution. Since $e[\nu] = 0$ for $\nu < \frac{1}{2}$, values of ν between 0 and $\frac{1}{2}$ are only possible precisely at $\mu_L = 0$ and hence have no finite extent in a generic inhomogeneous system. For the range, $\frac{1}{2} < \nu < \frac{2}{3}$, numerical studies indicate that $e[\nu]$ lies above the straight line joining the end-points $e[\nu = \frac{1}{2}] = 0$ and $e[\nu = \frac{2}{3}] = \frac{2}{3}\, n_0 \epsilon_2$. Therefore, these densities are unstable to phase separation into $\nu = \frac{1}{2}$ and $\nu = \frac{2}{3}$.

A slightly different perspective on the formation of two spatially separated liquids is the following. If one imagines adding more and more particles to a $\nu = \frac{1}{2}$ Laughlin droplet in a (radially symmetric) potential, one will eventually reach the point where the energy of an additional particle at the edge of the Laughlin droplet exceeds the 1-particle energy gap Δ_1 over the bulk Laughlin liquid. The corresponding critical value for N is $\tilde{N}_c = \frac{\Delta_1}{2\lambda_2}$. Using numerical results for Δ_1 and ϵ_2 (as given, for example in [47, 48, 49]) $\tilde{N}_c$ is found to be slightly higher than N_c, in agreement with the fact that $\nu = \frac{1}{2}$ system with additional quasi-particles will lower its energy by phase separating into a central $\nu = \frac{2}{3}$ liquid and an outer ring of $\nu = \frac{1}{2}$ liquid.

Repeating the analysis of the co-existing $\nu = \frac{1}{2}$ and $\nu = \frac{2}{3}$ liquids in a quartic

potential $V_4(r) = \frac{1}{4}k_4 r^4$ leads to a critical N of

$$N_c = \sqrt{\frac{\epsilon_2}{\lambda_4}} \, . \tag{6.12}$$

with $\lambda_4 = \frac{1}{4}k_4 \ell_\perp^4$, with inner and outer edges at

$$\begin{aligned} \left(\frac{r_2}{\ell_\perp}\right)^2 &= \frac{3}{4}(\sqrt{9N^2 - 8N_c^2} - N) \, , \\ \left(\frac{r_1}{\ell_\perp}\right)^2 &= \frac{9}{4}N - \frac{1}{4}\sqrt{9N^2 - 8N_c^2} \, . \end{aligned} \tag{6.13}$$

6.1.3 More liquids

Including in the analysis more quantum liquids, at filling $\nu_1 < \nu_2 < ...$ leads to a sequence of critical values $N = N_c^{(k)}$, marking the start of the formation of a central region of a quantum Hall fluid at $\nu = \nu_k$.

To illustrate the step-like profiles for higher filling fractions, we use the interaction energy function $e[\nu]$ calculated by exact diagonalization studies on a torus [46]. In the graphs presented in figure 6.1, a confining potential $V(r) = \frac{1}{2}k_2 r^2$ is assumed. The energy functional used is for system size of $N_V = 6$ single-particle states on a torus with aspect ratio $\frac{a}{b} = \frac{1}{2}\sqrt{3}$ (solid lines) [for which the numerical results extend up to $\nu = \frac{25}{3}$], and for $N_V = 12$ single-particle states on a torus with aspect ratio $\frac{a}{b} = 0.3$ (dashed lines) [up to $\nu = \frac{7}{6}$].

For filling fractions larger than $\nu \sim 6$, the groundstate is a compressible vortex lattice [46]. The steps seen in the density distribution in that regime are an artifact of the minimum change of filling fraction, $\Delta\nu = \frac{1}{6}$, allowed by the numerics on a finite system with $N_V = 6$. In this regime, the density profile will be smooth (we emphasize again that our results apply only on scales large compared to $\ell_\perp$, so do not describe the short-range density modulations associated with the unit cell of a triangular vortex lattice).

For filling fractions less than $\nu \sim 6$, plateaus appear at the densities of incompressible quantum Hall fluids, including the sequence of Moore-Read and Read-Rezayi states at $\nu = \frac{k}{2}$ (black dashed lines) as well as some of the composite fermion sequence $\nu = \frac{p}{p+1}$ with $p = 2, 3, -4$ [black dotted lines]. One interesting detail is the competition between successive members of the composite fermion series at $\nu = \frac{p}{p+1}$, and the Moore-Read liquid [53, 46, 47, 48, 49] at $\nu = 1$. These states have very different correlations, and one does not expect the higher composite fermion states to be stable against the pairing instability that is at the basis of the formation of the Moore-Read state.

Note that, in the calculation with $N_V = 12$, there is no appearance of the incompressible state at $\nu = \frac{5}{6}$. This indicates that, at least within this small system calculation, the $\nu = \frac{5}{6}$ state appears to be unstable to phase separation into the $\nu = \frac{3}{4}$ and $\nu = 1$ states.

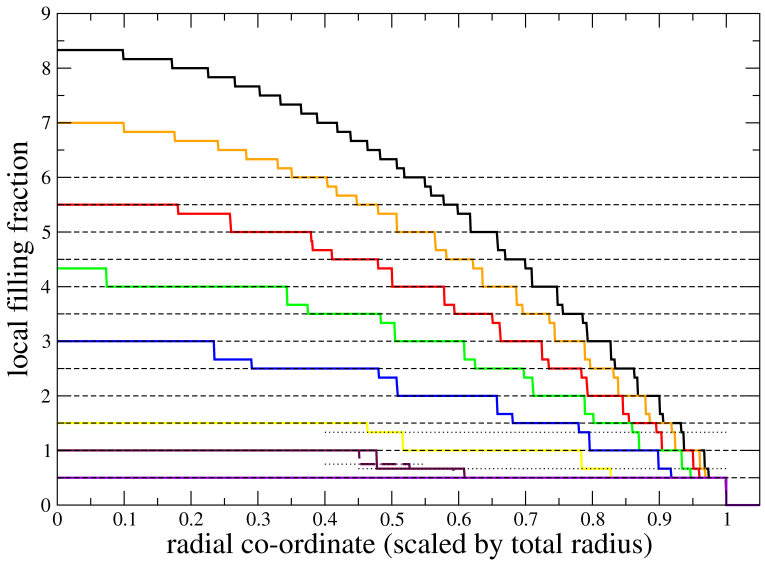

Figure 6.1: Radial density profiles in a single layer with harmonic confinement (at different values for k_2), for a series of filling fractions at the center of the trap. The solid and dashed lines correspond to energy functionals derived for $N_V = 6$ and $N_V = 12$ states in toroidal geometry, respectively.

6.1.4 Small systems

It is tempting to test the above picture against direct diagonalization results for small systems. In earlier studies, the exact groundstates in harmonic confinement (subcritical rotation) were successfully interpreted in terms of the successive filling of Landau levels (LL) for composite fermions [44]. The link with the multi-liquid interpretation is quickly made, if one realizes that a configuration having, say M_1 particles in the lowest composite fermion LL and M_2 in the next composite fermion LL, corresponds to a situation with an inner droplet of $N_2 = 2M_2$ particles forming a $\nu = \frac{2}{3}$ liquid, and an outer ring of $N_1 = M_1 - M_2$ particles in the $\nu = \frac{1}{2}$ Laughlin liquid. The angular momentum for this state is[3] $L = N_1(N_1 - 2) + \frac{3}{4}N_2(N_2 - 2) + \frac{3}{2}N_1N_2$.

However, at the small sizes that can be handled in exact diagonalization (up to $N = 12$ particles on a disc), the density profiles seem to be dominated by edge effects, and the multi-step profiles that we predict for large particle numbers are not easily recognized.

[3]This result is obtained by taking into account that $L = L_{\rm CF} + \frac{1}{2}N(N+1)$, where $L_{\rm CF}$ is the angular momentum of the composite fermions.

6.2 Multi-layer system

6.2.1 Experimental set up

We now investigate the situation where an optical lattice in the z direction is imposed on a cigar shaped cloud of atoms rotating around the z-axis.[4] If the optical potential is sufficiently deep, this will define a stack of parallel planes with (weak) tunneling t between the planes. The idea is that parameters can be chosen such that, while the original cloud is in a mean field regime, displaying a vortex lattice, the individual layers defined by the optical lattice can be in a quantum regime, so that the entire configuration becomes a stack of weakly coupled quantum liquids. We will assume the presence of a chemical potential $\mu(z) = \mu_0 - \mu_2(z/d)^2$ (with d the distance between the layers), which will induce a slow modulation in the number of particles per layer.

One may view a set-up like this as a road towards isolating a single layer in the quantum Hall regime, or perform diagnostics on the entire multi-layer geometry.

The main experimental challenges will be in establishing the multi-layer set-up while preserving the ultra-high rotation rate, and in measuring density profiles for relatively small numbers of particles.

In the following, we shall focus on the consequences of the formation of incompressible states on the density profile as a function of the layer co-ordinate $\rho(z)$. This could be measured from an image of the confined condensate, with a resolution in z better than the optical period.

6.2.2 Melting the vortex lattice

Reaching the regime where quantum Hall states can form, requires a number of conditions. First of all, to forego the formation of a mean-field vortex lattice, the filling factor in each of the layers should be sufficiently low (meaning high-enough total angular momentum per particle) and the interlayer coupling t should be sufficiently small. The second condition is that the tunneling is well below the gap expected for the quantum Hall states.

Concerning the first condition, a quick estimate is made as follows. The critical filling factor ν_c for a single layer has been found to be in the order $\nu_c \sim 6$ to 10. Starting from, for example $N = 5000$ particles and $N_V = 100$ vortices (filling $\nu = 50$), slicing up the condensate into, say, 50 layers of 100 particles each would produce a filling factor per layer of order unity. This would mean that in this set-up a gradual lowering of the the tunneling amplitude would cause a quantum melting of the vortex lattice at a critical $t = t_{c_1}$. For $t < t_{c_1}$ one expects a state with a quantum liquid in each of the layers.

To estimate the critical filling fraction per layer, ν_c', as a function of the tunneling t, we generalize an argument, presented in [42], based on the depletion of the conden-

[4] The authors were first made aware of this proposal by E. Cornell.

sate at ultra-high rotation. For $N = 5000$ particles, $N_V = 100$ vortices and a number of layers $N_L = 50$, our estimate is $t_{c1} \approx 0.1 g_{\rm qH}$ (see reference [125] for a detailed account).

6.2.3 Density profiles for N large

We analyze the multi-layer system for a situation where the number of particles in each individual layer is large, $N_i \gg 1$. Assuming $N/N_L \gg 1$ and $t \ll g_{\rm qH}$ we have the following physical picture. Within each layer, we have a density landscape built out of incompressible qH liquids each of the form shown in figure 6.1 This landscape varies slowly from layer to layer. The gap for bulk excitations over each qH liquid is of order $g_{\rm qH}$ [46, 47, 48, 49] and since $t \ll g_{\rm qH}$ there will be no 'bulk-to-bulk' tunneling events between the layers. However, the energy scale for processes where atoms tunnel from the edge of a quantum Hall fluid in one layer i to the corresponding edge in an adjacent layer $i \pm 1$, is much lower, of order $g_{\rm Mott}$. This scale is defined as $g_{\rm Mott} \simeq \lambda_2$ for quadratic confinement and $g^{(k)}_{\rm Mott} \simeq \lambda_4 (r_k)^2$ for the quartic case, with r_k the (dimensionless) radius of qH liquid k. In terms of $N_0 = g_{\rm qH}/\lambda_2$ ($N_0 = \sqrt{g_{\rm qH}/\lambda_4}$) we have $g^{(k)}_{\rm Mott} \simeq g_{\rm qH}/N_0$ ($g^{(k)}_{\rm Mott} \simeq g_{\rm qH} r_k^2/N_0^2$) for the quadratic (quartic) case. If the tunneling t is large on the scale of $g_{\rm Mott}$, inter-layer tunneling events will establish a continuously varying density profile $\rho(z) = \langle N_i \rangle$ across the layers, where N_i is now the total number of particles in layer i.

We propose two different schemes for experimental detection of the characteristic features of the multi-layer qH configuration. This first is a measurement of the profile $\rho(z)$, from an image of the confined condensate. This can be done provided the period of the lattice, d, is made larger than the imaging resolution (perhaps by forming the optical potential from running waves at a shallow angle[5]). In the second scheme one starts by an expansion of the multi-layered system, and subsequently measures the density profile $\rho_{\rm expanded}(r)$ as a function of the radial coordinate r in the expanded image. We shall see that both profiles $\rho(z)$ and $\rho_{\rm expanded}(r)$ contain characteristic features (cusps). To detect them, one needs a resolution that allows one to reliably determine the local density on the scale of the size of these features: for $\rho(z)$ this is the lengthscale of the density modulations along the optical lattice direction, and for $\rho_{\rm expanded}(z)$ it is the scale of the modulations in the expanded harmonic oscillator basis. [A resolution of a few percent of the total extent of the expanded image may suffice, see figure 6.4.] In both cases, the ability to achieve this spatial resolution is very much enhanced by the fact that in these images of multilayer systems a very large number of atoms are contained within this spatial resolution; the signal strength in an experimental image on this lengthscale can therefore be high.

We now assume quadratic in-plane confinement, and start by considering a situation where the number of particles per layer stays below $N_c^{(2)} = \frac{2\epsilon_2}{\lambda_2}$, so that the quantum Hall liquids in the layers will be Laughlin liquids at $\nu = \frac{1}{2}$. Minimizing the

[5] We learned of this proposal from J. Dalibard.

sum of the potential and interaction energies,

$$-\sum_i(\mu_0-\mu_2 i^2)N_i+\sum_i\lambda_2 N_i^2\ , \tag{6.14}$$

with respect to each of the N_i, we obtain a parabolic Thomas-Fermi density profile

$$\rho(z)=\frac{1}{d^2}\frac{\mu_2}{2\lambda_2}(z_1^2-z^2)\ , \tag{6.15}$$

with $z_1^3=d^3\frac{3N}{2}\frac{\lambda_2}{\mu_2}$. This last equality follows from the constraint $\int\rho(z)\mathrm{d}z\equiv N$.

We next consider values of N, μ_2 that are such that some of the N_i exceed $N_c^{(2)}$. In the corresponding layers, there will be additional stable quantum Hall liquids, as discussed in section 6.1. This leads to a more complicated density profile, $\rho(z)=\sum_k a_k\Theta(z_k^2-z^2)(z_k^2-z^2)$, which exhibits (weak) cusps at the positions $\pm z_k$ where N_i goes through $N_c^{(k)}$. At the position of the cusps, the slope $\frac{\partial}{\partial z}\rho(z)$ changes by a factor of ν_k/ν_{k-1}. As an example, we specify the complete density profile for the case where the central layers near $z=0$, which have the highest density, are in a two-liquid state with densities $\nu=\frac{1}{2}$ and $\nu=\frac{2}{3}$, respectively,

$$\rho(z)=\begin{cases}\frac{1}{d^2}\frac{\mu_2}{2\lambda_2}(z_1^2-z^2) & \text{for}\quad z_2<|z|<z_1\\ \\ N_c^{(2)}+\frac{1}{2d^2}\frac{2\mu_2}{3\lambda_2}(z_2^2-z^2) & \text{for}\quad |z|<z_2\end{cases} \tag{6.16}$$

with $z_1^2-z_2^2=2d^2N_c\frac{\lambda_2}{\mu_2}$ (following from $\mu(z_2)\equiv\mu_c=2\lambda_2N_c$) and $z_1^3+z_2^3/3=d^3\frac{3N}{2}\frac{\lambda_2}{\mu_2}$. This profile shows a (weak) cusp at $|z|=z_2$, with the slope $\frac{\partial}{\partial z}\rho(z)$ changing by a factor of $\frac{4}{3}$.

Choosing an alternative in-plane confining potential changes the nature of the cusps at $z=\pm z_k$. In figure 6.2 we show the cusp at $z=-z_2$ for three choices of the in-plane confinement potential $V(r)$. Clearly, a steeper confinement in the layers leads to a more pronounced cusp in the profile $\rho(z)$.

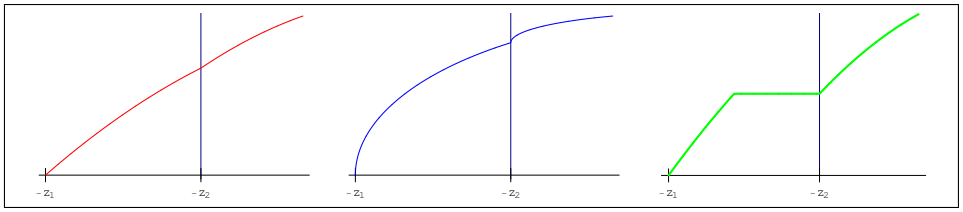

Figure 6.2: Density profiles $\rho(z)$. The layers at $-z_1<z<-z_2$ have the $\nu_1=\frac{1}{2}$ liquid only; the cusps at $z=-z_2$ mark the onset of a second liquid with $\nu_2=\frac{2}{3}$ in the layers. The panels correspond to (left) quadratic confinement, (middle) quartic confinement, (right) quadratic confinement with square well cut-off.

For the case of quartic confinement, the profile at $N < N_c^{(2)}$ is a semi-circle, and the cusps at $|z| = z_k$ have square-root singularities. In fact, $\rho(z)$ is of the general form $\rho(z) = \sum_k b_k \Theta(z_k^2 - z^2)\sqrt{z_k^2 - z^2}$. Figure 6.3 shows the full $\rho(z)$ profile for quartic confinement, with the layers supporting quantum Hall liquids at $\nu_1 = \frac{1}{2}$, $\nu_2 = \frac{2}{3}$, $\nu_3 = 1$.

The density distribution $\rho_{\rm expanded}(r)$, following an expansion the multi-layered system in an otherwise quadratically-confined trap, will have a dependence on the radial co-ordinate r that is of the same qualitative form as $\rho(z)$ is of the axial co-ordinate z.

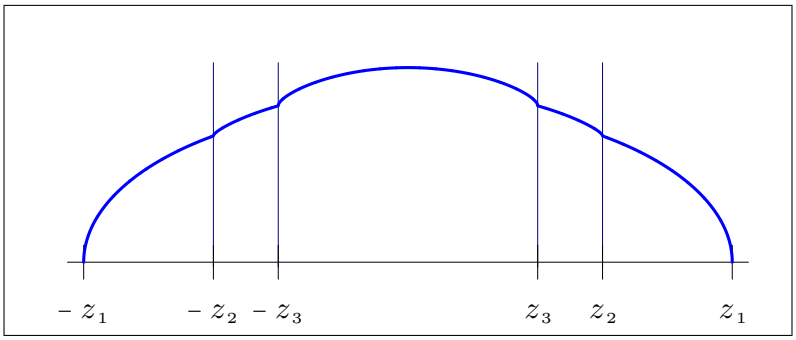

Figure 6.3: Schematic density profile $\rho(z)$, for a situation with quartic in-plane confinement and quantum Hall liquids at $\nu_1 = \frac{1}{2}$, $\nu_2 = \frac{2}{3}$, $\nu_3 = 1$.

We now estimate the magnitude of fluctuations that affect these mean field density profiles. We consider the situation when N is not very much larger than 1. A deviation $\delta N_i^{(k)}$ from the mean field profile for a quantum Hall liquid in layer i costs an energy of order $g_{\rm Mott}^{(k)} (\delta N_i^{(k)})^2$, and one thus expects that tunneling events give fluctuation in the range

$$\delta N_i^{(k)} \simeq \sqrt{N_0 \frac{t}{g_{\rm qH}}} \ , \quad \delta N_i^{(k)} \simeq \frac{N_0}{r_k} \sqrt{\frac{t}{g_{\rm qH}}} \tag{6.17}$$

for the quadratic and quartic cases.[The fluctuations in N_i are the sum of $\delta N_i^{(k)}$ for all liquids present in layer i.] In addition to these, there will be fluctuations where intra-layer edge excitations are excited (for example, by promoting the outermost edge particle at radius r_k to an unoccupied orbital at radius $r_k + \delta r_k$). [Such fluctuations have not been included in the above derivation of the density profile]. Equating the corresponding energy to t leads to

$$\frac{\delta r_k}{r_k} \simeq \frac{N_0}{r_k^2} \frac{t}{g_{\rm qH}} \ , \quad \frac{\delta r_k}{r_k} \simeq \left(\frac{N_0}{r_k^2} \right)^2 \frac{t}{g_{\rm qH}} \tag{6.18}$$

for the quadratic and quartic cases. This shows that if $t \ll g_{\rm qH}$ and N_i/N_0 is not too small, the steps in the in-layer density profiles are well-defined on the scale of the overall radius.

A one shot experiment will obviously produce integer values for all N_i. Based on the above, we predict that these numbers will follow our continuous curves for $\rho(z)$ rather closely, with fluctuations as specified in equation (6.17). Gradually lowering t (for example, by turning on the potential slowly enough) will lead to values N_i that are nearest integer to the corresponding value of $\rho(z)$.

To adress the question whether the density features could still be recognized in the presence of fluctuations, we simulated one-shot density measurements. In figure 6.4 we plotted the results using a system with quartic confinement, supporting quantum Hall liquids at $\nu = \frac{1}{2}$ and $\nu = \frac{2}{3}$. In this virtual experiment we varied the number of layers N_L and the resolution[6], taking the density fluctuations explicitly into account. This was done by randomly taking points from a normal distribution with standard deviation equal to $\delta N_i^{(k)}$ on top of the mean field density. From the points in the figure it is clear that there is a feature near the location where the cusp is expected. This can be concluded both from the change in direction of the 'curve' and from the enhanced scatter in the data points.

6.2.4 Quantum Hall-Mott phases

Our estimate for $\delta N_i^{(k)}$ in equation (6.17) indicates that $\delta N_i^{(k)} \simeq 1$ if t is lowered to a value of order $g_{\rm Mott}^{(k)}$. Based on the analogy with single atoms in an optical lattice, we anticipate a phase where the numbers N_i are sharply quantized, similar to the Mott-Hubbard insulating phase for bosons in an optical lattice.

To investigate this possibility, we write the following Bose-Hubbard hamiltonian

$$\begin{aligned} H[\{N_i\}] &= -t\sum_i H_{\rm tunnel}[i \leftrightarrow i+1] \\ &\quad -\sum_i(\mu_0 - \mu_2 i^2)N_i + \sum_i E(N_i)\ , \end{aligned} \tag{6.19}$$

with $E(N)$ the energy of the optimal N-particle configuration in a single layer.

A Bose-Hubbard hamiltonian is standard in the description of bosonic atoms in optical lattices [13]; in this situation the Bose-Hubbard description is a drastic simplification, as it neglects all excited states within the layers. While the description is thus highly schematic, it does allow us to keep track of the competition between in-plane potential and interaction energy and kinetic energy due to hopping across the layers.

To estimate the critical tunneling rate t for entering a quantum Hall-Mott phase, we shall follow a mean-field treatment. For the standard Bose-Hubbard model, this leads to characteristic 'lobes' in the μ-t plane, marking the boundaries of the Mott states [126]. In these states, the number of particles per lattice site (layer) is sharply quantized, taking on the same values one finds for $t = 0$, i.e. in the absence of any tunneling.

[6] A measurement with a certain resolution of say, R, corresponds to taking one data point per $\frac{1}{R}$ layers.

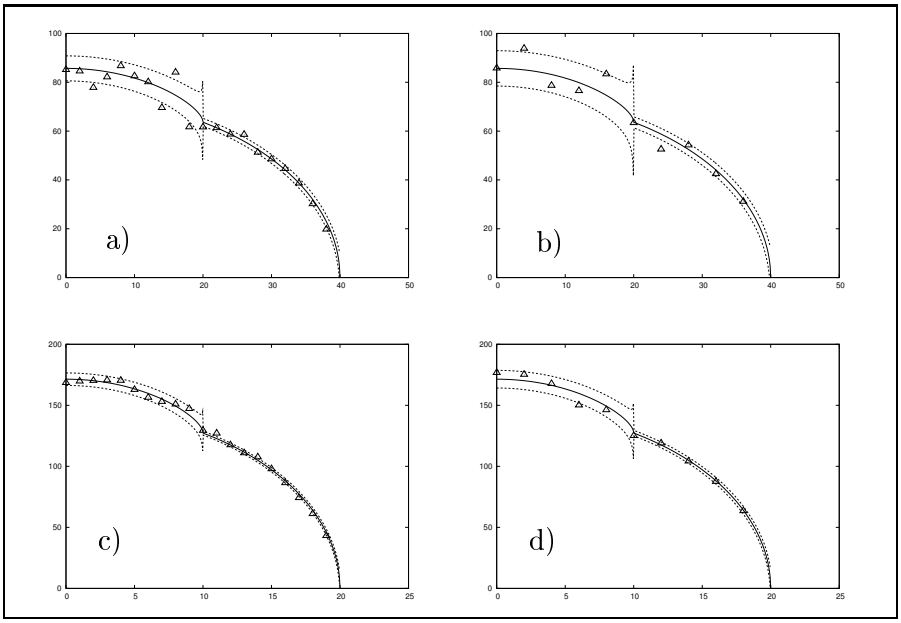

Figure 6.4: A simulated density measurement with $N = 5000$ and $t = .02 g_{\rm qH}$. The two upper figures correspond to a set-up with $N_L = 100$, the lower to $N_L = 50$. On the vertical axis we plotted the particle number per layer and the horizontal axis displays the layer index. We took a different resolution in each 'measurement': a) and d) $\frac{1}{2}$, b) $\frac{1}{4}$ and c) 1. The solid line represents the mean field density profile and the dashed curve the upper and lower range of the fluctuations.

Starting from the hamiltonian equation (6.19), we can again perform a mean field analysis. For simplicity we assume that in each layer the atoms form $\nu = \frac{1}{2}$ Laughlin states. [With this, our analysis extends to small values of N.] Taking into account that the tunneling processes happen at specific locations in the liquid, we do not include any enhancement factors for bosonic statistics. Defining $\Delta_+(N) = E(N+1) - E(N)$, $\Delta_-(N) = E(N) - E(N-1)$, we find the following critical t for the transition into a quantum Hall-Mott state with N particles per layer

$$2t_{c_2}(N) \simeq \frac{(\Delta_+ - \mu)(\Delta_- - \mu)}{\Delta_- - \Delta_+} \ . \tag{6.20}$$

For quadratic in-plane confinement, with $E(N) = \lambda_2 N^2$ and μ satisfying $2\lambda_2(N-1) < \mu < 2\lambda_2 N$, the critical t for entering the N-particle quantum Hall-Mott state is

$$t_{c_2}(N) = -\lambda_2[N - \frac{\mu}{2\lambda_2}][(N-1) - \frac{\mu}{2\lambda_2}] \ , \tag{6.21}$$

with a maximum of $\lambda_2/4$, which is of order $g_{\rm Mott}$, for all N. Scanning the sample

from layer to layer, there will then be segments showing quantum Hall-Mott phases, and 'conducting' regions in between, see figure 6.6. A measurement of the particle number per layer in an N-particle quantum Hall-Mott phase will give $N_i = N$ with no fluctuations. The same measurement in a 'conducting' phase will produce integer numbers as well, but these integers will fluctuate over the range of z where the conducting phase is realized. The presence or not of such fluctuations will tell the difference between the two phases.

One sees that in our approximate description, the case $E(N) \propto N^2$ is critical in the sense that the maximal $t_{c_2}(N)$ is the same for all N. For $E(N)$ 'steeper than' quadratic, the maximal $t_{c_2}(N)$ grows with N.

In figure 6.5 we display a $\mu(z)$-t diagram for quartic in-plane confinement. figure 6.6 shows the corresponding density profile for tunneling $t = t_0$ as in figure 6.5.

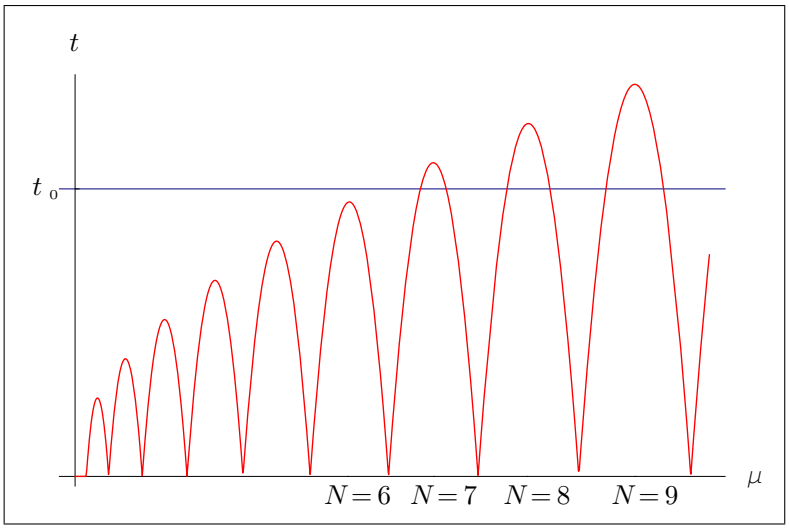

Figure 6.5: Phase diagram in the $\mu(z)$-t plane, with the 'lobes' corresponding to a quantum Hall Mott state with sharply quantized particle number N. The situation shown here corresponds to quartic in-layer confinement, with all layers supporting a $\nu = \frac{1}{2}$ Laughlin quantum Hall state.

To conclude this chapter we summarize the main results. Provided that the quantum Hall regime in a rapidly rotating condensate can be reached in the multi-layer set-up and that suitable density measurements can be performed, unique features can be observed in the density profiles. These features will serve as a characteristic of the atomic quantum Hall states.

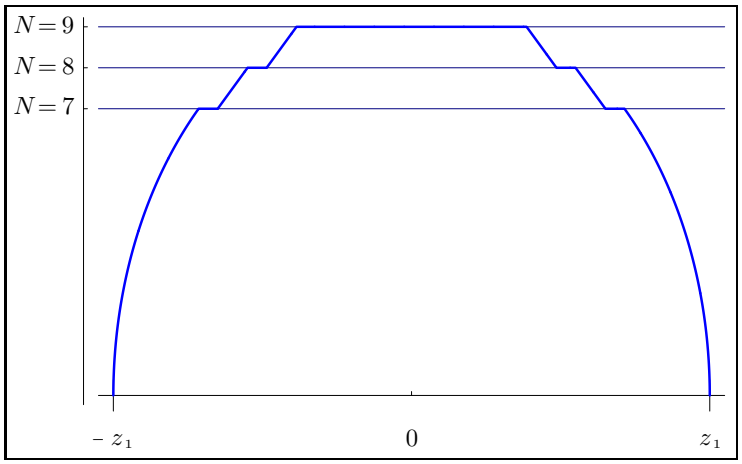

Figure 6.6: Schematic density-profile $\rho(z)$, with parameters corresponding to those in figure 6.5. The horizontal lines indicate the quantum Hall-Mott phases, with sharply quantized particle number per layer, while the remaining parts correspond to 'conducting' phases, with fluctuating values for the N_i.

Bibliography

[1] A. Einstein, *Sitzungsberichte der Preussischen Akademie der Wissenschaften, Physikalisch-mathematische Klasse* (1924) p. 261; (1925) p. 3.

[2] S. N. Bose, *Z. Phys.* **26**, 178 (1924).

[3] H. Kamerlingh Onnes, *Leiden Comm.* **120b, 122b, 124c** (1911).

[4] M. H. Anderson, J. R. Ensher, M. R. Matthews, C. E. Wieman, and E. A. Cornell, Science **269**, 198 (1995).

[5] K.B. Davis, M.-O. Mewes, M. R. Andrews, N. J. van Druten, D. S. Durfee, D. M. Kurn and W. Ketterle, Phys. Rev. Lett. **75**, 3969 (1995).

[6] C. C. Bradley, C. A. Sackett, J. J. Tollett and R. G. Hulet, Phys. Rev. Lett. **75**, 1687 (1995).

[7] J. W. Reijnders, F. J. M. van Lankvelt, K. Schoutens and N. Read, Phys. Rev. Lett. **89**, 120401 (2002).

[8] J. W. Reijnders, F. J. M. van Lankvelt, K. Schoutens and N. Read, Phys. Rev. A **69**, 023612 (2004).

[9] F.J.M. van Lankvelt, *Quantum Hall spin liquids*, PhD thesis, University of Amsterdam (2004).

[10] See, for example, C. J. Pethick and H. Smith, *Bose-Einstein condensation in dilute gases* (Cambridge University Press, 2002).

[11] M. Greiner, O. Mandel, T. Esslinger, T. W. Hänsch and I. Bloch, Nature **415**, 39 (2002).

[12] M.P.A. Fisher, P. B. Weichman, G. Grinstein, and D. S. Fisher, Phys. Rev. B **40**, 546 (1989).

[13] D. Jaksch, C. Bruder, J.I. Cirac, C. W. Gardiner and P. Zoller, Phys. Rev. Lett. **81**, 3108 (1998).

[14] L. P. Pitaevskii, *Zh. Eksp. Teor. Fiz.* **40**, 646 (1961) [*Sov. Phys. -JETP* **13**, 451 (1961)].

[15] E. P. Gross, *Nuovo Cimento* **20**, 454 (1961); *J.Math. Phys.* **4**, 195 (1963).

[16] C. J. Myatt, E. A. Burt, R. W. Ghrist, E. A. Cornell and C. E. Wieman, Phys. Rev. Lett. **78**, 586 (1997).

[17] M. D. Barrett, J. A. Sauer and M. S. Chapman, Phys. Rev. Lett. **87**, 010404 (2001).

[18] D. M. Stamper-Kurn, M. R. Andrews, A. P. Chikkatur, S. Inouye, H. -J. Miesner, J. Stenger and W. Ketterle, Phys. Rev. Lett. **80**, 2027 (1998).

[19] J. Stenger, S. Inouye, D. M. Stamper-Kurn, H. -J. Miesner, A. P. Chikkatur and W. Ketterle, Nature **396**, 345 (1998).

[20] H -J. Miesner, D. M. Stamper-Kurn, J. Stenger, S. Inouye, A. P. Chikkatur and W. Ketterle, Phys. Rev. Lett. **82**, 2228 (1999).

[21] M.-S. Chang, C. D. Hamley, M. D. Barrett, J. A. Sauer, K. M. Fortier, W. Zhang, L. You and M. S. Chapman, Phys. Rev. Lett. **92**, 140403 (2004).

[22] H. Schmaljohann, M. Erhard, J. Kronjäger, M. Kottke, S. van Staa, J. J. Arlt, K. Bongs and K. Sengstock, Phys. Rev. Lett. **92**, 040402 (2004).

[23] T.-L. Ho, Phys. Rev. Lett. **81**, 742 (1998).

[24] H. T. C. Stoof, E. Vliegen and U. Al Khawaja, Phys. Rev. Lett. **87**, 120407 (2001).

[25] F. Zhou, Phys. Rev. Lett. **87**, 80401 (2001).

[26] V.K. Tkachenko, Zh. Eksp. Teor. Fis. **50**, 1573 (1966) [Sov. Phys. — JETP **23**, 1049 (1966)].

[27] I. Coddington, P. Engels, V. Schweikhard, and E. A. Cornell, Phys. Rev. Lett. **91**, 100402 (2003).

[28] M. R. Matthews, B. P. Anderson, P. C. Haljan, D. S. Hall, C. E. Wieman, and E. A. Cornell, Phys. Rev. Lett. **83**, 2498 (1999).

[29] B. P. Anderson, P. C. Haljan, C. E. Wieman, and E. A. Cornell, Phys. Rev. Lett. **85**, 2857 (2000).

[30] P. Rosenbusch, V. Bretin, and J. Dalibard, Phys. Rev. Lett. **89**, 200403 (2002).

[31] K. W. Madison, F. Chevy, W. Wohlleben, and J. Dalibard, Phys. Rev. Lett. **84**, 806 (2000).

[32] J. R. Abo-Shaeer, C. Raman, J. M. Vogels, and W. Ketterle, Science **392**, 476 (2001).

[33] P. C. Haljan, I. Coddington, P. Engels, and E. A. Cornell, Phys. Rev. Lett. **87**, 210403 (2001).

[34] E. Hodby, G. Hechenblaikner, S. A. Hopkins, O. M. Maragò, and C. J. Foot, Phys. Rev. Lett. **88**, 010405 (2002).

[35] I. Coddington, P. C. Haljan, P. Engels, V. Schweikhard, S. Tung, and E. A. Cornell, Phys. Rev. A **70**, 063607 (2004) .

[36] `http://jilawww.colorado.edu/bec`

[37] See A. L. Fetter and A. A. Svidzinsky, J. Phys.: Condens. Matter **13**, R135 (2001), and references therein.

[38] U. R. Fischer and G. Baym, Phys. Rev. Lett. **90**, 140402 (2003).

[39] G. Baym and C. J. Pethick, Phys. Rev. A **69**, 043619 (2004).

[40] V. Schweikhard, I. Coddington, P. Engels, V. P. Mogendorff and E. A. Cornell, Phys. Rev. Lett. **92**, 040404 (2004).

[41] T. -L. Ho, Phys. Rev. Lett. **87**, 060403 (2001).

[42] J. Sinova, C. B. Hanna, and A. H. MacDonald, Phys. Rev. Lett. **89**, 030403 (2002).

[43] N. K. Wilkin, J. M. F. Gunn and R. A. Smith, Phys. Rev. Lett. **80**, 2265 (1998).

[44] N. R. Cooper, N. K. Wilkin, Phys. Rev. B **60** R16279 (1999).

[45] N. K. Wilkin and J. M. F. Gunn, Phys. Rev. Lett. **84**, 6 (2000).

[46] N. R. Cooper, N. K. Wilkin and J. M. F. Gunn, Phys. Rev. Lett. **87**, 120405 (2001).

[47] N. Regnault and Th. Jolicoeur, Phys. Rev. Lett. **91**, 030402 (2003).

[48] N. Regnault and Th. Jolicoeur, Phys. Rev. B **70**, 241307 (2004).

[49] N. Regnault and Th. Jolicoeur, Mod. Phys. Lett. B **18**, 1003 (2004).

[50] T.-L. Ho and E. J. Mueller, Phys. Rev. Lett. **89**, 050401 (2002).

[51] N. Read and E. Rezayi, Phys. Rev. B **59**, 8084 (1999).

[52] R. B. Laughlin, Phys. Rev. Lett. **50**, 1395 (1983).

[53] G. Moore and N. Read, Nucl. Phys. **B 360**, 362 (1991).

[54] J. K. Jain, Phys. Rev. Lett. **63**, 199 (1998).

[55] V. Bretin, S. Stock, Y. Seurin and J. Dalibard, Phys. Rev. Lett. **92**, 050403 (2004).

[56] S. K. Yip, Phys. Rev. Lett. **83**, 4677 (1999).

[57] T. Isoshima and K. Machida, Phys. Rev. A **66**, 23602 (2002).

[58] T. Mizushima, K. Machida and T. Kita, Phys. Rev. Lett. **89**, 30401 (2002).

[59] T. Mizushima, K. Machida and T. Kita, Phys. Rev. A **66**, 53610 (2002).

[60] I. Carusotto and E. J. Mueller, J. Phys. B: At. Mol. Opt. Phys. 37, S115 (2004).

[61] T. Kita, T. Mizushima, K. Machida, Phys. Rev. **A66**, 061601 (2002).

[62] V. Schweikhard, I. Coddington, P. Engels, S. Tung and E. A. Cornell, .Phys. Rev. Lett. **93**, 210403 (2004).

[63] E. J. Mueller and T.-L. Ho, Phys. Rev. Lett. **88**, 180403 (2002).

[64] K. Kasamatsu, M. Tsubota and M. Ueda, Phys. Rev. Lett. **91**, 150406 (2003).

[65] W. I. Glaberson and R. J. Donnelly, Phys. Rev. **141**, 208 (1966).

[66] James C. Weaver, Phys. Rev. A **6**, 378 (1972).

[67] A. T. Fiory, A. F. Hebard, and S. Somekh, Appl. Phys. Lett. **32**, 73 (1978).

[68] M. Baert, V. V. Metlushko, R. Jonckheere, V. V. Moshchalkov, and Y. Bruynseraede, Phys. Rev. Lett. **74**, 3269 (1995).

[69] A. Castellanos, R. Wordenweber, G. Ockenfuss, A. v.d. Hart, and K. Keck, Appl. Phys. Lett. **71**, 962 (1997).

[70] J. I. Marín, M. Vélez, J. Nogués, and Ivan K. Schuller, Phys. Rev. Lett. **79**, 1929 (1997).

[71] David J. Morgan and J. B. Ketterson, Phys. Rev. Lett. **80**, 3614 (1998).

[72] D. R. Nelson and B. I. Halperin, Phys. Rev. B **19**, 2457 (1979).

[73] E. Brézin, D. R. Nelson, and A. Thiaville, Phys. Rev. B **31**, 7124 (1985).

[74] G. Blatter, M. V. Feigel'man, V. B. Geshkenbein, A. I. Larkin, and V. M. Vinokur, Rev. Mod. Phys. **66**, 1125 (1994).

[75] L. Radzihovsky, Phys. Rev. Lett. **74**, 4923 (1995).

[76] C. Reichhardt, C. J. Olson, and Franco Nori, Phys. Rev. Lett. **78**, 2648 (1997).

[77] A. B. Kolton, Daniel Domínguez, and N. Gronbech-Jensen, Phys. Rev. Lett. **83**, 3061 (1999).

[78] C. Dasgupta and O. T. Valls, Phys. Rev. B **66**, 064518 (2002).

[79] V. Zhuravlev and T. Maniv, Phys. Rev. B **68**, 174507 (2003).

[80] W. V. Pogosov, A. L. Rakhmanov, and V. V. Moshchalkov, Phys. Rev. B **67**, 014532 (2003).

[81] J. W. Reijnders and R. A. Duine, Phys. Rev. Lett. **93**, 060401 (2004).

[82] J. W. Reijnders and R. A. Duine, `cond-mat/04011307` (Accepted in Phys. Rev. A).

[83] P. G. Kevrekidis, R. Carretero-González, G. Theocharis, D. J. Frantzeskakis and B. A. Malomed, J. Phys.B: At. Mol. Opt. Phys. **36**, 3467 (2003).

[84] A. B. Bhattacherjee, O. Morsch and E. Arimondo, J. Phys. B: At. Mol. Opt. Phys. **37**, 2355 (2004).

[85] D. Boiron, A. Michaud, J. M. Fournier, L. Simard, M. Sprenger, G. Grynberg, and C. Salomon, Phys. Rev. A **57**, R4106 (1998).

[86] R. Dumke, M. Volk, T. Mther, F. B. J. Buchkremer, G. Birkl, and W. Ertmer, Phys. Rev. Lett. **89**, 097903 (2002).

[87] Z. Chen and K. McCarthy, Opt. Lett. **27**, 2019 (2002).

[88] R. Newell, J. Sebby, and T. G. Walker, Opt. Lett. **28**, 1266 (2003).

[89] H. Pu, L. O. Baksmaty, S. Yi and N. P. Bigelow, `cond-mat/0404750`.

[90] See, for example, H. Kleinert, *Gauge fields in condensed matter* (World Scientific, Singapore, 1989).

[91] L. J. Campbell, M. M. Doria and J. B. Kadtke, Phys. Rev. A **39**, 5436 (1989).

[92] T. -L. Ho and V. B. Shenoy, Phys. Rev. Lett. **77**, 3276 (1996).

[93] B. D. Esry, C. H. Greene, J. P. Burke, Jr. , and John L. Bohn, Phys. Rev. Lett. **78**, 3594 (1997).

[94] E. Timmermans, Phys. Rev. Lett. **81**, 5718 (1998).

[95] L. D. Landau and E. M. Lifschitz, *Theory of Elasticity* (Pergamon Press, New York, 1970).

[96] Lynn Bonsall and A. A. Maradudin, Phys. Rev. B **15**, 1959 (1977).

[97] M. Abolfath, K. Mullen, and H. T. C. Stoof, Phys. Rev. B **63**, 075315 (2001).

[98] See E. B. Sonin, Rev. Mod. Phys. **59**, 87 (1987), and references therein.

[99] D. Jaksch and P. Zoller, New J. Phys. **5**, 56 (2003).

[100] E. J. Mueller, Phys. Rev. A **70**, 041603 (2004).

[101] A. Sørensen, E. Demler and M. Lukin, `cond-mat/0405079`.

[102] U. Al Khawaja and H. T. C. Stoof, Nature **411**, 918 (2001).

[103] D. A. Butts and D. S. Rokhsar, Nature **397**, 327 (1999).

[104] N. Read and D. Green, Phys. Rev. B **61**, 10267 (2000).

[105] F. D. M. Haldane, Phys. Rev. Lett. **51**, 605 (1983).

[106] F. D. M. Haldane, Phys. Rev. Lett. **55**, 2059 (1985).

[107] T. Ohmi and K. Machida, J. Phys. Soc. Jpn. **67**, 1822 (1998).

[108] T.-L. Ho and S. K. Yip, Phys. Rev. Lett. **84**, 4031 (2000).

[109] We thank Ed Rezayi for providing numerical data that prompted our derivation of this result.

[110] G. F. Bertsch and T. Papenbrock, Phys. Rev. Lett. **83**, 5412 (1999).

[111] R. A. Smith and N. K. Wilkin, `cond-mat/0005230`.

[112] P. Nozières and D. Saint James, J. Phys. **43**, 1133 (1982).

[113] E. J. Mueller, Phys. Rev. A **69**, 033606 (2004).

[114] J.-P. Martikainen, A. Collin and K.-A. Suominen, Phys. Rev. **A66**, 53604 (2002).

[115] R. Shankar, private communication.

[116] B. Paredes, P. Zoller and J. I. Cirac, Phys. Rev. A **66**, 033609 (2002).

[117] N. R. Cooper, F. J. M. van Lankvelt, J. W. Reijnders and K. Schoutens, `cond-mat/0409146`, (Submitted to Phys. Rev. A).

[118] B. Paredes, P. Fedichev, J. I. Cirac and P. Zoller, Phys. Rev. Lett. **87**, 010402 (2001).

[119] M. A. Cazalilla, Phys. Rev. A **67**, 063613 (2003).

[120] N. Read and N. R. Cooper, Phys. Rev. A **68**, 035601 (2003).

[121] E. Altman, E. Demler, M. D. Lukin, Phys. Rev. A **70**, 013603 (2004)

[122] F. J. M. van Lankvelt, J. W. Reijnders and K. Schoutens, presentation S3.003 at 2004 APS March meeting (Montreal).

[123] N. R. Cooper, presentation at the conference 'Quantum Gases' KITP Santa Barbara (May 2004).

[124] T.-L. Ho and C. V. Ciobanu, Phys. Rev. Lett. **85** 4648 (2000).

[125] N. R. Cooper, F. J. M. van Lankvelt, J. W. Reijnders and K. Schoutens, manuscript in preparation.

[126] Subir Sachdev, *Quantum phase transitions* (Cambridge University Press, 1999).

[127] B. Wemmenhove, *Statistical mechanics of finitely connected neural networks*, PhD thesis, University of Amsterdam (2004).

Chapter 7

Samenvatting

In dit hoofdstuk wordt een samenvatting gegeven van dit proefschrift. Het is geschreven voor de niet-deskundige lezer. Gedeeltelijk is het gebaseerd op de populair-wetenschappelijke publicatie F. J. M. van Lankvelt, J.W. Reijnders en K. Schoutens, *Nederlands Tijdschrift voor Natuurkunde* **70/2**, (2004) 48-51.

7.1 Roterende bosonen

De spectaculaire recente vorderingen in de kunst van het koelen van atomen hebben het mogelijk gemaakt quantumgedrag van atomen (bosonen en fermionen) bij extreem lage temperatuur direct te bestuderen. Een belangrijke doorbraak was de creatie in 1995 van een Bose-Einstein condensaat, waarin een macroscopisch aantal bosonische alkali-atomen een enkele quantumtoestand bezet. In het verlengde van deze doorbraak werden talrijke aspecten van ultra-koude quantumgassen onder de loupe genomen. De vraag naar het gedrag van een roterend Bose-Einstein condensaat is door experimentele studies ten dele beantwoord: rotatie leidt tot de vorming van vortices (gequantiseerde wervels), die zich in een vlak loodrecht op de rotatierichting rangschikken op een driehoekig rooster. Dit rooster, dat ook in roterende dunne lagen van vloeibaar ^{4}He is waargenomen, is sterk analoog aan het door Abrikosov in 1957 voorgestelde rooster van magnetische vortices in een type-II supergeleider.

De beelden in figuur 2.1 tonen de vorming van een vortexrooster voor een systeem van ^{87}Rb atomen in een (harmonische) magnetische val. Een aantal manieren om een dergelijk systeem aan het draaien te brengen is met succes beproefd: een mogelijkheid is het aanbrengen van een snel-draaiende anisotropie in de opsluitpotentiaal, een andere is het 'roeren met een snel-roterende laserstraal. Het eerste beeld in figuur 2.1 (geen rotatie) toont een Bose-Einstein condensaat. De overige beelden, die corresponderen met steeds toenemende rotatiefrequentie, tonen de vorming van het vortexrooster, waarbij uiteindelijk een toestand is bereikt met ruim meer dan 100 vortices. In deze laatste toestand is de rotatiefrequentie van de val, Ω, nog maar een

fractie kleiner dan de frequentie ω van de harmonische potentiaal van de val. (Bij rotatiefrequenties $\Omega > \omega$ zullen de atomen uit de val ontsnappen.)

De details van de vorming van een driehoekig vortexrooster, en van de verdere eigenschappen hiervan (zoals de frequenties van oscillaties die het rooster vervormen) zijn vanuit de theorie goed begrepen.

De wonderlijke fysica van de roterende Bose-Einstein condensaten wordt helemaal spectaculair als we de systemen voorzien van 'extra ingrediënten' die het quantummechanische karakter onderstrepen. Dit proefschrift gaat over deze roterende condensaten verrijkt met extra ingrediënten. We kunnen de inhoud ervan in drieën verdelen.

I Het gedrag van een vortexrooster in een periodieke potentiaal. De vorm van het vortexrooster, dat normaal gesproken driehoekig is, kan met zo'n potentiaal worden veranderd. Hoofdstuk 3 beschrijft de studie van de verandering van de roosterstructuur als de sterkte of de periode van de potentiaal veranderd wordt.

II Door een optische (niet magnetische) val te gebruiken, kunnen atomen worden gecondenseerd met meerdere 'interne niveaus'. In een spin-vol condensaat, zoals deze systemen genoemd worden, wordt in elk intern niveau een vortex (rooster) gevormd als het systeem aan het draaien wordt gebracht. Hoofstukken 4 en 5 presenteren een studie naar de vorm van deze vortices en roosters daarvan in een condensaat met drie interne niveaus (een spin-1 condensaat).

III Als de rotatie opgevoerd wordt tot zeer grote waarden, verwachten natuurkundigen in plaats van de vortexroosters zogenaamde quantumvloeistoffen aan te treffen. Dit zijn zeer speciale materietoestanden met exotische eigenschappen. In hoofdstuk 6 worden meetbare karakteristieken besproken van deze quantumvloeistoffen in een multi-laag systeem.

7.2 Vortices in optische roosters

Vortices worden ook aangetroffen in type-II supergeleidende systemen. Als een supergeleider in een (niet al te sterk) magneetveld gehouden wordt, worden de magnetische veldlijnen gebundeld. Elke bundel draagt een precieze hoeveelheid magnetische flux. Deze magnetische vortices worden gerangschikt op een driehoekig rooster.

Een bekend verschijnsel in type-II supergeleiders is dat de magnetische vortices 'gevangen' kunnen worden door onzuiverheden in het materiaal. Zo'n onzuiverheid creëert een minimum in de potentiële energie van een vortex. Hierdoor worden vortices letterlijk vastgeprikt (gepind) op een vaste locatie. Dit 'pinning-effect' verrijkt het fasediagram aanzienlijk: naast het driehoekige vortexrooster zijn ook roosters met andere roosterstructuur mogelijk.

De onzuiverheden (pinningcentra) waarop de vortices vastgehouden worden zijn willekeurig verdeeld in het materiaal. Daarom is het onmogelijk om de 'pinning-

potentiaal' precies te weten te komen. Precieze berekeningen van het fasediagram zijn daarom niet mogelijk.

In hoofdstuk 3 bestuderen we een verschijnsel dat analoog is aan het pinnen van vortices in supergeleiders. We bekijken een vortexrooster in een periodieke optische potentiaal. De vorm van deze potentiaal is precies bekend en experimenteel kan deze gemaakt worden met behulp van staande lichtgolven. De maxima van een optisch rooster gedragen zich als pinningcentra in aanwezigheid van vortices. Het effect van vortex-pinning op de (vortex)roosterstructuur in een Bose-Einstein condensaat kan precies berekend worden. Dit is een voordeel ten opzichte van de studie naar vortex-pinning in supergeleidende materialen. Naast de mogelijkheid van theoretische voorspellingen is er nog een groot voordeel: in een experiment kan de sterkte en vorm van de pinning potentiaal expliciet gemanipuleerd worden!

Met de kennis over de vortices en de vorm van het optische rooster kunnen we het fasediagram berekenen. We bespreken hier een voorbeeld: voor een twee dimensionaal optisch rooster en een vortex per pinningcentrum vinden we drie fases, zie figuur 3.2.

i) Voor een sterke optische potentiaal zijn alle vortices gepind op een roostermaximum; de structuur van dit rooster is vierkant.

ii) Voor een zwak optisch rooster vinden we het 'gewone' vortexrooster terug, met hexagonale struktuur.

iii) Tussen bovengenoemde fases in vinden we een vortexrooster waarin de helft van de vortices gepind is. De structuur is dan driehoekig.

Voor verschillende vortexdichtheden vinden we dezelfde fases, alleen de roosterstructuur is dan in het algemeen anders dan in het bovengenoemde voorbeeld.

7.3 Spin-volle condensaten en rotatie

Veel van de relevante alkali-atomen komen voor in hogere spintoestanden (met hyperfijn spin $F = 1, F = 2$,..). Het is interessant om na te gaan wat de effecten van rotatie op bosonen met spin zullen zijn. Een spin-F atoom heeft $2F + 1$ spintoestanden, en door te werken met een optische (niet-magnetische) val kan voorkomen worden dat tussen die toestanden door het Zeeman-effect een energieverschil ontstaat. De spin vrijheidsgraad leidt tot extra parameters in de 2-deeltjes interacties, die bepalend zijn voor de fysische eigenschappen. Voor $F = 1$ atomen is met name van belang of het spin-afhankelijke deel van de interactie anti-ferromagnetisch is (zoals voor ^{23}Na) of ferromagnetisch is (zoals voor ^{87}Rb). Roterende optische vallen zijn experimenteel nog niet gerealiseerd; we rapporteren hier kort de bevindingen van de theoretische analyse in hoofstuk 4 en 5.

Al bij lage rotatie zijn er belangrijke verschillen tussen bosonen met en zonder spin. Voor bosonen zonder spin ontstaan singuliere vortices (de zwarte puntjes in figuur

2.1.), waar de deeltjesdichtheid verdwijnt. Voor bosonen met spin verwachten we spin-structuren, waarin de deeltjesdichtheid nagenoeg constant is, maar de verwachtingswaarde van de spin-vector op ingewikkelde maar continue wijze varieert in de ruimte. Als de rotatiefrequentie verder wordt opgevoerd, ontstaan voor spin-1 atomen roosters (kristallen) van de elementaire spin-structuren. In figuur 5.7 wordt een aantal mogelijke patronen getoond, voor verschillende waarden van de verhouding van de spin-afhankelijke en spin-onafhankelijke interacties van de bosonen.

In een recent experiment werd het effect van rotatie bestudeerd op een Bose-Einstein condensaat met twee interne niveaus. In beide niveaus werd een vortexrooster aangetroffen met een vierkante structuur. Dit veelbelovende resultaat schept goede hoop dat ook experimenten in roterende spin-1 condensaten in de nabije toekomst kunnen worden gedaan.

7.4 Quantumvloeistoffen

We kunnen ons voorstellen aan de serie in figuur 2.1 nog een aantal beelden toe te voegen door de rotatie verder op te voeren en daarmee het verschil $\Omega - \omega$ verder te verkleinen. We komen dan uiteindelijk terecht in een situatie waarin we niet langer mogen verwachten dat de bosonen een vortexrooster zullen vormen. De reden hiervoor is dat naarmate de rotatie toeneemt de deeltjesdichtheid afneemt. De quantumfluctuaties in de posities van de vortices nemen daardoor toe. Bij zeer hoge rotatiesnelheid wordt er een punt bereikt waarop de fluctuaties van de orde van grootte worden van de afstand tussen twee vortices, en waarop het rooster zal 'smelten. Bij deze quantumfaseovergang verdwijnt het Bose-Einstein condensaat definitief uit beeld en ontstaat nieuwe quantumtoestand van snelroterende atomaire materie.

De toestanden die kunnen ontstaan na het quantumsmelten van het vortexrooster zijn vooralsnog buiten het bereik van experimenten, maar zijn theoretisch tamelijk uitvoerig onderzocht. Van groot belang hierbij is de analogie met de fysica van electronen onder de omstandigheden waarbij zogenaamde fractionele quantum Halltoestanden kunnen ontstaan. Het blijkt dat er een preciese analogie bestaat tussen ultrakoude, snel-roterende atomen en electronen in een vlak met een sterk transversaal magnetisch veld.

Het bereiken van het quantum Hallregime vereist extreem hoge rotatiefrequenties en extreem lage (sub-nK) temperaturen, en is daarmee een experimentele uitdaging van formaat. Vooralsnog lijkt de speelruimte voor experimenten in deze richting niet uitgeput te zijn, en er is goede hoop dat het ontstaan van quantum Halltoestanden in ultra koude gassen getoetst zal kunnen worden aan de experimentele realiteit.

Een multi-laag systeem (een roterend ultra koud gas in een 1-dimensionaal optisch rooster) is de meest hoopgevende kandidaat opstelling waarin het quantum Hallregime experimenteel bereikt zou kunnen worden. In hoofdstuk 6 beschrijven we de implicaties van het onstaan van quantum Hallvloeistoffen voor het dichtheidsprofiel van de gaswolk in zo'n multi-laag systeem. We vinden dat er scherpe 'knikken' in de deeltjes dichtheid (gemeten langs de lagen) onstaan als in het systeem een quantum

Hallvloeistof gevormd wordt, zie figuur 6.2. Deze knikken zijn afwezig als een Bose-Einstein condensaat de grondtoestand vormt. Observatie van de knikken in een experiment zal daarom beslissend zijn voor het vraagstuk of de quantum Hallvloeistoffen ontstaan bij hoge rotatie– of niet.

Chapter 8

Dankwoord

Graag wil ik hier een aantal personen bedanken die op het wetenschappelijk vlak bijgedragen hebben aan de totstandkoming van dit proefschrift.

Allereerst mijn promotor, Kareljan, ik zou je mijn 'wetenschappelijke vader' willen noemen. Je geduld en aandacht zijn cruciaal geweest voor dit resultaat. Je had bijna altijd tijd voor me en gaf me maximaal de ruimte om mijzelf te kunnen ontwikkelen. Ik ben je intens dankbaar.

Dan wil ik alle collegae van het ITFA bedanken voor de goede werksfeer. In het bijzonder Frank, Eddy, Rob, Jean-Sébastien, Raoul, Wouter, Bastian, Ruben, Jelper, Anders, Srdjan, Yocklang: de gezellige momenten zal ik niet vergeten. Aan Bastian, die naast collega ook een persoonlijke vriend van mij is, ben ik de nodige dank verschuldigd. Onze 'lunchwandelingen' waren belangrijk voor me. Ook jij mag je achterstallige wetenschapsbelasting [127] die je mij nog verschuldigd bent investeren in je toekomstige aanslagen.

Na het vertrek van Bastian heb ik de traditie van de lunchwandelingen voortgezet met mijn kamergenoot Rob. Ik heb erg genoten van de 'ontspannende' en hilarische gesprekken!

Ook is Rembert, my collaborator in Texas, erg belangrijk geweest voor een gedeelte van dit proefschrift. Waar een wild idee aan de Costa Brava niet toe kan lijden! Een persoon als jij zou je (en met je bedoel ik nu ik) daarvoor dankbaar moeten zijn. Eigenlijk is de 'wetenschappelijke lol' die we hadden nog helemaal niks vergeleken met onze persoonlijke lol.

Verder wil ik ook mijn collega-AIO's en OIO's in het algemeen bedanken voor de goede momenten op diverse wetenschappelijke bijeenkomsten en AIO-scholen. In het bijzonder mijn Utrechtse collegae Dennis en Dries. Dankzij jullie werden deze gebeurtenissen naast leerzaam ook nog gezellig!